DESIGN, FABRICATION AND PRELIMINARY TESTING OF EXPERIMENTAL ROCK DRILLING RIG

A Thesis

by

DUSTIN JOHN TINGEY

Submitted to the Office of Graduate and Professional Studies of
Texas A&M University
in partial fulfillment of the requirements for the degree of

MASTER OF SCIENCE

Chair of Committee,	Alan Palazzolo
Co-Chair of Committee,	Mansour Karkoub
Committee Member,	Robert Lytton
Head of Department,	Daniel McAdams

August 2015

Major Subject: Mechanical Engineering

ABSTRACT

Due to the foreseen need in literature to develop a more complete bit to formation interface law to be used in petroleum drilling applications, a full-scale bit force measurement drilling test rig was developed to measure the various forces acting on the drill bit. The rig features a rock formation sample container that is fixed with sensors to measure the weight on bit, torque on bit, lateral loads on the bit, the rate of penetration and the position of the bit. This sample container is drilled into using a short drill shaft and data is collected during the experiment. The data collected from the test rig can be used to develop a database containing bit factors and drilling factors that can be used to develop a more complete bit to rock interface law.

In order to make a functional drilling rig, much work was put into redesigning and modifying the existing rig to improve performance, reduce cost and to meet updated requirements. The entire rig was analyzed for strength, stability and cost. This included an analysis of manufacturability for all complex parts. This also included the testing and calibrating of all sensors to ensure that all data collected was accurate and useful. A small portion of the work went into the design of a second test rig to measure the drillstring vibrations downhole in an existing well to validate the force law developed with the bit force measurement rig. However, this rig was not manufactured.

The bit force measurement rig was manufactured and completed in May 2015. Once the rig was built and completed, preliminary testing was done to ensure the functionality of the mechanical aspects of the rig and data acquisition system. The data collected from these runs proved that the rig functions as designed and proposed and that additional testing should be undertaken to develop the bit to formation interface law.

DEDICATION

Dedicated to my wife, Stephanie, for her support and encouragement throughout the course of this project

ACKNOWLEDGEMENTS

I would like to thank Dr. Alan Palazzolo for his dedicated work in encouraging and directing me in this work. His expertise and understanding was a key factor for the success and completion of this project.

I would also like to extend gratitude to Dr. Mansour Karkoub at Texas A&M University at Qatar for his patience and his willingness to serve as co-chair of my advisory committee. I would also like to thank Dr. Robert Lytton for putting the time into serving as a member of my advisory committee.

I would like to extend thanks to Randall Tucker of OTBOG Energy for his invaluable advice and insight into the construction and design of both test rigs. I would also like to thank all of the much needed help and support from all of the members of the Vibration Control and Electromechanics Lab (VCEL). Among these, a special thanks for John Shaw, another Graduate Student at VCEL, for his hard work, time and effort during the final months of the project. A special thanks also goes to Erwin “Tom” Thomas for his expertise and time spent on helping with the completion of the rig and in supplying power to the test rig and making it functional.

NOMENCLATURE

API	American Petroleum Institute
BFIL	Bit/Force Interface Law
BHA	Bottom Hole Assembly
CAD	Computer Aided Design
CVEN	Civil Engineering Department
DAQ	Data Acquisition
FEA	Finite Element Analysis
FS	Full Scale
HP	Horse Power
l	Wear-Flat Length
NPT	Non-Productive Time
P	Power
QNRF	Qatar National Research Fund
R_b	Bit Radius
ROP, r	Rate of Penetration
RPM	Rotations per Minute
TAMU	Texas A&M University
TOB, T	Torque on Bit
VCEL	Vibration Control and Electromechanics Laboratory
WOB, W	Weight on Bit
X_R	Lateral Load Rod Local X Axis
Y_R	Lateral Load Rod Local Y Axis
Z_R	Lateral Load Rod Local Z Axis
δ	Depth of Cut per Revolution
ε	Intrinsic Specific Energy

γ	Bit Constant
ζ	Drilling Strength to Rock Strength Ratio
Ω	Shaft Rotation Speed

TABLE OF CONTENTS

Page

LIST OF FIGURES

Page

LIST OF TABLES

Page

1. INTRODUCTION

1.1. Background and Literature Review

The petroleum industry is one of the largest in the world. It was estimated in 2013 that the world uses approximately 90.52 million barrels of oil per day [1]. Oil and gas are used in many applications ranging from fuels to lubricants to ointments. To increase the efficiency and production of oil, researchers are constantly trying to develop ways to increase drilling speed and reduce non-productive time (NPT), which is time spent fixing problems such as stuck pipe, reaming, fishing operations or unscheduled casing [2]. There are many factors involved that reduce the efficiency of drilling. One of the largest limiting factors in drilling performance is vibrations [3]. Controlling and suppressing the vibration of the drillstring not only improves drilling speed, but it also reduces harmful effects such wellbore patterns and bit wear. There are three main classes of vibration that are of concern when referring to drilling and the bottom hole assembly (BHA). The first type is lateral vibration, commonly called whirl. The second is torsional vibration, where the most severe cases are referred to as stick/slip. The last type is axial vibration, commonly referred to as bit bounce. While all of these vibrations reduce the efficiency of the drilling process, stick-slip and lateral vibrations have been identified as the largest bit limiters and a vast majority of the literature focuses on these two types. One study presented evidence that the reduction of lateral vibrations provides benefits to drilling performance such as better borehole quality, reduction in NPT, greater tool reliability and overall lower drilling costs [4]. In order to make the necessary modifications to the BHA and drillstring, the drillstring dynamics must first be understood and modelled. While there has been a large amount of drillstring dynamic study, both analytical and experimental [5], [6], there has not been as much verification and characterization of a full model of the forces acting on the BHA.

To develop a good model of what kind of vibration and how severe it may be, one would need to have a knowledge of the forces acting on the bit. This area of interest, commonly referred to as the bit to formation interface law (BFIL) or bit to rock interface law, is an important topic to understand to fully implement a more accurate model to design more effective vibration control methods. There has been a lot of effort and hard work put into the development of the interface between the drilling bit and the rock formation during drilling operations. Research into this topic has ranged from analytical to experimental and in most cases focuses on only one or two types of vibration. Some of the research only focuses on one type of vibration and the component of the BFIL that is assumed to induce that vibration. For example, Tucker and Wang analyze two torsional vibration models to determine vibration control techniques [7]. In their paper, they use an analytical nonlinear bit torque profile dependent on the rpm of the bit as shown in Figure 1.1. This model was developed using a coulomb friction model using a continuous approximation to produce an alternative to the piecewise model that is generally required to model the stick-slip phenomenon [8]. In this figure, it was pointed out that the region around 0 rpm is the "stick" portion of stick-slip vibrations. This may be a good model and prediction of the torsional forces acting on the bit that induce stick-slip, however, it can't be used as a full model of the BFIL and is not validated by direct experimental research to characterize the model to other applications.

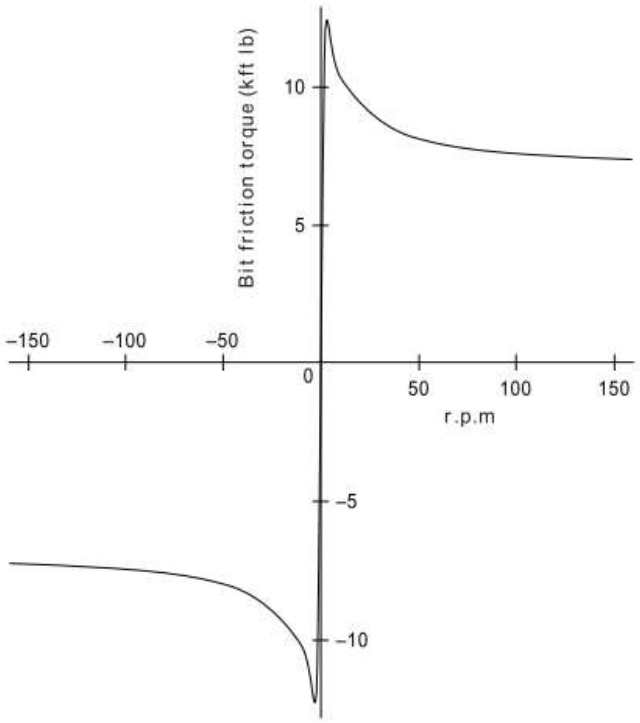

Figure 1.1: Frictional torque curve to simulate the nonlinear effects of the bit torque as related to rotating speed [7], [8]

A more complex and complete model of the torsional forces acting on the bit was later developed that includes axial and torsional coupling [9]–[13] . This model was developed only for drag bits which remove material by shearing the rock. One key attribute to this model is that it includes both a cutting and a frictional component for both the weight on bit (WOB) and torque on bit (TOB) components. The decomposition of these forces can be visualized for a single cutter on a bit in Figure 1.2.

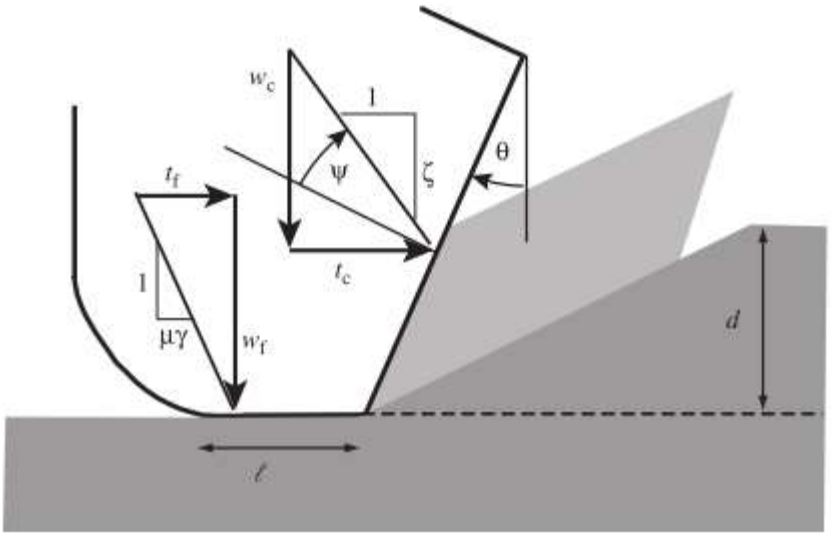

Figure 1.2: Decomposition of total forces into forces transmitted by the cutting face and frictional surface [12]

This model and the literature published to develop and incorporate it discuss that the forces acting on the bit are highly complex and coupled. This relationship, originally derived by Detournay and Defourny, for the bit to force interface law for drag bits is defined as

$$\frac{2T}{a} = (1 - \mu\gamma\zeta)\varepsilon\delta a + \mu\gamma W \tag{1.1}$$

where μ is the coefficient of friction between the bit and formation, γ is a bit constant, ε is the intrinsic specific energy and δ is the depth of cut per revolution. This model was later further developed to include the dynamics of the drillstring vibration [10]. The model was expanded upon by adding the axial stiffness to account for a changing rate of penetration during a constant surface rate of penetration as shown in Figure 1.3. As illustrated in the figure, the formation profile between blades is not modeled as a straight line, which would indicate a constant ROP. Instead the ROP is constantly changing due

to the drillstring dynamics. This is due to the incorporation of a rate-independent interaction law which has been confirmed by experimental results.

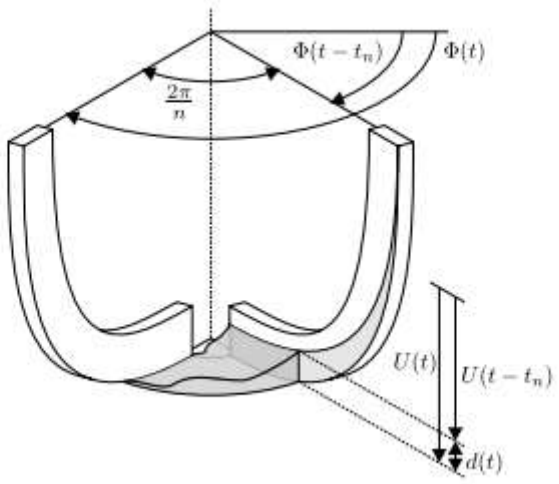

Figure 1.3: Bottom hole profile between two successive blades [9], [13]

It was concluded in the literature that the average cutting forces create a velocity-weakening effect while the average frictional forces create a velocity-strengthening effect [13]. This seemed to be true for both the torsional and axial vibrations. However the overall effect of the bit forces creates a velocity weakening effect which explains the self-excitation of torsional vibrations that could lead to stick-slip. This self-excitation phenomenon of drillstring vibration had often been observed and caused many drillstring failures and bit damage [14]. It has been stated and proven by multiple sources that these self-excited oscillations are unstable. It should also be noted that due to the high complexity of the axial damping, it is very difficult to model and may require experimental characterization. It should be noted that although the model is considered an accurate analytical model, the derived equations are dependent on many constants and factors that must be found experimentally.

While this bit formation interface model for drag bits is widely used and uncontested, it is important to remember that this model was originally only intended for use with PDC drag bits. While there are some similar dynamics to roller-cone bits, there are some differences which prevent from translating this model directly over to use on roller bits. This problem has also been addressed. One of the major differences noted in the dynamics of roller cone bits and drag bits is that roller cones tend to produce a forced axial vibration response that it 3x the running speed [15]. This frequency, often referred to as the tooth frequency [14] is generally not seen in drag bits. On the other hand, the self-excited stick slip response discussed previously is generally not found in roller cone bit applications. Although it is sometimes argued that the cutting dynamics of roller cone bits are different than that of drag bits, most of the mechanics are the same. Both bits use the same idea of the tooth penetrating into the formation and removing material with some dragging motion. This was verified when Franca developed a roller cone model using the same drag bit model developed by Detournay and Defourny. An experimental rig was designed and tested to validate this modified model [16]. As shown in Figure 1.4, the model is very similar to that shown for the drag bit decomposition. It includes a cutting and friction component of the force. The only real difference is the geometry of the cutter itself and that a third component of the weight on bit force is included which is the indentation force.

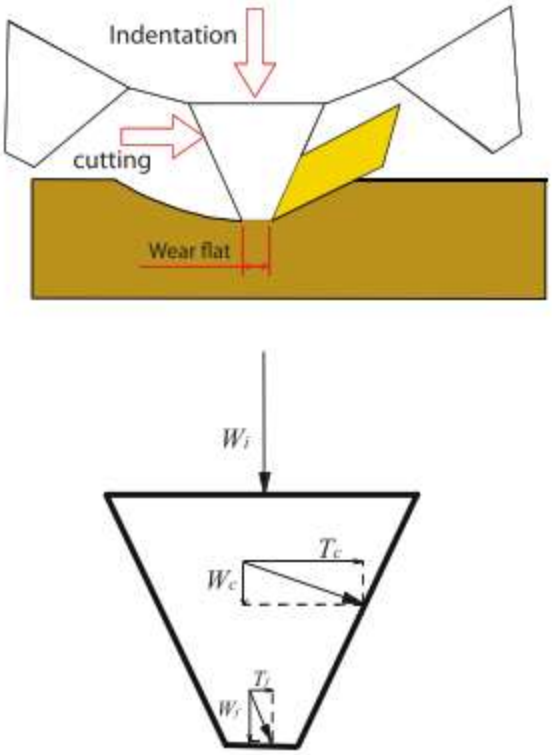

Figure 1.4: Decomposition of forces acting on a single tooth or a roller cone bit [16]

Some other roller cone models have focused on blunt tool indentation force which causes tensile fractures [17], [18]. One of the base models for this approach is the cavity expansion model. This idea takes into account the volume of material displaced and the elastic deformation in the surrounding material as shown in Figure 1.5. This method is based on some assumptions that may make it less accurate than the cutting model adapted from drag bits. However, efforts have been made to incorporate this model into a relatively new drilling approach known as rotary-percussive drilling [19]. This method of drilling is similar to hammer drilling, where there is a spinning component and an axial impact component. This method has been shown to be useful in very hard rock formations. A model was developed by Franca that includes the cutting model modified for roller cone bits plus a component of impact energy which fragments the rock.

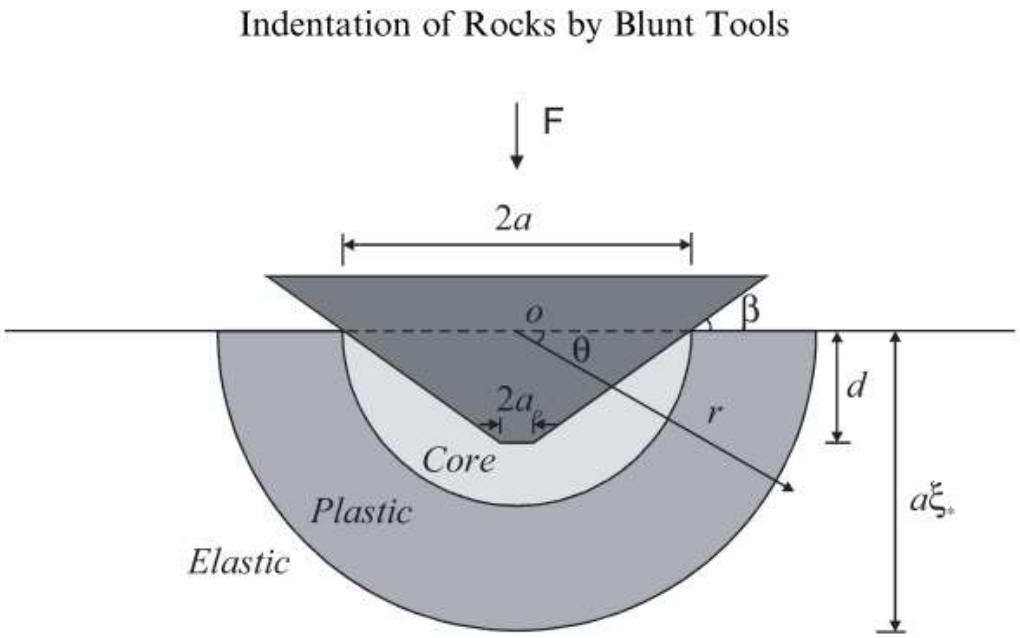

Figure 1.5: Cavity expansion model for a truncated wedge [18]

While these models presented in literature are well founded in physics, there is still room for a more complete interface law for various drill bits created from experimental data in order to validate the models and find possible phenomenon that may lead to further research and model development. Some attempt has been done to build an experimental database for certain bits. Both roller cone bit models presented were validating using a test rig that measures the weight on bit and torque on bit. This experimental validation is important in proving the accuracy of the analytical models and determining any unknown factors that require an experimental value. This particular rig presented by Franca utilized a stationary bit and a rotating rock sample. This bit was pressed into the rock sample with a 2 ½ in roller cone bit to develop a relationship for the rate of penetration vs the weight on bit and torque on bit. This rig shown in Figure 1.6 is only capable of measuring the weight on bit and torque on bit and does not include any fluid circulation. This rig is also somewhat small scale, which may lead to some error in

translating this data over to full scale applications. Another rig presented by Miller and Ball was built for testing impregnated diamond microbits [20]. As inferred by the name, this rig is a very small scale rig only utilizing 20mm drill bits. This rig was used to measure the rate of advance and thrust vs torque, weight on bit, bit wear and rock fracture. While this rig may have been sufficient for the desired tests, it should be considered that at such a small scale, it may not realistically represent the forces acting on a full scale drill bit. Some other test rigs have been developed that include a scaled down drillstring and measure the effects of the frictional forces on the drillstring dynamics [21], [22]. The test rig presented by Liao et al. measured the lateral and torsional vibrations of the drillstring that was scaled 25:1. This drill string had a cylinder at the bottom that represented the bottom hole assembly and would react to the casing wall which would produce friction that was meant to represent some of the frictional forces acting on the drill bit and BHA. The rig presented by Mihajlovic et al. was similar in that it had a scaled drill string and a miniature BHA. The drill string of this set up had a diameter of 2 mm. This one differed from the last in that had a constant frictional torque applied through a disc brake device, as shown in Figure 1.7, rather than only including the friction induced by the casing wall when the BHA came in contact. While both of these models present very valuable information about the effects of the frictional forces acting on the BHA, they represent very small scale setups that could use further large scale validation.

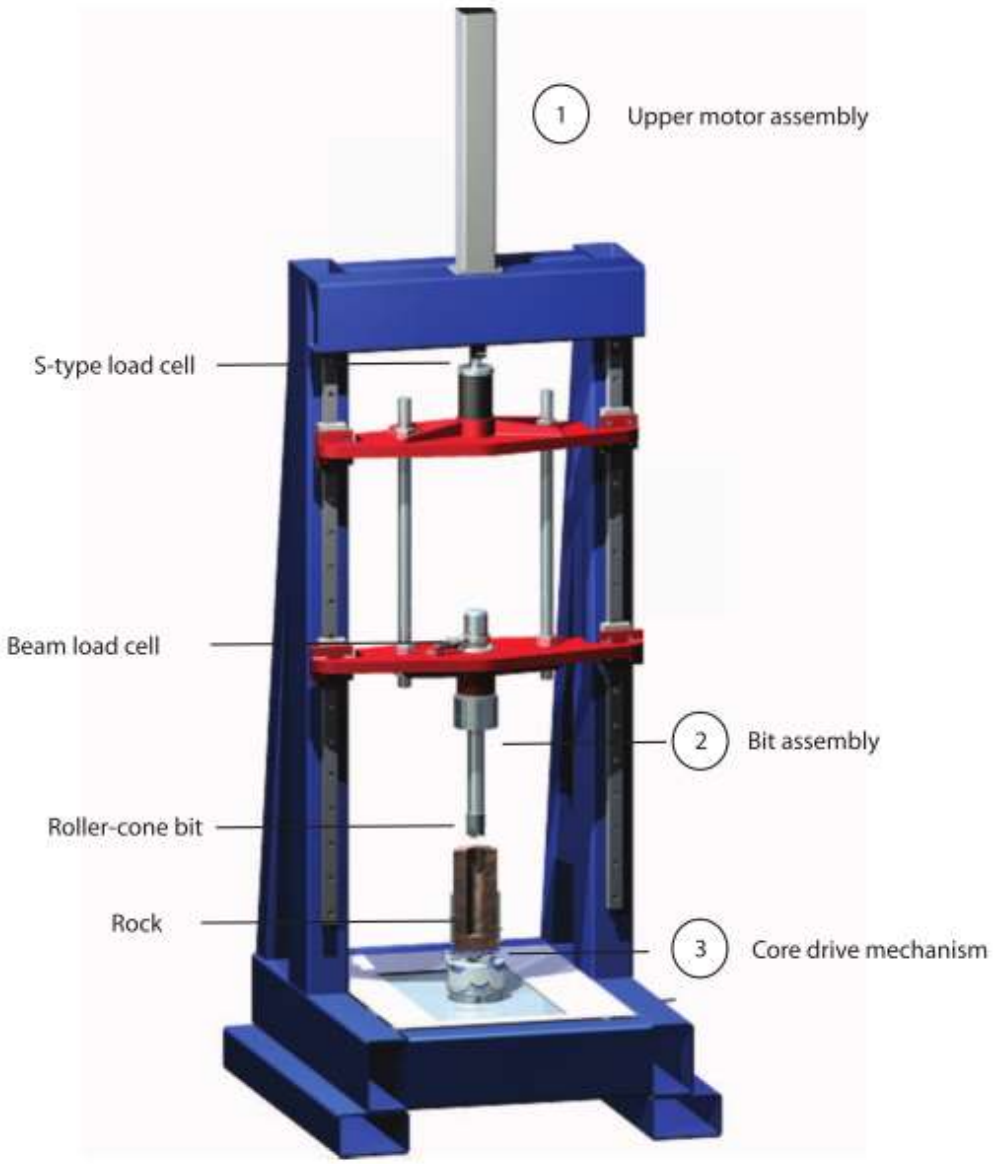

Figure 1.6: Roller cone drilling rig used by Franca [16]

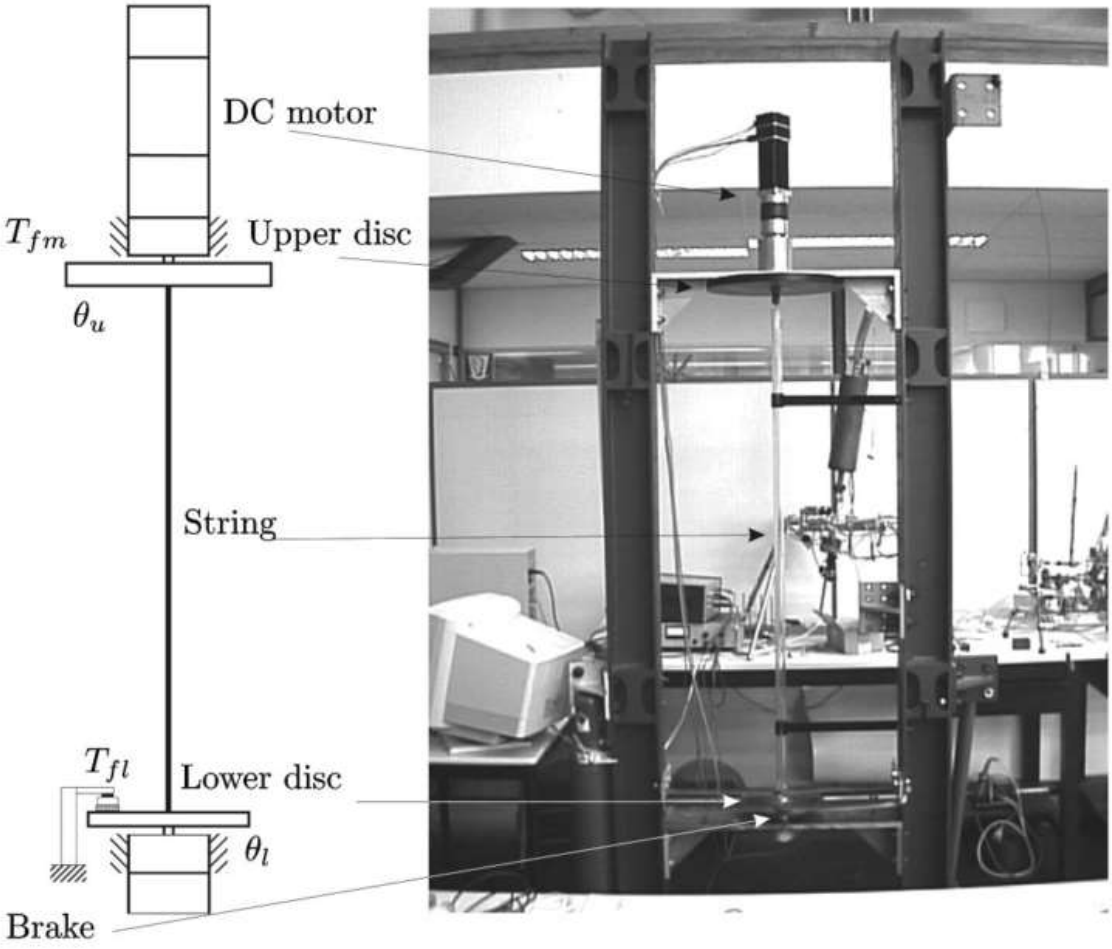

Figure 1.7: Experimental drillstring test rig used by Mihajlovic et al. [22]

There do exist some larger scale force testing rigs that can be found in literature [23], [24]. Two of these rigs were built by MINES ParisTech. The rig presented by Gerbaud et al. can be seen in Figure 1.8 [23]. This rig also measures torque and weight on bit. It does not contain other features such as fluid circulation or ability to measure lateral loads. The rig presented by Amghar et al. is specifically for directional drilling so does have the ability to measure lateral loads. However, it does not include fluid flow and was not used to measure the bit forces but rather the cutting angles and effect from a

prescribed side load. There are other rigs found in literature that are mostly very small scale, or only test on single cutters rather than a full bit geometry.

Figure 1.8: Full scale drilling rig at MINES ParisTech [23]

It should be again noted that these experimental rigs used for measuring bit forces did not include factors such as fluid effects or lateral loads on the bit, which are important factors to consider. The fluid forces provide damping that is important to the

development of the drillstring model. The side loads are an important factor to consider when developing a model for directional drilling and the effects of a side load. All of these factors should be considered and there is room to develop a database for all of these factors that have been discussed. According to literature, there still exists a need for a rig that is capable of accurately measuring the forces on the drill bit that can account for side loads and walking tendencies while including the effects of drilling fluid. There is also still work to be done to develop a more complete database to add to the research that has been accomplished on the existing rigs. This is the overall purpose of this work is to present such a test rig and to use it build on the existing database.

1.2. Scope of Research

The scope and objective of the research presented in this thesis is of three main parts. The first is to analyze, modify and construct a bit force measurement testing rig that was previously designed by Joshua K. Wilson [25]. This work focuses on making the design presented by Wilson into a functional rig. This work not only includes the physical fabrication of the rig, but the design and verification of parts not included or not foreseen in the previous work.

The second part is to create a formation sample and run preliminary tests on the rig. This testing would be used as a basis to understand how well the rig functions and how the data acquisition works under operating conditions. This data will also be used to recommend any further work to be done to make the rig more effective and to incorporate features that would increase the measurements that could be made.

The third objective was to design and build a second test rig to be used at a pre-existing well at TAMU Riverside Campus. This rig would be used to measure the vibrations in the BHA and to validate the dynamic model developed from the bit/force interface law developed from the test data recorded from the former rig.

2. PHYSICAL DESIGN OF RIG

2.1. Bit Force Measurement Rig Introduction

In order to understand the work presented here, it is important to get a background of how the rig was designed and to discuss that various components of the design. The rig was developed to meet the perceived needs of a full scale drilling test rig that can measure the weight on bit, the torque on bit, rate of penetration and lateral loads acting on the drill bit during operation. This rig was also designed to have a mud circulation system to more accurately represent the drilling environment. This rig design would allow for much more flexibility as to the types of tests run on it while attempting to recreate realistic drilling parameters so that a more valid and accurate bit to formation interface law can be developed.

As a summary of the operation of the rig, it utilizes a spinning shaft that is constrained radially and axially. At the end of the shaft is a drill bit, which can be interchanged with different types and sizes. A rock formation sample is then drilled into by being pushed along a track into the spinning bit. Fluid is pumped from a fluid tank into the shaft which flows into the annulus of the drilled hole and is circulated back into a sediment filter and back into the tank. This process simulates the fluid flow in actual drilling operations and is used for cooling, damping and cutting removal. During the drilling process, data is measured and collected from the non-rotating formation sample. To ensure that all of these functions are being realized, the rig consists of various sub-assemblies each with a specific function. An overview of the various parts can be seen in Figure 2.1. As shown in the figure, each sub-assembly is specified by a different color for visualization. These will be discussed in the proceeding sub-sections.

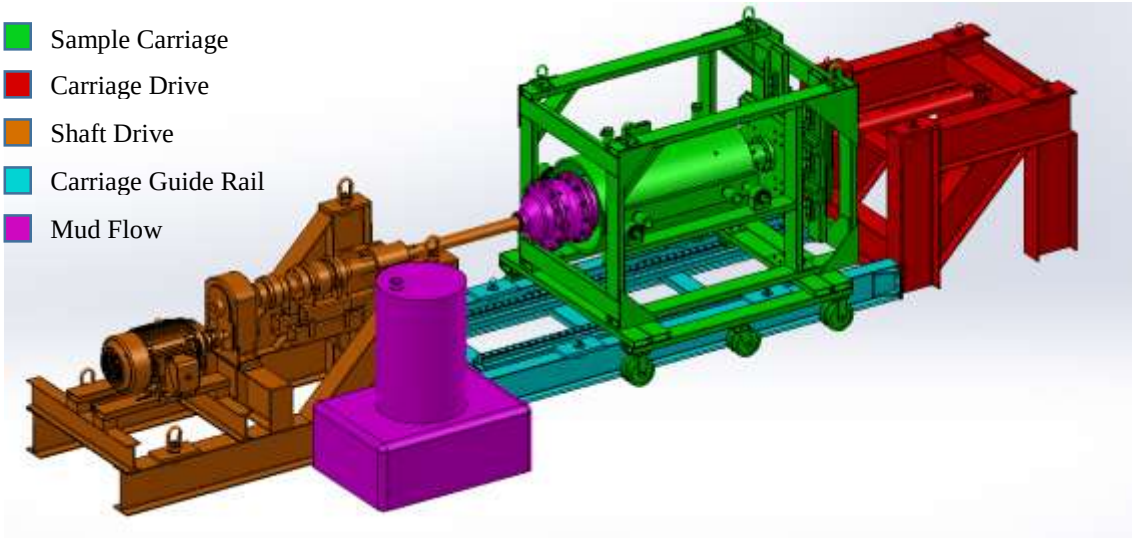

Figure 2.1: Drilling test rig CAD model detailing the main sub-assemblies

2.1.1. Sample Carriage Sub-Assembly

The first assembly to be discussed is the sample carriage. The sample carriage is the heart of the rig and the most complex sub-system as it holds the sample and contains all of the sensors used to measure the various loads during a test. As shown in Figure 2.2, the main purpose of the carriage is to support and measure the formation sample. The formation sample is supported inside a steel cylinder referred to in this work as the sample containment cylinder. This sample containment cylinder is supported by all load sensors used to collect data for the test rig. At the back end of the sample containment cylinder is a large torsional/axial load cell. This load cell is rated to 150000 lbf axially and 200000 lbf*in in torsion. This load cell is supported on the opposite end with a 2 axis rail system as an attempt to negate any bending loads on the load cell from misalignments in the sample containment cylinder. The outer wall of the sample containment cylinder is supported by 8 rods which constrain the sample laterally and measure any lateral loads. While the primary purpose of these lateral load rods is to measure any lateral forces acting on the formation, a secondary purpose is to measure

any frictional loads in the axial or torsional direction caused by the rods themselves. Ideally, all of the axial and torsional load would be carried and measured by the load cell. However, in order to get more accurate results, these frictional loads are measured as well. The lateral load rods are supported by the rod support cylinder. This cylinder is then supported by the structural frame of the sample carriage.

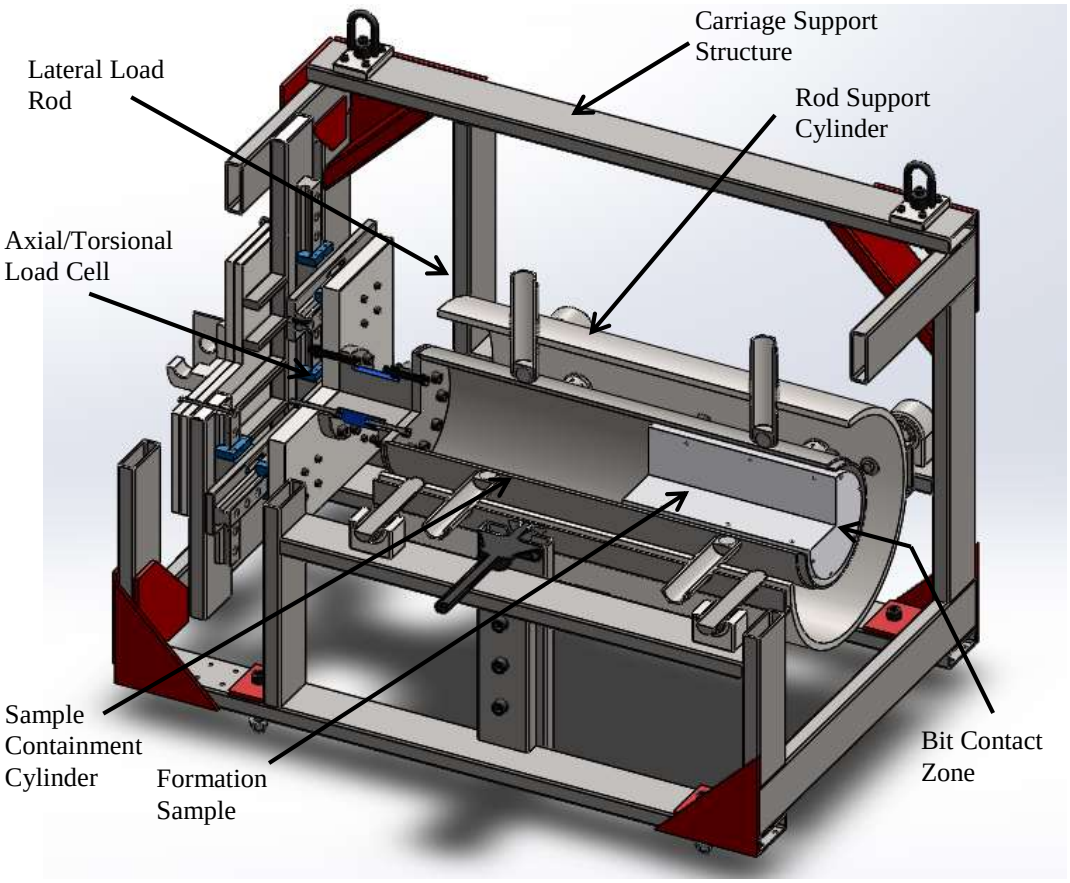

Figure 2.2: Section view of sample carriage assembly

As part of the discussion of the sample carriage assembly, it is important to discuss the design of the lateral load rods. A key element to the functionality of the lateral load rods is the use of strain gauges. As such a brief discussion of strain gauges is mentioned here.

Strain gauges are most often set up in a circuit such as a Wheatstone bridge. A Wheatstone bridge is a circuit designed to measure the change in resistance of one or more strain gauges by utilizing the change in voltage. This is necessary because the actual change in resistance of a strain gauge is very small and difficult to measure [26]. A diagram of a Wheatstone bridge can be seen in Figure 2.3.

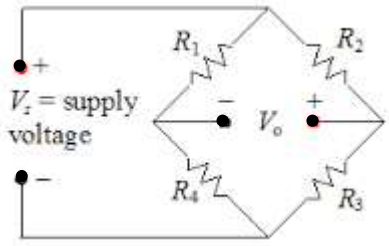

Figure 2.3: Wheatstone bridge circuit

The Wheatstone bridge is often used for just a single strain gauge and 3 known constant value resistors. This is known as a quarter bridge set up. Due to the simplicity and commonality of this set up, it was used for the rod axial measurement gauges. However, it is common for gauges measuring bending moments to use a half bridge, which is where two strain gauges are used [27]. The reason for this can be understood by examining the equation determining the output voltage.

$$V_0 = \frac{V_{ex} R_2 R_3}{(R_2 + R_3)^2} \left(\frac{\Delta R_3}{R_3} + \frac{\Delta R_1}{R_1} - \frac{\Delta R_2}{R_2} - \frac{\Delta R_4}{R_4} \right) \tag{2.1}$$

Consider the case where the strain gauges are placed on opposite sides of the rod and are wired in positions R_2 and R_3. If a bending load is on the rod, the output will be double that of a single strain gauge, which increases the sensitivity. If the rod is placed under an axial load, both gauges will have the same reading, and will cancel each other out

causing V_0 to go to zero. So in summary, a half bridge configuration allows for a built in mechanism that theoretically removes coupling between bending and axial forces.

Each lateral load rod is fixed with 6 strain gauges used to measure loads along the local coordinates on the rod as shown in Figure 2.4. Two of these gauges are wired in a Wheatstone quarter bridge configuration and are used to measure the rods local axial load, Z_R, which is a global lateral load. This is a direct measurement of the strain induced by the axial load. The other four gauges are wired into two sets of Wheatstone half bridge configurations. These bridges measure the rod's local x and y axis, X_R and Y_R , which translate to global WOB and TOB frictional components. These measurements are indirectly measure loads in the X_R and Y_R directions by measuring the strain induced by the bending moment from these loads. For reference, the global measurement system coordinates are shown in Figure 2.5.

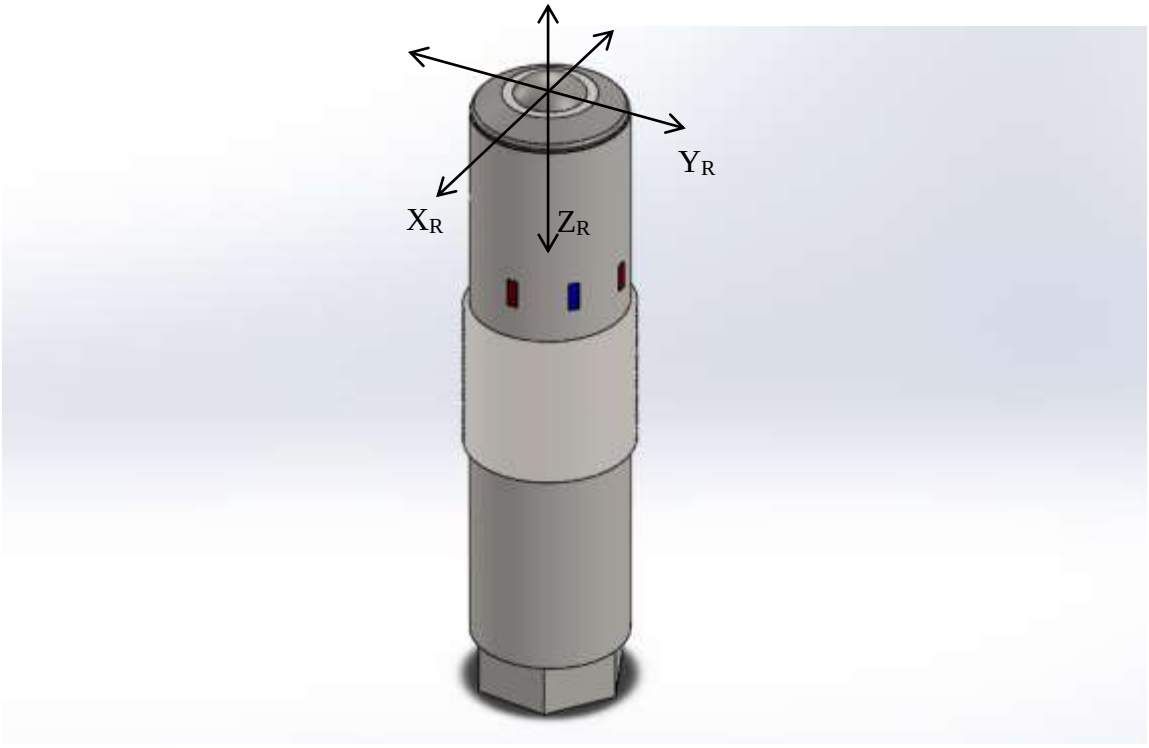

Figure 2.4: Lateral load measurement rod and local coordinate system

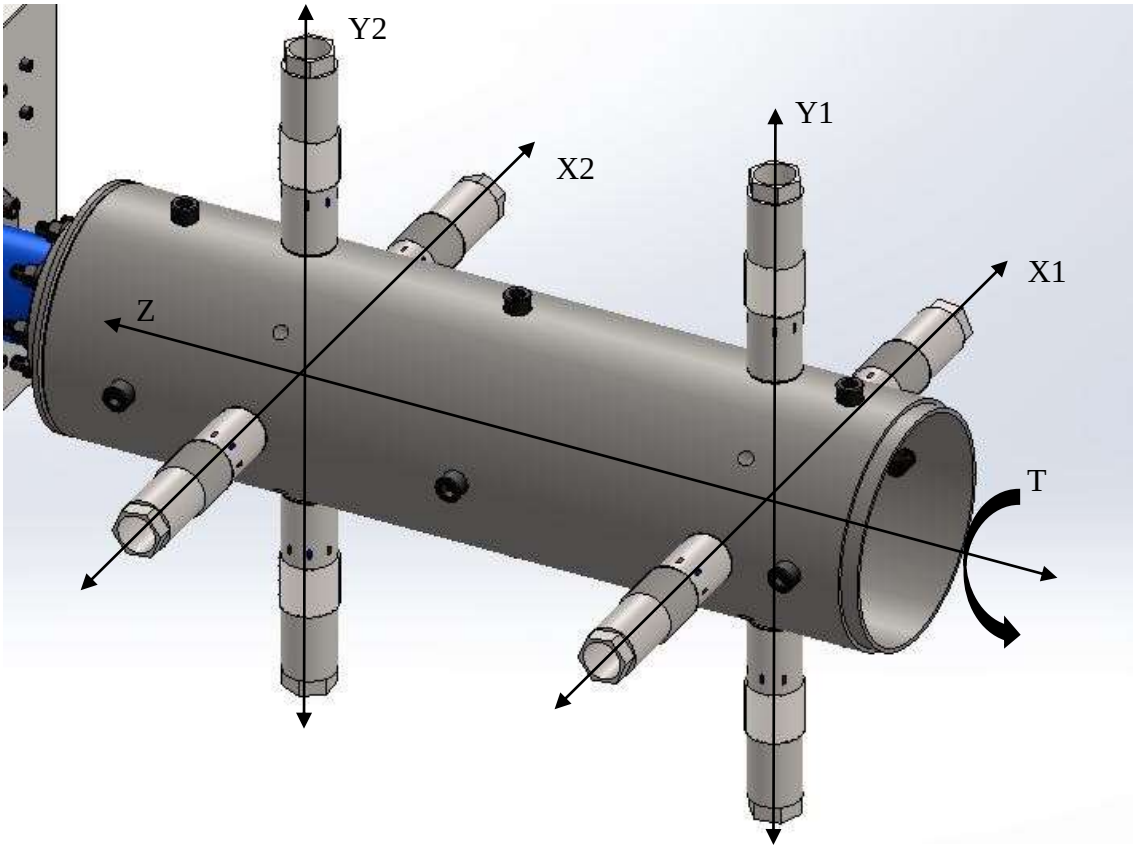

Figure 2.5: Global coordinate system of test layout

2.1.2. Carriage Drive Sub-Assembly

The second main sub-assembly to discuss is the carriage drive system shown in detail in Figure 2.6. The main function of this part of the rig is to house and support the hydraulic cylinder that is used for the sample carriage actuation. This sub-assembly is crucial to the design because it provides the ability to apply a high WOB as the formation sample is pushed into the rotating drill bit. The hydraulic cylinder used in this assembly has a 4" bore and a maximum pressure of 3000 psi. This translates to having the capability to apply a weight on bit of up to 28,000 lbf. However it is recommended that all tests are carefully monitored to prevent the WOB from exceeding 20,000 lbf to ensure a safety factor on all rig components.

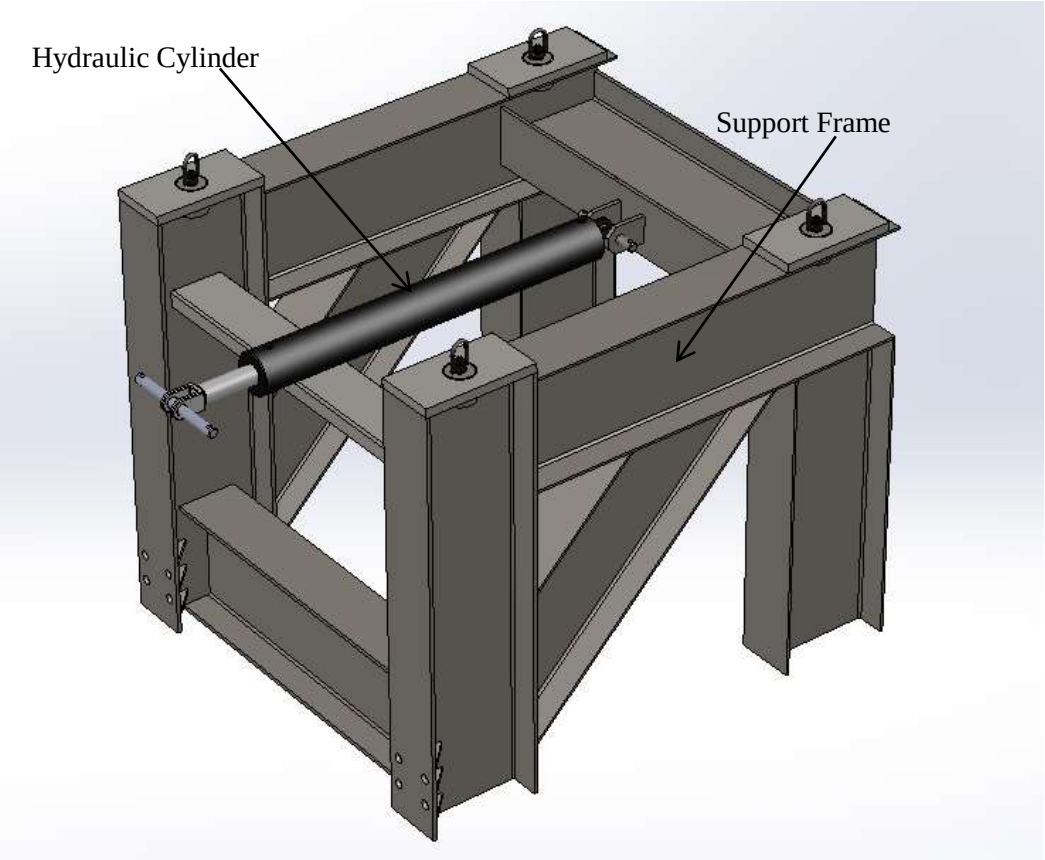

Figure 2.6: 3D CAD Model of Carriage drive assembly

2.1.3. Shaft Drive Sub-Assembly

The next main sub assembly is the opposite end of the drive system, which is the shaft drive system. This system consists of the drive motor, a speed reducing gear box, shaft bearing housing, the drill shaft and drill bit. These crucial components are fixed in place on a rigid support frame.

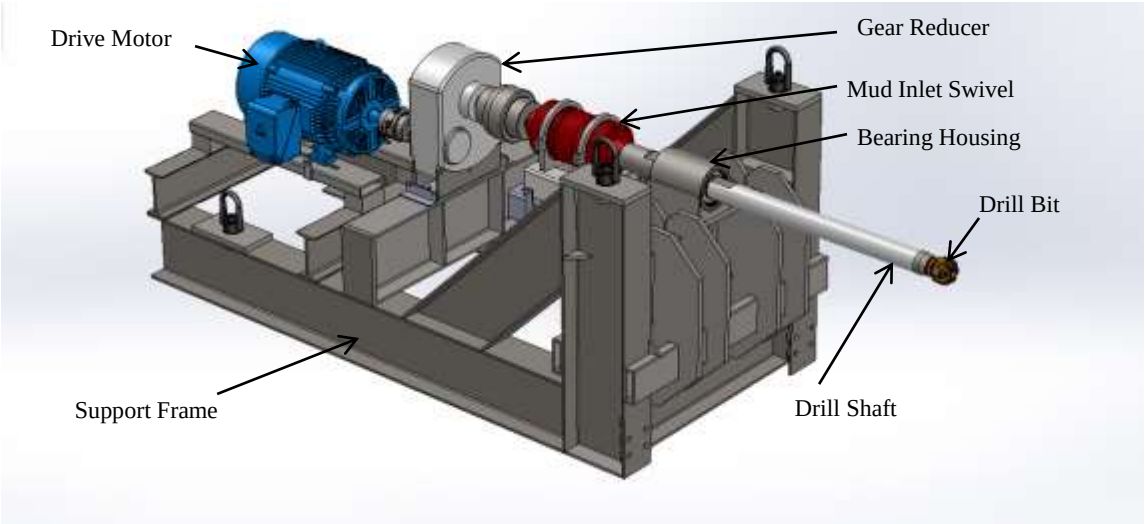

Figure 2.7: 3D CAD model of the drill shaft drive assembly

This system is driven by a 40 HP 3 phase NEMA B electric motor. The output of this motor goes through a 15:1 gear ratio which reduces the max speed from 1750 RPM to about 115 RPM which is more in the range of actual drilling applications. To find the torque capacity of the drive, the torque curve of a NEMA B motor was used as shown in Figure 2.8.

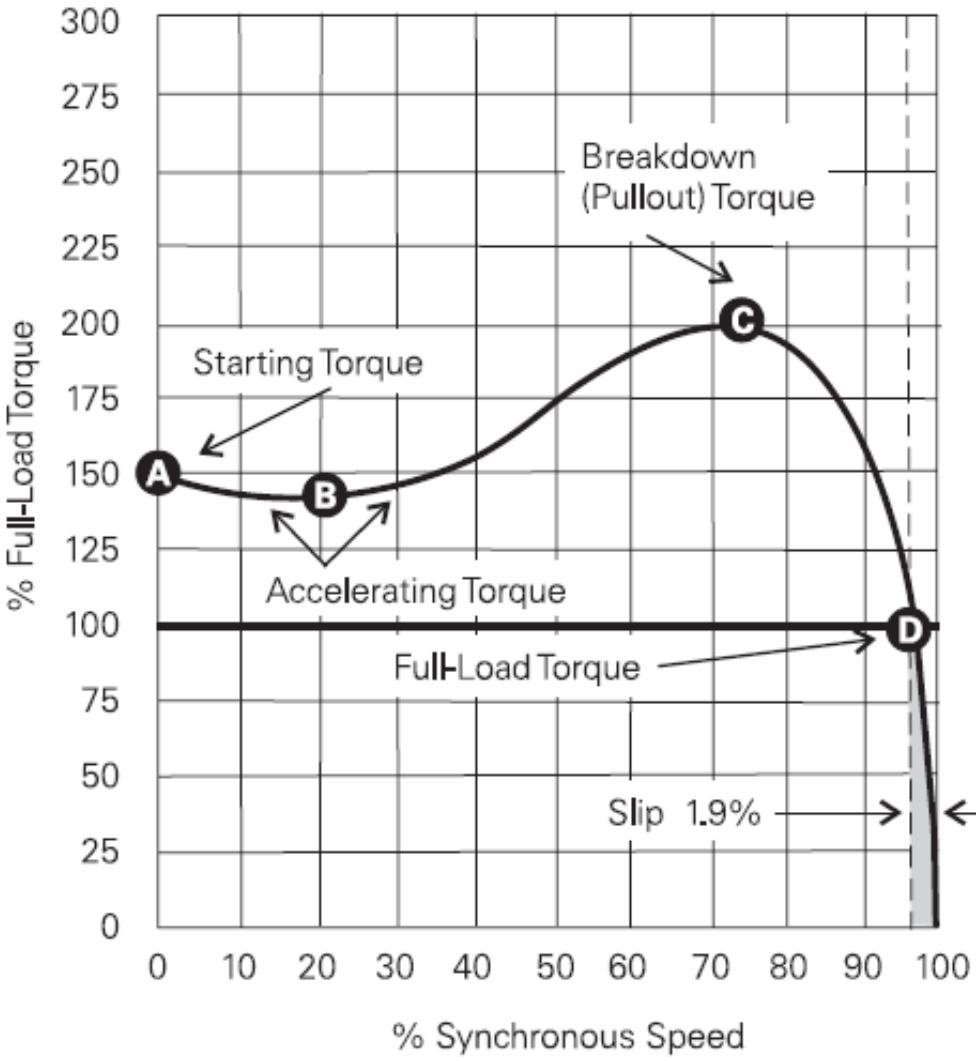

Figure 2.8: Generalized speed to torque curve of NEMA B AC motors [28]

From the rated power and speed of the motor, the maximum torque produced by the system can be calculated. The full load torque of the motor can be calculated using the relation

$$P = T\Omega \tag{2.2}$$

where P is power, T is Torque and Ω is rotor speed. Using this relation and applying the necessary conversion factors, this relation becomes

$$T = \frac{5252 \times HP}{RPM} \tag{2.3}$$

Using the rated RPM and the rated HP of the motor, this relation gives the full-load torque as 120 ft*lbf. Referring back to Figure 2.8, the maximum torque output of the motor, or the breakdown torque, is approximately 200% of the full-load torque. This means that the maximum output torque of the motor is 240 ft*lbf. After the gear reduction, the max output torque of the drill shaft is about 3600 ft*lbf or 43,000 in*lbf.

2.1.4. Carriage Guide Rail Sub-Assembly

The carriage guide rail has only two purposes. The first purpose is to create a linear path to ensure that the sample carriage is directed parallel to the shaft. This function ensures that the drilling path is straight and controlled. The second purpose is to act as a structural support the entire carriage assembly during operation. The isolated CAD model for the rail system can be seen in Figure 2.9.

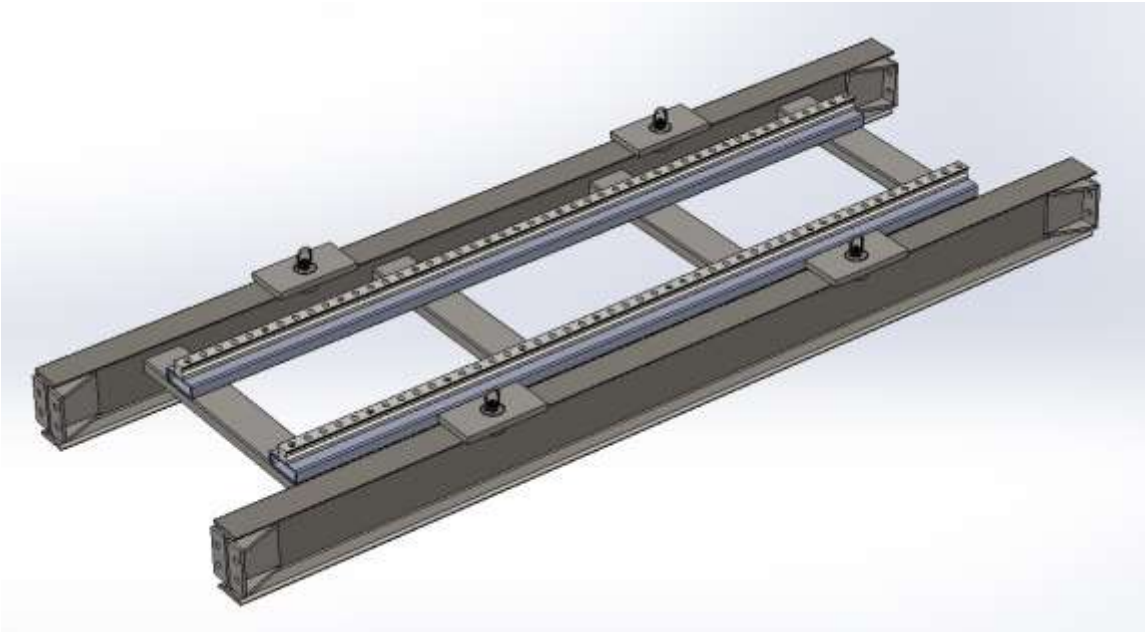

Figure 2.9: 3D CAD model of carriage rail system

2.1.5. Mud Flow Sub-Assembly

The final sub-assembly of the test rig is the mud flow system. In the drilling industry, the drilling fluid is often referred to as mud. This convention will be used throughout this work. The mud flow assembly of the rig consists of the mud tank, the mud pump, the mud drain and the sediment filter. The components of this sub-assembly and the flow path of the mud can be seen in Figure 2.10.

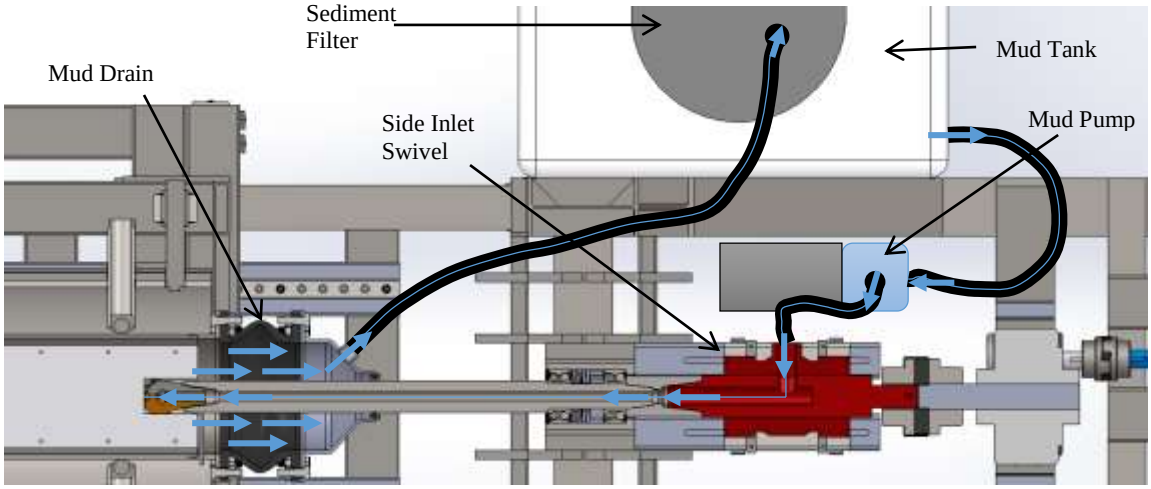

Figure 2.10: Diagram of drilling fluid flow path through the mud flow system

As shown in Figure 2.11, the mud drain system includes the formation sample container fluid outlet, and the dynamic shaft seal to prevent the escape of fluid at the drain to shaft interface during operation. This system connects directly onto the sample containment cylinder with a threaded connection and utilizes a rubber expansion joint to reduce the amount of lateral vibration to be transmitted to the shaft other than at the bit. The other side of the expansion joint houses a dynamic shaft seal which retains fluid on a moving shaft.

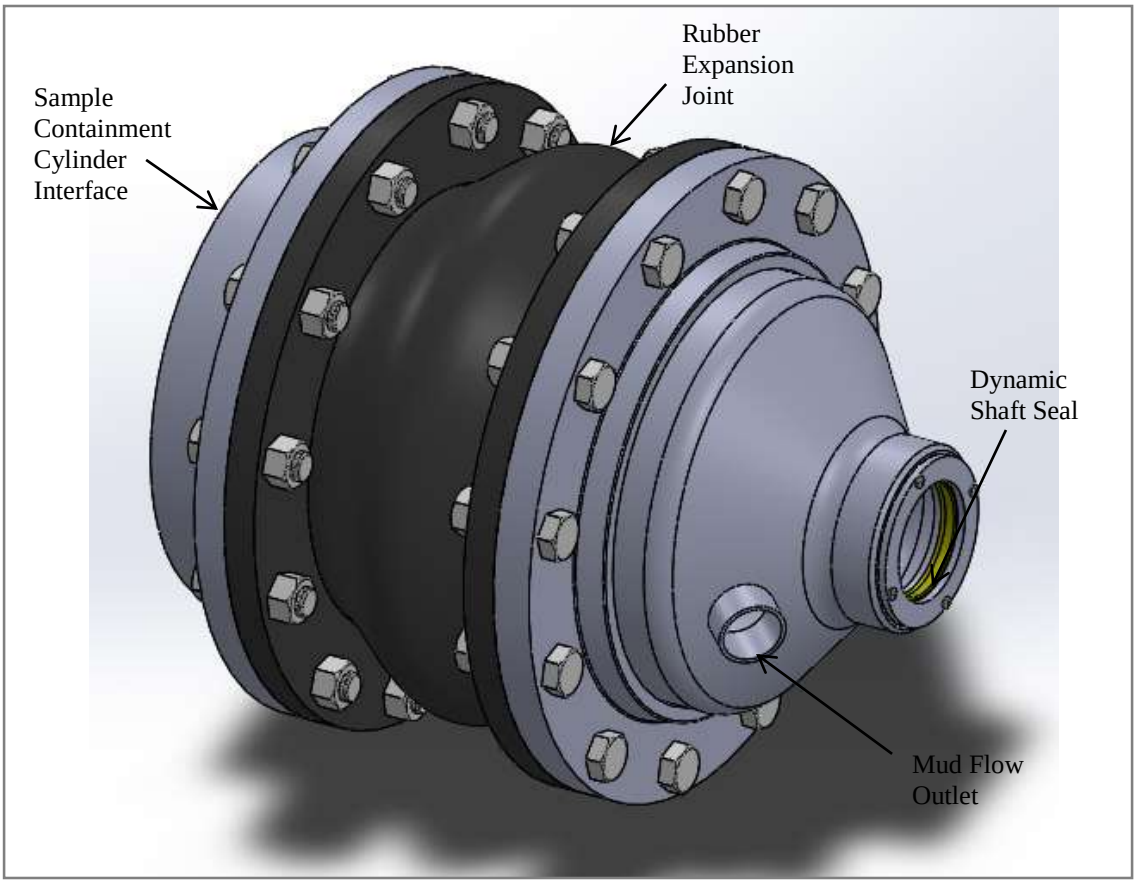

Figure 2.11: 3D CAD model of formation sample mud drain assembly

The mud tank is used to store the drilling fluid so that there is a sufficient reservoir for the mud pump to ensure a continuous flow and to prevent cavitation. Since the mud flow system is directly involved with the drilling interface, it is important for there to be a way of filtering out the cuttings produced during the test so they aren't circulated back through. This circulation of the cutting could cause damage to the pump and clog up the system which would negatively impact the drilling efficiency and cause issues with the pump flow. The purpose of the sediment filter is to remove these cuttings so that clean fluid is constantly being circulated. A discussion of the design of the sediment filter will be covered in the next section.

2.2. Rig Component Design

Although the majority of the rig design was finalized before the work presented in this thesis, there were modifications and additions that needed to be made in order to complete the rig. Many components had to be redesigned to meet new design criteria, improved functionality or to reduce cost. Some of these design changes were minor, such as additional shims or a change of coupling type. Some other changes were more drastic and required more attention. A general discussion of the major components of design work put into this research project is discussed in the following sections.

2.2.1. Drill Shaft Assembly

The drill shaft assembly required the most design work. One of the driving factors in the drill shaft and bearing housing design was the decision to use double row angular contact bearings. The original design used thrust bearings and a complex housing to properly preload the bearings as shown in Figure 2.12 [25]. This solution is an ideal solution for an application where the bearings are under high thrust loads for long periods of time. However, this system required a very specific preload and housing to function as designed. After analysis of the rig and an estimate of how long tests would be run, it was concluded that the tests would be run over short periods of time due to the stroke of the rig dictating how far it could drill into a sample in one run. Since this is a low speed, low use rig, a high complexity bearing system was unnecessary.

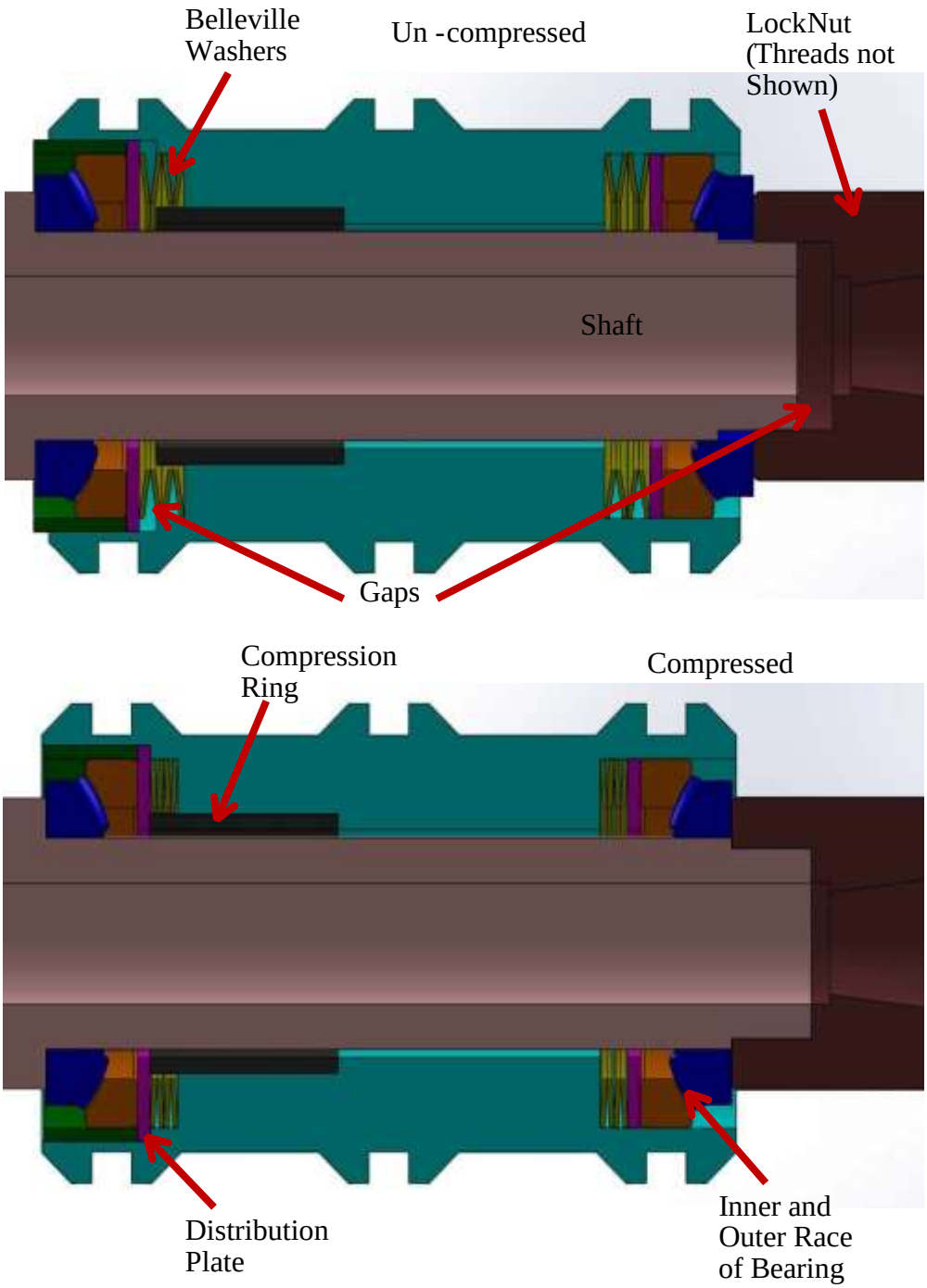

Figure 2.12: Original design of bearing assembly utilizing thrust bearings [25]

It was determined that double row angular contact bearings would be utilized as the bearings for the system. These bearing were chosen due to their relatively low cost compared to thrust bearings and their high radial and thrust capacities without requiring a preload. The bearings that met size and load requirements were SKF 5314A double row angular contact bearings. Based on information requested from SKF applications, these bearings are rated to a radial capacity of 36,600 lbf and a total thrust capacity of 27,000 lbf. It should be noted that this is the maximum capacities for both thrust and radial and it is not rated to support both maximum loads simultaneously.

Due to the change in bearings, the housing was redesigned to reduce the high machining cost of the complex preloading housing designed for the thrust bearings. The housing was redesigned as a bore as shown in Figure 2.13. This design allowed for easier assembly and a much lower manufacturing cost while remaining very functional for the angular contact bearings. Along with the simplified internal design, the external design was simplified. The former design had groove features for mounting brackets to fix the housing in place which can be seen in Figure 2.12. The new design has a smooth cylindrical external surface which is welded to a support frame as shown in Figure 2.14. This welded structure is bolted directly to the drive assembly support frame. This reduced cost drastically while keeping the important feature of having the shaft and bearing housing removable for service or modifications if needed.

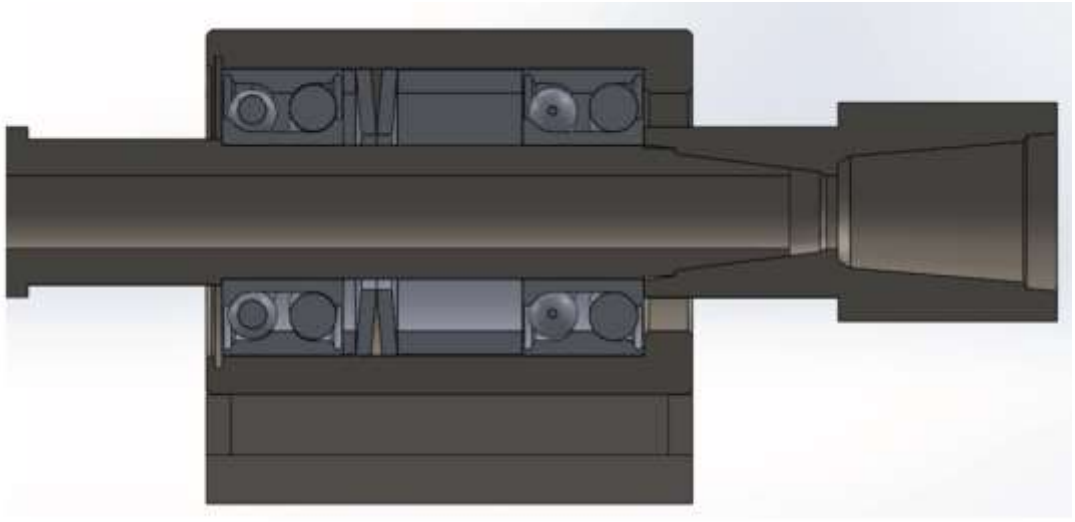

Figure 2.13: Redesigned bearing assembly for double row angular contact bearings

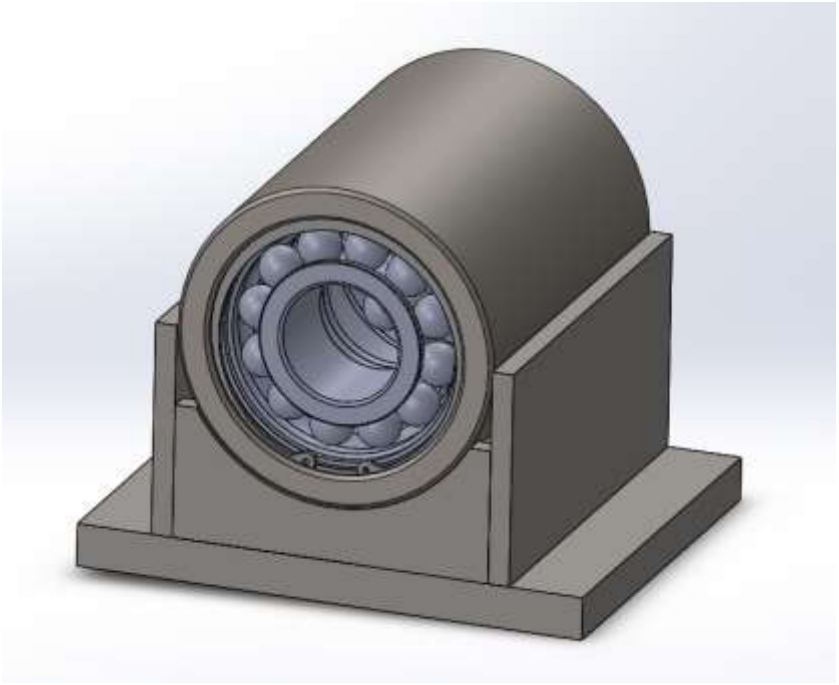

Figure 2.14: 3D CAD model of bearing housing assembly

Although an axial preload is not required or recommended for these bearings, the current design can use a preload to attempt to distribute the axial load transferred from the WOB. The Belleville washer preload system was retained from the older design. Without a preload, nearly all of the load will be supported by the rear of the bearings due to very slight ball clearances, .03 mm, and housing spacer tolerance. However, assuming rigid bearings, the weight could be distributed with the addition of a preload. Assuming that the effects of the clearance gap are negligible at loads high enough to approach the rated capacity of the bearings, Figure 2.15 shows the load distribution of each bearing normalized to the value of the preload. The negative reaction force seen when there is no applied load is due to the rear bearing being preloaded in the opposite direction as the assumed WOB.

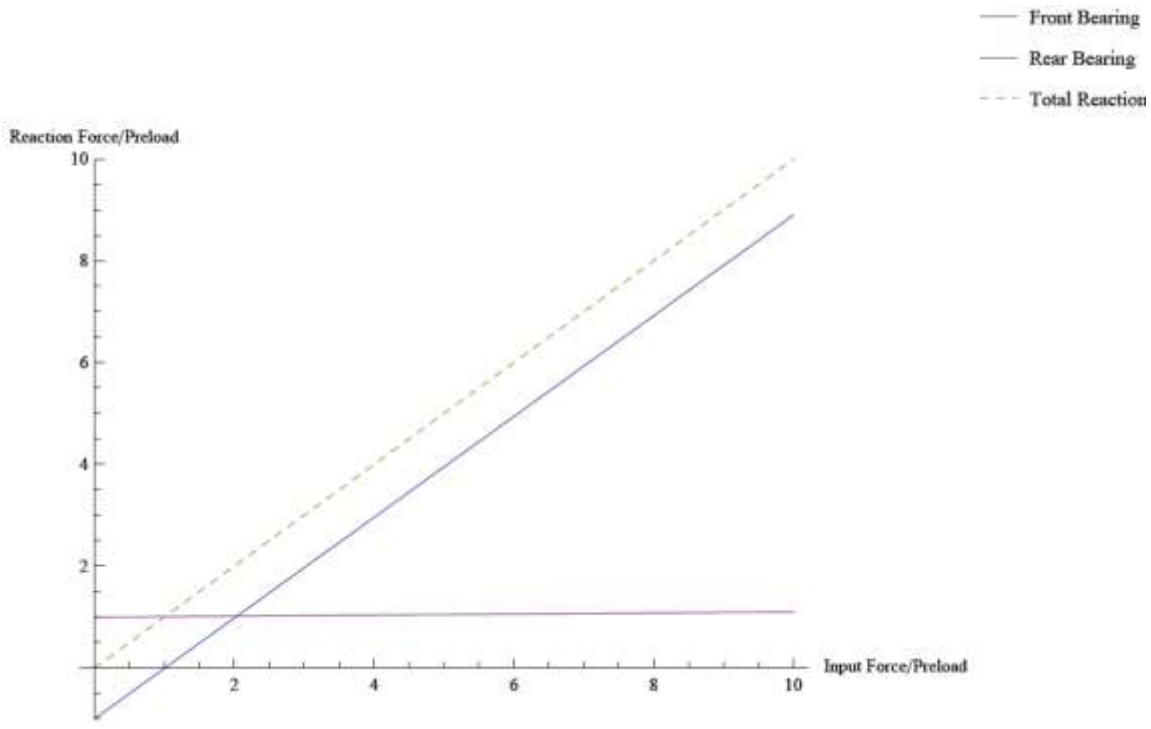

Figure 2.15: Normalized bearing load distribution with bearing preload.

Due to the assumed loads of the drilling process and the ability to control the rate of penetration, for the current time, it was decided to not preload the bearings. For this reason it is recommended that the applied WOB does not exceed 20,000 lbf to ensure that the bearings have a longer life in the rig.

The shaft itself also went through some minor modifications. It was initially proposed to have a custom straight thread on the back end of the shaft. Many drilling components are built off of American Petroleum Institute (API) standards. These threads are called box threads for internal threads and pin threads for external. The mud inlet swivel that was chosen and purchased for the rig has a 3 ½ inch internal flush API standard pin thread on the end that would need to be coupled to the shaft. The straight thread on the shaft would require the fabrication of a custom part to couple swivel to the shaft. In attempt to make all components fit together better and to plan for the possibility of future work making the rig more modular, the thread type was modified to be an API standard thread. The size chosen for the back was the same thread size that is standard for the drill size that was chosen for the rig. This size chosen was a 2 3/8 inch regular API thread. This allowed for the purchase of a drill sub, which is a short section of drill pipe with a box thread on either side used to connect two sections of pipe together of the same or different size. This standard part purchased as a coupling was only $275 while the

custom part was quoted to be $800. The drill shaft and bearing assembly can be seen in Figure 2.16.

Figure 2.16: Assembled drill shaft and bearing housing assembly

2.2.2. Formation Sample

The formation sample was initially intended to be a concrete mixture made directly in the sample container cylinder. This method utilizes the steel tube to provide some tensile strength to sample. This negates the need to add any internal structure but it creates other problems that are difficult to solve. The first issue is that it requires the sample container cylinder to be removed to add a sample. To make the clearance necessary to remove the sample containment cylinder, the drill shaft must first be removed. This requires additional work and steps that could be avoided. Another major issue with this method is

taking into account the scenario where the concrete sample would have to be replaced. In order to remove the sample containment cylinder, the bolts at the bottom of the sample container must be accessed. This could be solved by making these mounting holes threaded. However, the sample containment cylinder was one of the components manufactured before and thus threaded holes could not be made that would fit with the load cell. With the current design of the load cell being bolted onto the bottom, removing the cylinder would require removing all of the concrete before the bolts could be accessed. This adds another design problem as to what methods could be used to remove the concrete and how effective it would be. It turns out to be a very difficult design problem to remove all formation sample and to be able to effectively remove all of it with a wide range of material properties based on what the composition of the is. Another issue is the amount of material that would be wasted by utilizing the entire length sample containment cylinder. It should be noted that the stroke of the hydraulic cylinder is only 36” and the sample container cylinder is 48”. After accounting for the position of the sample carriage before the bit touches the concrete, there is only about 20” of stroke left for drilling. This shorter effective stroke and the sample removal problems led to the design of a shorter concrete sample that could be made on its own and inserted into the sample container cylinder.

It is known that concrete does not have a lot of tensile strength so it is important to reinforce the concrete sample so that it does not break under the load of drilling. This is a disadvantage of a short sample that is made separate from the containment cylinder since a feature must be added into the design of the sample. In this case, the concrete sample was designed to be reinforced with a rebar skeleton as shown in Figure 2.17. This rebar reinforcement gives the sample needed tensile and hoop strength while drilling.

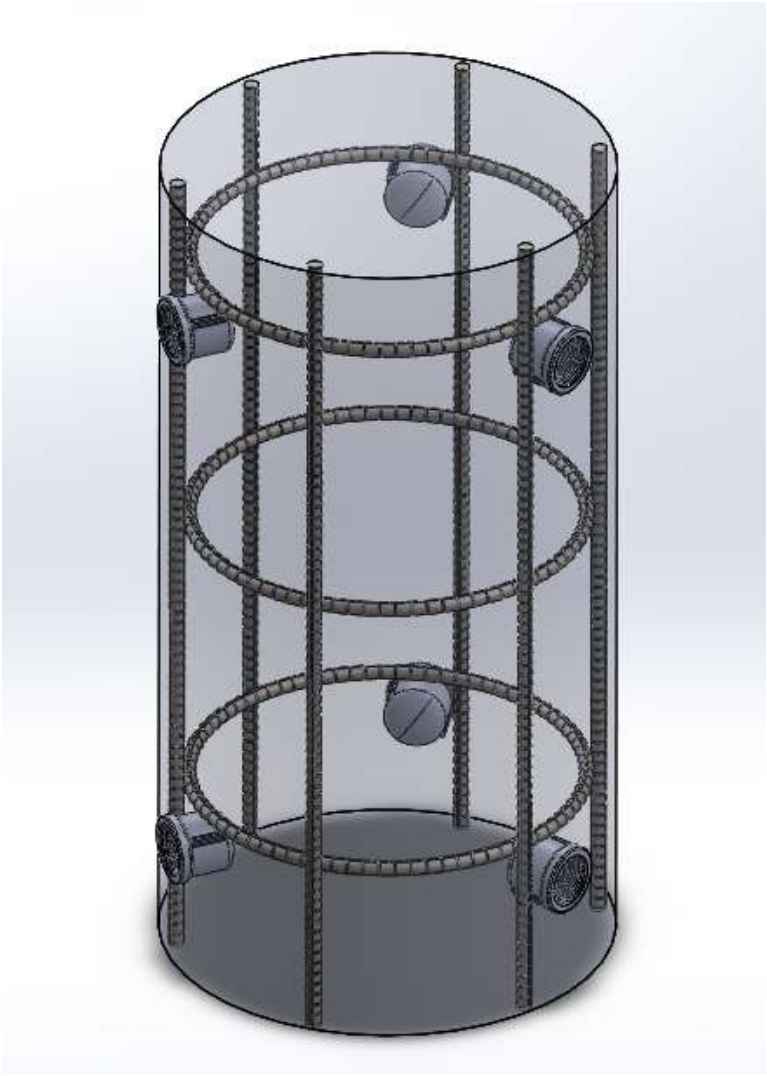

Figure 2.17: Rebar and cup layout of the formation sample mold

Since this concrete sample would be inserted into the existing sample cylinder, there was a need for a mechanism to hold the sample into place. As a holding mechanism for the sample, two rows of three holding screw mounts were added to the cylinder. These would be used to mount set screws to hold that formation sample. To increase the effectiveness of these holding screws, cups were incorporated into the mold of the concrete sample to distribute the force of the holding screws so that the concrete would

not break at the holding points. This rebar and cup skeleton was made using tie wire and put into a 22” section of a 12” diameter concrete mold cylinder and filled with a concrete mixture as shown in Figure 2.18. The cups were protected from concrete leakage by inserting wax coated screws directly into the cups before the concrete was poured into the mold. The formation sample made for the initial testing stages is shown in Figure 2.19 as an example of how a finished formation sample looks like.

Figure 2.18: Formation sample mold

Figure 2.19: Finished formation sample used for initial testing

This concrete sample, depending on exact composition, weighs a little less than 200 lbf while the steel sample cylinder weighs about 330 lbf. This requires less need for equipment and can be set into place with only a few people. It also creates a much better solution in loading the sample cylinder by not requiring the shaft to be removed.

The recommended method to insert and remove sample cylinders is to unthread the mud drain assembly and slide it to the back end of the shaft and remove the bit. Then remove the hydraulic cylinder pin and pull the carriage back by directing the cylinder above the back support beam as shown in Figure 2.20. This creates enough clearance to lift the formation sample up between the shaft and the cylinder and then slide it into place. This is easily performed with five people, having set the cylinder on two lifting rods. Four can lift while the fifth person slides the sample in once the sample is lifted to the correct height.

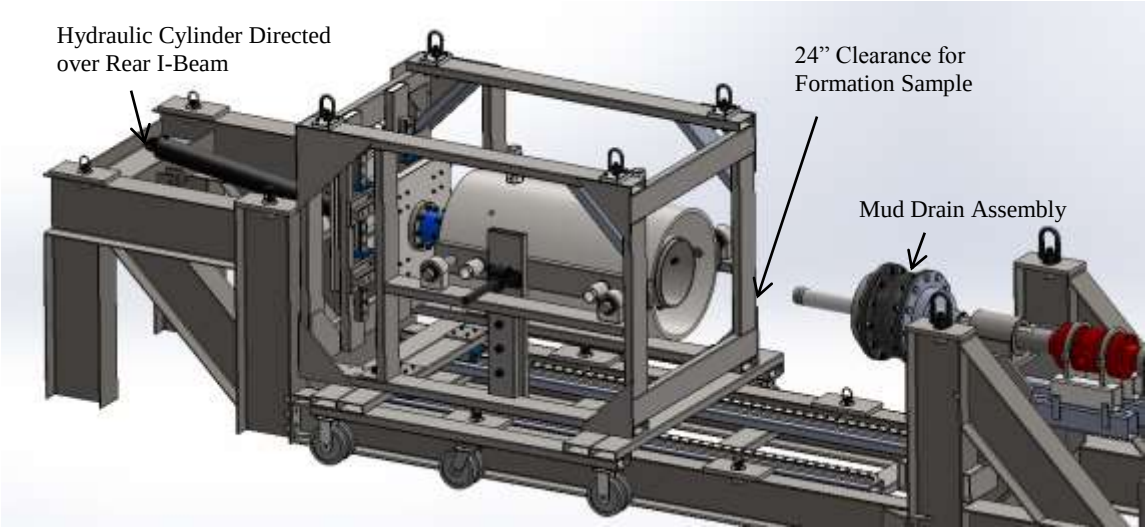

Figure 2.20: CAD Model showing the repositioning of the hydraulic cylinder and the drain assembly for sample loading

2.2.3. Mud Tank and Filter

The mud tank is an important component for the rig to work as intended. One of the purposes of the rig is to measure the effect of fluid forces on the vibration of the drillstring. The need was a large enough tank to hold enough fluid to circulate through the entire system while still having enough fluid for the pump to draw from. It was measured that to fill all hoses, drill shaft, sample container cylinder and mud drain cap would require approximately 42 gallons of fluid. With this measurement it was determined to have a tank that could provide at least double to ensure proper circulation and to provide a large reservoir to help with cooling. A simple solution was to purchase a bulk material tank as shown in Figure 2.21. This tank has a 110 gallon capacity and has a 1” NPT drain hole at one end that is be used as the port to attach the pump suction hose to with the use of a pipe reducer.

Figure 2.21: 110 gallon plastic tank used as the mud tank

Having a fluid tank is not all that is needed for a drilling application. Although the pump chosen was designed to handle thick fluid, it is never recommended to run debris through the pump such as rock formation cuttings produced from the drilling process. Circulating cuttings back into the drilling interface would also cause clogging and reduce the bit effectiveness. This could cause the bit to be incapable of cutting and cause the WOB to exceed the rated value of the system and damage important components of the bit. This provides the necessity to design a filtration system to remove the majority of the sediment produced before it is recirculated back through the pump.

A few concepts were developed for a filter solution. The simplest solution was to put a filter cap on the outlet of the mud tank. This solution has a flaw in that the filter would get clogged very quickly and would prevent the fluid from flowing into the pump. Another solution was an overflow system, creating a sediment collection basin. This concept involved having two tanks next to each other with a U shaped cut in both of them creating an overflow as shown in Figure 2.22. This concept is also a simple concept that could be very effective at preventing the recirculation of the cuttings. However, this concept requires a large amount of space to put two tanks side by side. It also has the problem of being very difficult to clean and empty. At some point there will

be enough cuttings that there is no longer any filtration, so it is of crucial importance to be able to remove the cuttings. Another issue is accurately cutting the overflow channel between the tanks and properly sealing it. While these issues can be solved, the space and the cost of purchasing two tanks led to further concept development.

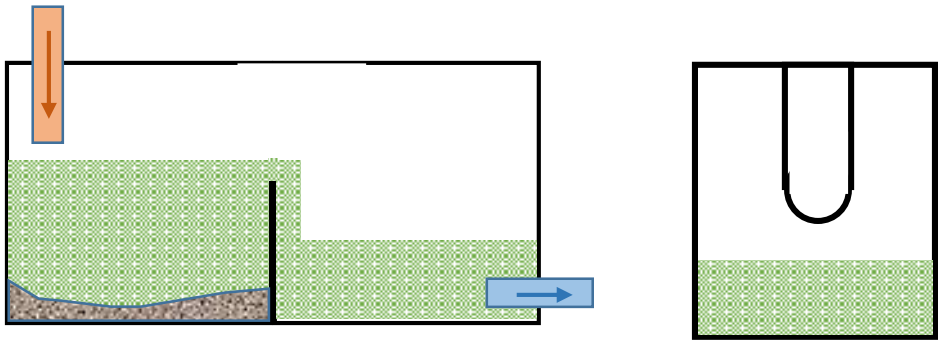

Side View Cross Section Front View

Figure 2.22: Early concept of overflow style filter

Figure 2.23 details the current design of the mud tank and filtration system. The final design involved a hybrid design of the two concepts presented previously. The main idea of the concept is to have a filter tank that could easily sit on top of the mud tank. This was ideal due to the 5 in. diameter hole on top of the chosen bulk tank. The filter tank was designed to be cylindrical with a smaller cylinder in the center. The inner cylinder would act as a pipe flow inlet into the tank. As shown, this filter to tank transfer tube is raised up requiring the tank to be partially filled before the fluid will overflow into it. By requiring the fluid to reach a certain lever before flowing into the tube, this concept becomes very similar to the overflow style filter. The bottom of outer cylinder becomes

the sediment basin and the tube becomes the overflow channel. This tube would also extend below the tank inlet to ensure all of the fluid flows into the tank and doesn't leak over the edge of the mud tank. This also improves the stability of the filtration tank by preventing it from tipping over. For additional filtration, the top of the filter to tank transfer tube is covered with a mesh filter that removes any sediment and debris that does not settle to the bottom of the tank.

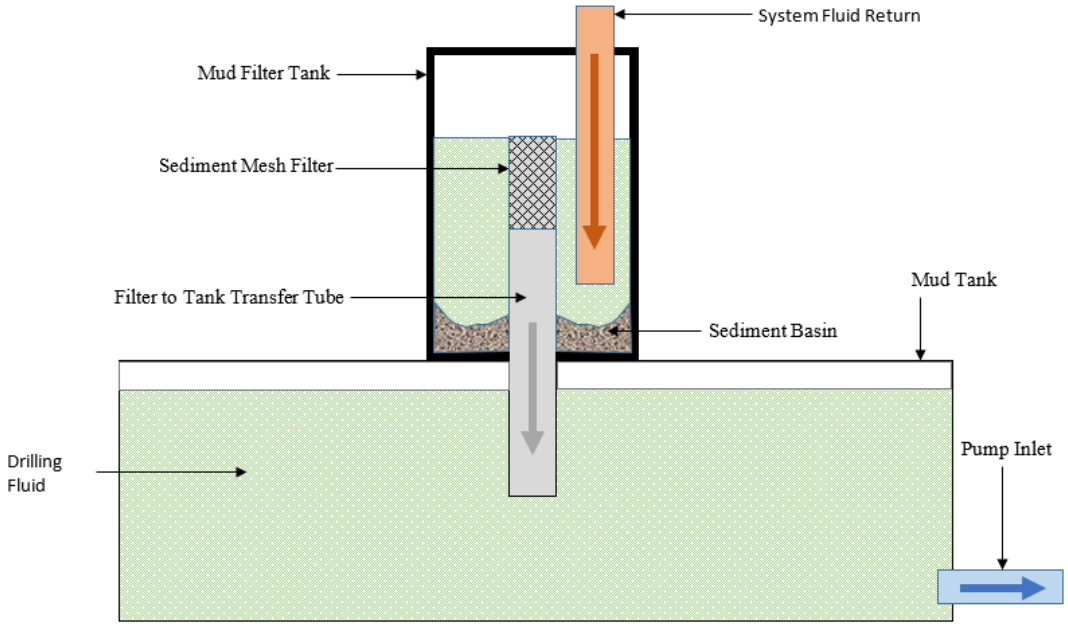

Figure 2.23: Cross-sectional diagram of the final mud tank and filter assembly

This concept was preferred over the other concepts for a number of reasons. The first reason is that it implements the strengths of both filtration concepts which helps ensure that the circulated fluid is clean and free of debris. Another major advantage comes from the smaller size and the ease of removing the tank. This smaller size makes the filter much easier to empty and clean in between tests. However, this also makes the filter quicker to overflow if there is a clog at the mesh filter. The last advantage is that it was very easy to assemble and a very low cost. The final solution to build the filter was to

use a 20 gallon black garbage bin with a hole cut into the bottom with a 4 in diameter PVC section with at pipe seal through it. The final fabricated components are shown in Figure 2.24 and Figure 2.25.

Figure 2.24: Fabricated mud tank and filter

Figure 2.25: Inside of sediment filter detailing the mesh over the filter to tank transfer tube

2.3. Vertical Drilling Rig Design

Another objective of the project was to design a second drilling rig to be used with an existing wellbore at Texas A&M University Riverside Campus. The design of this rig underwent various stages. The need was a simple free standing rig that could be used to support the topdrive, fluid swivel and BHA. Early on, it was determined that the best way to raise and lower the system was to use a cable winch system to lift from the top drive and to use the weight of the system as the WOB as seen in the concept sketch in Figure 2.26. A winch system was chosen due to the existence of a pneumatic winch at the Riverside derrick where the tests would be performed.

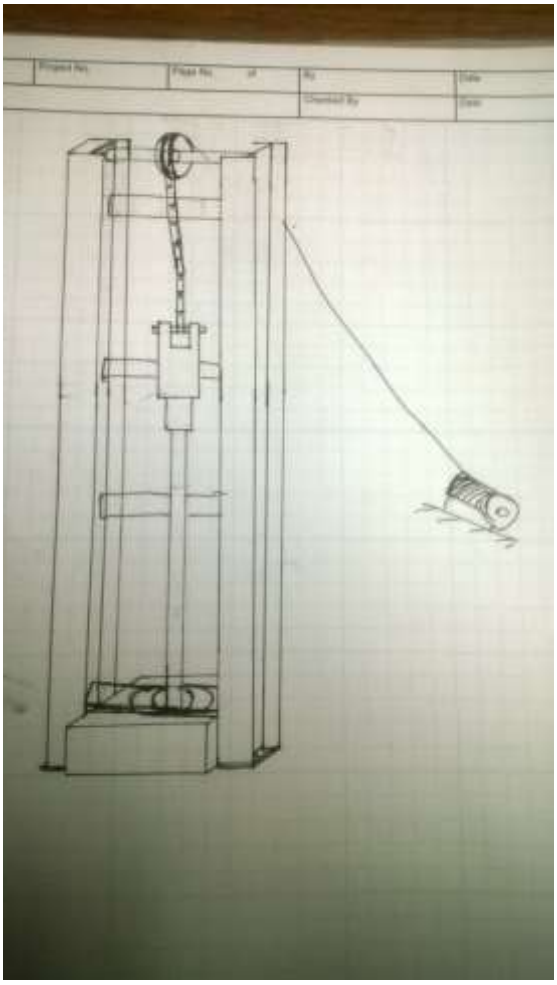

Figure 2.26: Initial Concept drawing of vertical test rig

This concept was developed assuming that the system would be driven by a hydraulic auger drive and using a standard water well drilling mud inlet swivel as the fluid inlet into the system. The hydraulic auger drive was chosen as a top drive due to availability, low cost, high torque and high thrust load capability. This method of driving the system was also included in the original project proposal to the Qatar National Research Fund (QNRF). An example of a hydraulic auger drive that would be used for this application can be seen in Figure 2.27.

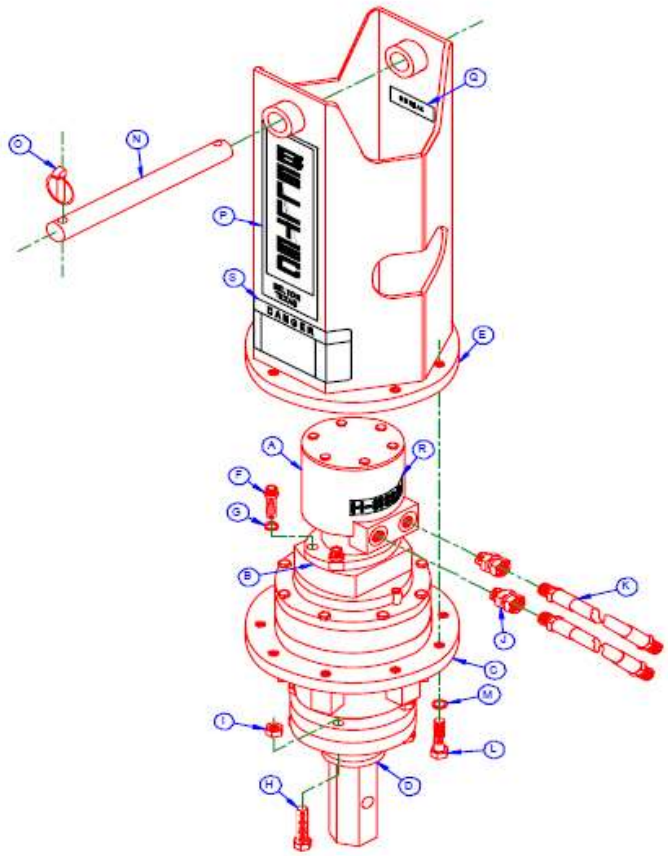

Figure 2.27: Detail and assembly instructions of a Belltec hydraulic auger drive

Once the drive and lift systems were established various concepts of the structure were developed. The three main concepts developed can be seen in Figure 2.28. These concepts were developed under the assumption that 10 ft sections of drill pipe would be used. The concept shown on the left was designed using I-beam as the main support structure. The top drive in this concept was directed on a track with rollers. The middle concept utilized four tubes as the track for the topdrive. These tubes were supported by an external support structure. The concept shown on the right is a simplified design of the four tube model. This concept would use larger tubing as the track for the top drive which would also act as the support structure. The third concept was eventually chosen

due to its lower material cost, ease of manufacturing and symmetric geometry. The symmetric geometry was desired because there would not a bending direction that had a substantially lower moment of inertia as is seen in the I-beam concept. The main issue foreseen with the tube concept was that at high enough loads it was prone to buckling and lower frequency resonance because of the long sections of relatively thin structural tubing.

Figure 2.28: Two stages of the development of the vertical drilling rig (Left: I-beam rail and support concept, Center: pipe rail with external support structure concept, Right: simple pipe rail concept)

The final concept shown in Figure 2.29 was eventually developed from the original simplified pipe concept but with the intention to use 5 ft pipe sections to reduce the overall height. This concept was chosen due to its low cost construction, high torsional strength and shorter size to lower the natural frequencies and improve the stability of the system. The shorter size of the rig also increases the safety and ease of tripping because of the reduced requirement for pipe length. This reduction makes the tripping process more safe and manageable by one or two people.

One key concept of the rig was providing a bending moment relief link above the top drive. The function of this link would be to add two lateral degrees of freedom in the system. Due to the high torque capacity of the auger drive, it was important to allow small lateral movements in the pipe so that any lateral vibration would not cause a large bending moment in the pipe and cause the pipe to fail due to combined bending and torsional stress.

Figure 2.29: Final concept of vertical drilling test rig

In order to provide the ability to add in additional sections of pipe as the drillstring is lowered, a slip plate will be used to slide onto a flat cut into the drill pipe sections as shown in Figure 2.30. This plate will hold the drillstring and BHA secure as the pipe is unscrewed from the drive system. The top drive will then be lifted up to the top position and a new pipe section will be threaded onto both the top drive assembly and the existing drillstring being held in place by the slip plate. Once the additional pipe section is added, the slip plate can be removed and drilling can continue for another 5 feet.

Figure 2.30: Slip plate for vertical drilling rig

The design of the horizontal rig also included the downhole measurement system. The downhole measurement system module is proposed to be a self-contained device that will have all of the sensors and the formation sample. The current concept assumes a formation sample exactly the same as that proposed for the bit force measurement rig discussed in Section 2. This device will be placed near the bottom of the well and drilled into. The current concept for this downhole measurement system can be seen in Figure 2.31. Figure 2.32 details the measurement system with the drill collar, to show how all three proximity probes will be used during drilling.

Figure 2.31: 3D CAD model of downhole measurement and sample containment device

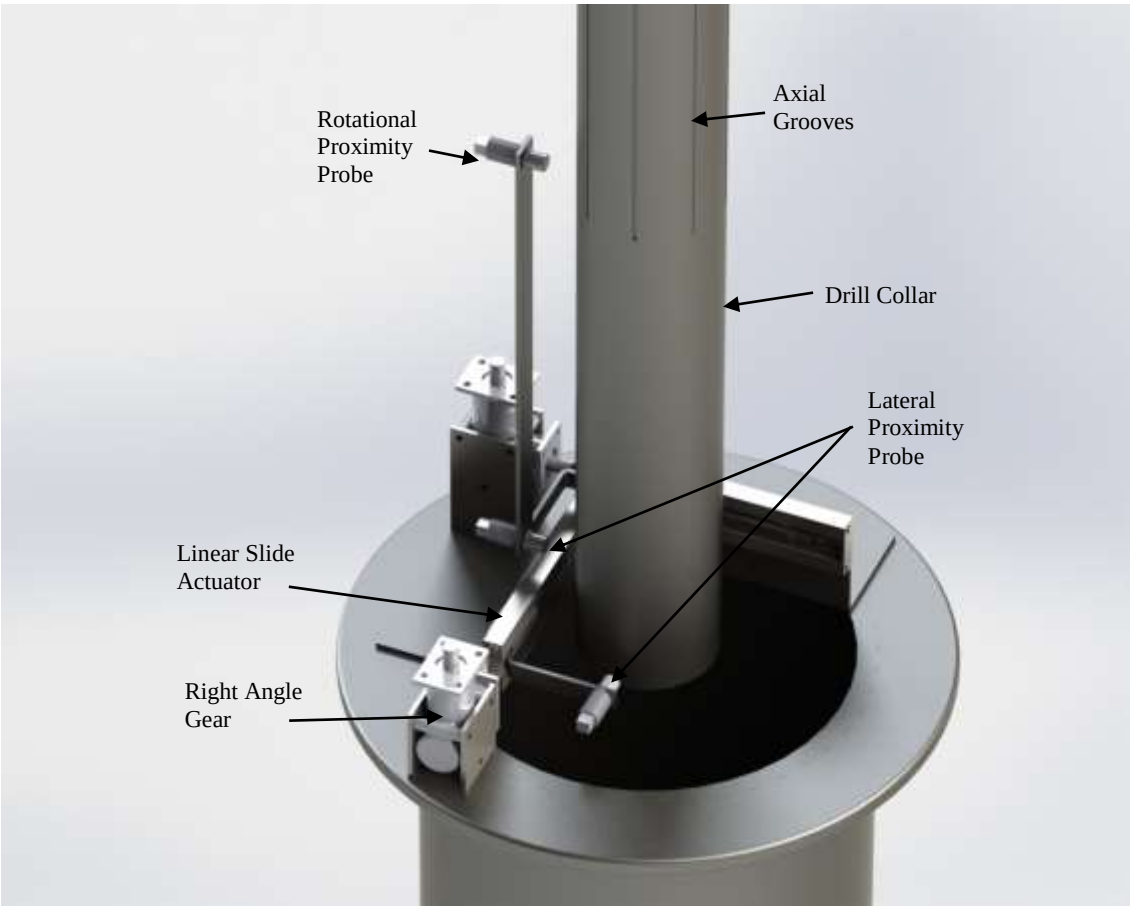

Figure 2.32: Detail of downhole sensor system 3D CAD Model

The downhole assembly will contain a sample containment cylinder with the build on sensor system at the top. The sensor system will consist of three proximity probes to measure the vibration in the drillstring. Two of these probes will be used to measure the lateral motions of the drillstring near the drilling interface. The third proximity probe will be located higher up on the BHA. This sensor will be used to measure the rotational speed and vibration on the drillstring. It is proposed that the drill collar that interfaces with the bit will have axial grooves extending over a short distance along the outer surface. This will be placed to coincide with the height of the sensor when drilling begins and will be the same length as the formation sample. These grooves will create

sudden increases in the distance measured by the probe making somewhat of a square periodic reading. Utilizing this reading, the peaks in amplitude can be counted by the data acquisition system (DAQ) and transformed into an angular velocity.

Due to the fact that it will be difficult to lower the drillstring perfectly down into the center of the sample containment device, and considering the clearance needed for the drill bit to pass by the sensors, it was important to add a feature that allows for the remote adjustment of the position of the sensors. To do this, linear slides were added to the assembly. These slides would be actuated by a rotational input, and as such, right angle gear boxes would be coupled to the slide position control knob. These right angle gear boxes would allow for a more convenient and easy to work with input since it would be facing upward instead of toward the casing wall of the existing well. These would then be turned either by a long rod device extending to the surface or using remote controlled downhole motors.

3. MEASUREMENT SYSTEM

3.1. Measurement System Design

The majority of the design of the measurement system was already completed before this work. Namely, the lateral load rods and the load cell discussed earlier. There were, however, a couple of sensors that needed to be addressed for the rig to be functional. In order to develop a transfer function between the lateral measurement rods and the lateral forces acting on the bit, the position of the sample carriage must be known. To gather this crucial data, it was determined that a string potentiometer would be used as seen in Figure 3.1. The best location for the device was located to be between the rear end of the sample carriage and the hydraulic cylinder support structure. This sensor was ideal for this application due to its long stroke and ease of use.

One consideration, however, was that the position of interest is the depth of penetration, not necessarily the distance of the sample carriage from the hydraulic cylinder support structure. This issue was easily resolved by measuring the dimensions of the rig and deriving a position transform equation. In order to make the depth of penetration zero at the end of the sample containment cylinder, the following equation was applied.

$$d = x - 28.77 + l_B \tag{3.1}$$

where x is that distance between the back of the sample containment carriage to the front of the hydraulic cylinder support, and l_b is the length of the drill bit. All of these dimensions are measured in inches.

Figure 3.1: String Potentiometer used to determine carriage location

The rig also needs to be able measure the relative displacement between the shaft and the formation sample for side load tests to determine the effective stiffness of the rock sample. While the previous final design of the rig included a proximity probe as the sensor to measure this deflection, the actual location and installation of the probe was not finalized. To ensure that the feature could be added in, the proposed location of the probe is to be placed in the sample cylinder cap near the end of the formation sample as shown in Figure 3.2. Since this cylinder cap, which is part of the mud drain assembly, can be easily removed and accessed, this was determined to be the ideal location to put the probe. It should be noted that probe would have to be backed out until the drill has penetrated into the sample enough so that only shaft is extending out of the cylinder. Otherwise, the sensor would be damaged by the rotating bit and need to be replaced. This sensor is not currently installed onto the drilling rig and should be added when considering testing the formation stiffness.

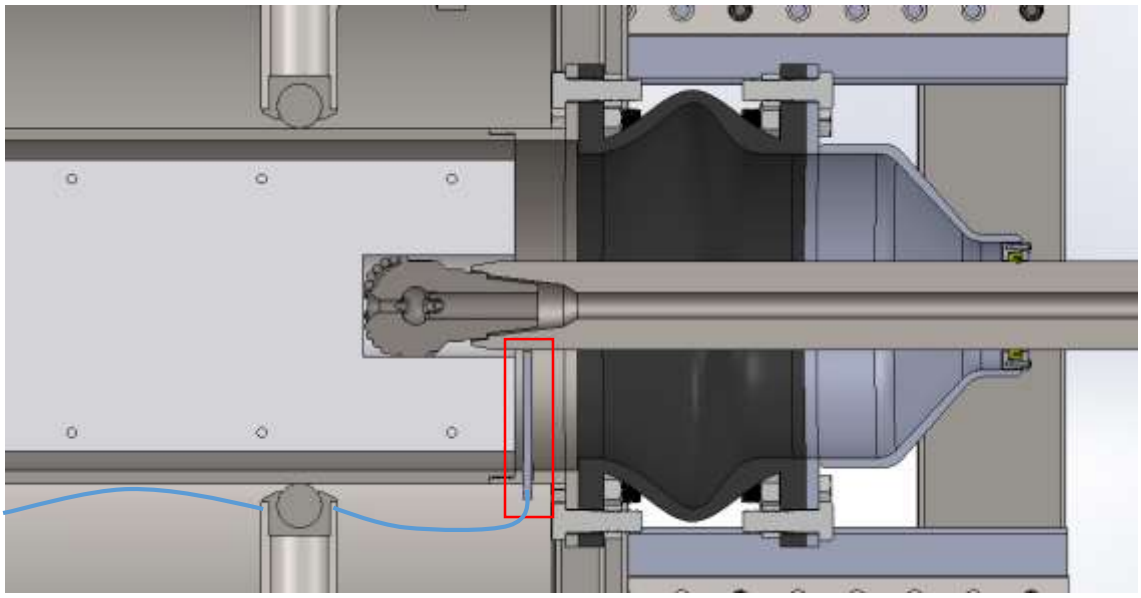

Figure 3.2: CAD model detailing location of side load proximity sensor

3.2. Sensor Calibration

A major part of the functionality of the test rig is ensuring that all sensors are reading consistently and accurately. This process of ensuring that all sensors are working correctly differed from sensor to sensor. The axial torsional load cell was factory calibrated and delivered with the calibration data. This data provided was validated doing a series of force and torque tests. These tests were not only used for verification purposes, but also to ensure the accuracy of the load cell while under relatively low loads compared to the full load capacity of the sensor. The lowest data point provided by the factory calibration was 30000 lbf. It should be noted that this load cell was purchased before the rig was redesigned for the lower power requirements. Due to this, it was imperative that the load cell worked accurately below 30000 lbf since the current capacity of the rig cannot exceed 30000 lbf. The same issues existed with the torsional rating as well. It was verified that even at very low forces, the load cell was very linear and accurate. The load cell was rated to have a 0.027% error in its readings.

3.2.1. Lateral Force Load Rod Calibration

While the load cell only needed to be verified, the lateral force measurement rods discussed in the previous section were designed and fabricated for the rig and the rods needed to be calibrated and tested to obtain a strain to force conversion factor for the rod measurements and to understand the accuracy of the rods. The calibration of these rods underwent various stages. For a proper calibration, there was a need to shunt calibrate each Wheatstone bridge on the rods and to calibrate the rods themselves.

It is important to acquire a shunt calibration factor for each bridge to get all of the rods to read loads similarly. It was also crucial that all axial gauges read similarly since the system would output the average reading of both axial gauges to suppress any bending moments on the rods. This was done by putting a known resistor across the strain gauge being calibrated. This resistor simulates a known strain in the strain gauge. A shunt calibration factor is developed to make all of the bridges read the voltage output from the resistor as the same value, which is the actual strain of the load rod.

During the calibration process, it was discovered that the measurement rods were very sensitive to fluctuations in temperature. This is due to the thick walled design of the tubes. After this discovery, it was approximated that a change of temperature of $1^{\circ}F$ produces a strain equivalent to an axial load of about 900 lbf. This is partially due to the high coefficient of thermal expansion found for the 304 stainless steel material used for the rods. However, it should be noted that this translation would be assuming that the entire thickness of the tube has increased in temperature the same amount which takes time. Nevertheless, there is need to be cautious about the temperature error. In order to calibrate the rods efficiently without the effects of temperature producing poor data, the tests were done quickly and the air conditioning was monitored so that there was very little or no temperature change. This approach produced much more consistent results than some of the initial calibration tests. Once installed into the rig the measurements of the lateral load rods that are exactly opposite of each other are averaged which would

greatly reduce the thermal effects, assuming that the temperature fluctuation at each rod is the same or very close.

However, there was still a concern that the drilling process would produce high temperatures that would affect the measurements of the rods. This led to the need to ensure that large temperature changes were not produced during a drilling test. For simplicity, a very conservative approach was undertaken as a quick check for frictional heat generation and temperature distribution to represent a worst case scenario. For this case, the frictional heat generation was assumed to be

$$Q = \eta T_f \Omega \tag{3.1}$$

where Q is the heat generation, T_f is the frictional torque, η is a heat power transformation factor, and Ω is the rotating speed of the shaft. Being conservative, the calculation was done assuming that all frictional power is converted to heat so that η goes to 1. Utilizing the adjustable parameters of the rig and assuming a cylindrical bit with uniform pressure on the formation, Equation 3.1 becomes

$$Q = \left(F_L r_b + \frac{2}{3} F_A r_b \right) \Omega \tag{3.2}$$

where F_L is the lateral load on the bit, F_A is the weight on bit, and R_b is the radius of the bit. Using the maximum capacity of the drilling rig for the heat generation parameters, F_A becomes 20,000 lbf, F_L is 3000 lbf, Ω is at the maximum speed of 115 RPM or 12 rad/s. Using these values, a finite element model was created to determine the temperature change in the system. The finite element model assumed a formation sample made of granite which has a high thermal conduction constant which would result in a faster system heat up time. The setup of the finite element model is shown in Figure 3.3. The model was further simplified to only have one lateral load rod and to be an insulated system. The formation sample, the metal sample containment cylinder, the lateral load rod and the surrounding air were all taken into account for the analysis.

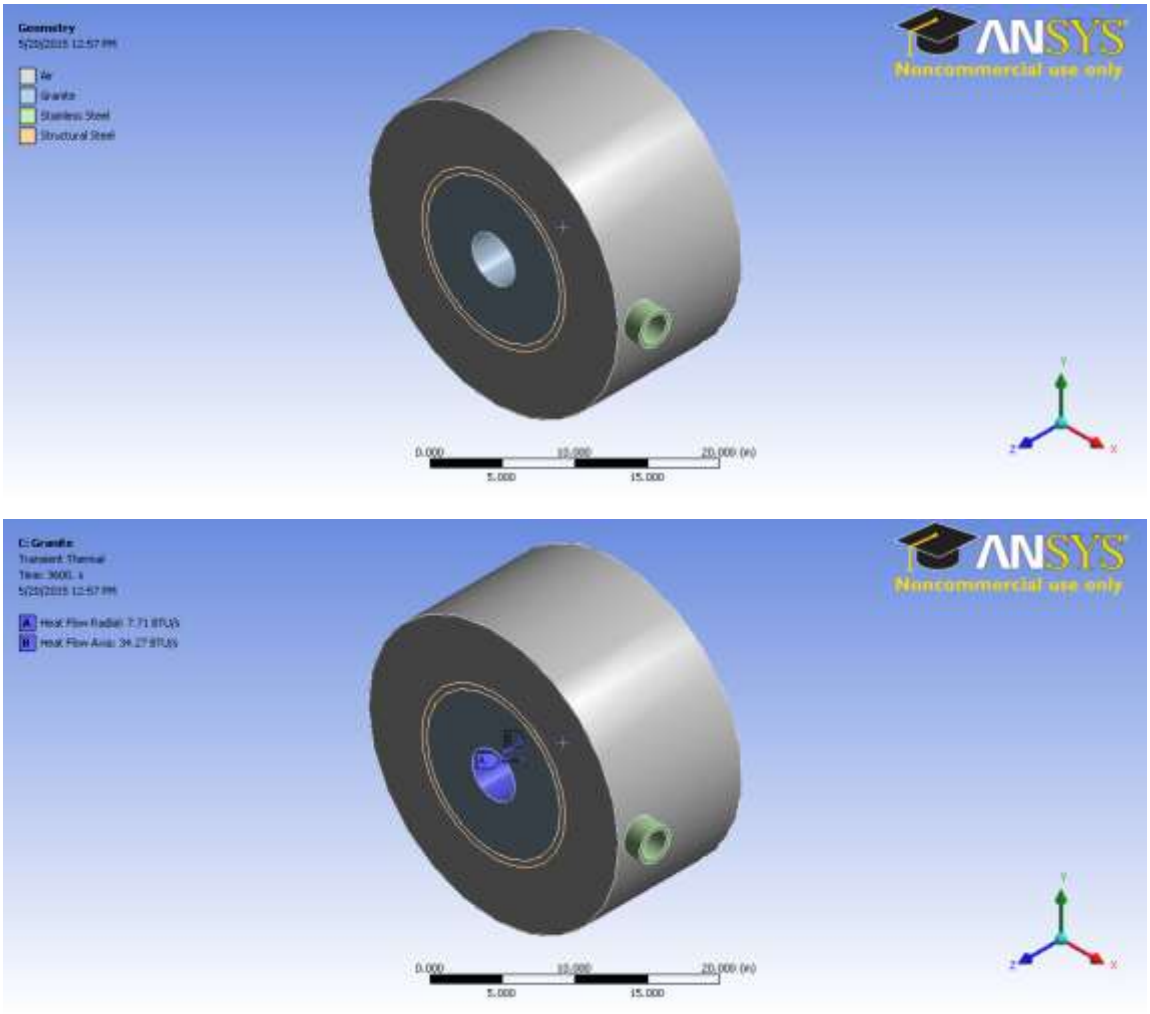

Figure 3.3: Finite element model set up in ANSYS® Workbench

The results of the temperature of the rod and the surrounding air are shown in Figure 3.4. These results show that under these highly conservative results one would have 5 minutes of constant drilling before the rod would even begin to noticeably change temperature. After 10 minutes of these extreme loading conditions, the highest temperature increase on the rod would be 1°F. This temperature change would be near the tip as shown in Figure 3.5 and thus the material below the strain gauges would not be

experiencing as much thermal strain and not affect the strain gauge reading enough to be a concern.

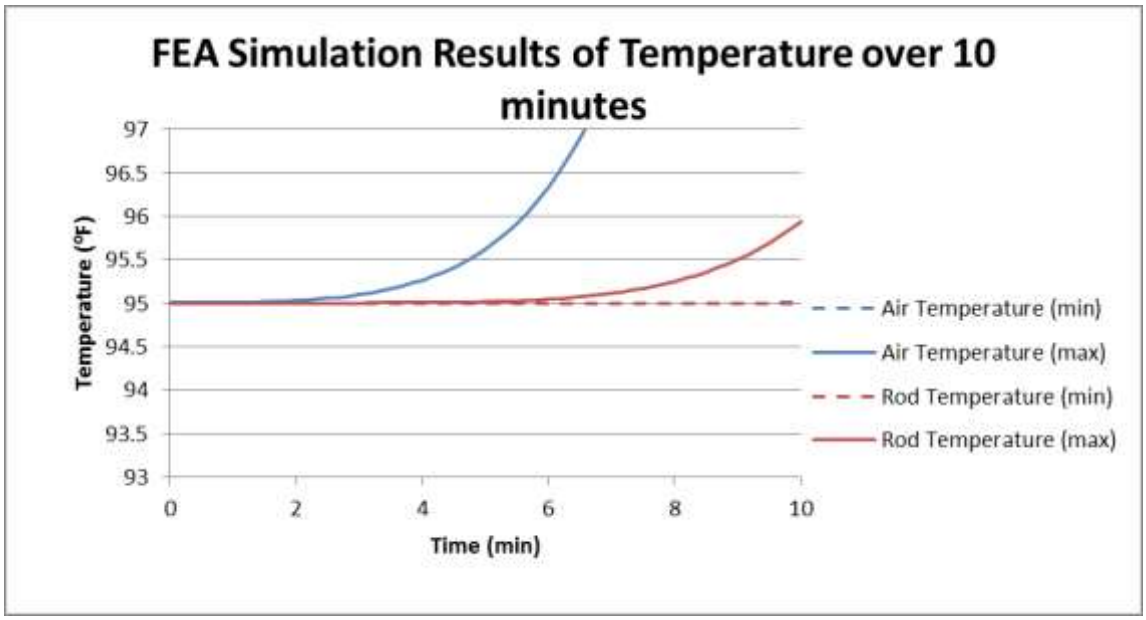

Figure 3.4: Temperature envelope of lateral load rod and surrounding air while drilling for 30 minutes

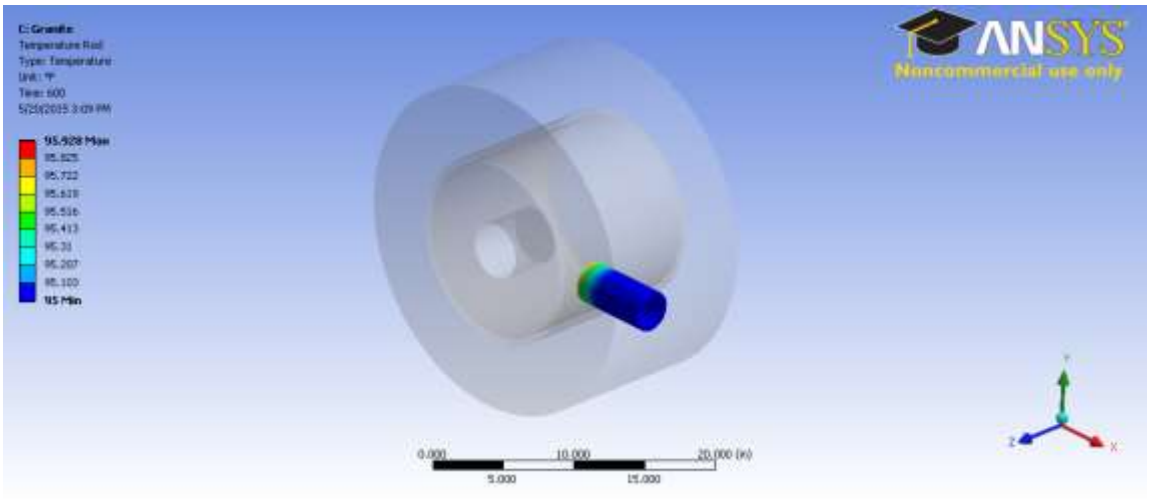

Figure 3.5: The temperature distribution on the lateral load rod after 10 minutes of simulation

The axial calibration data for all 8 load rods can be seen in Figure 3.6 through Figure 3.13. By examining the calibration data, it can be seen that there is little to no X and Y bending reactions to an axial load. It is assumed that any correlation found is due misaligned axial loading causing a slight bending moment during testing. Although the temperature effects were minimal in the calibration testing, the rods were found to be accurate to about ±100 lbf on average. Assuming that the full scale (FS) expected force is 2000 lbf per rod, this translates to an average error of ±5% FS. Figure 3.14 shows the deviation plot of rod 1 which was the used to determine the deviation error of the data sets. The plot was created by subtracting the data point values from the linear calibration fit value at the same load. This data shows that there is a need to redesign the sensor or to add noise cancelling features to make the rods more accurate. Also, if it is acceptable to read data at a lower frequency, longer averages could be made that increase the accuracy of the rod.

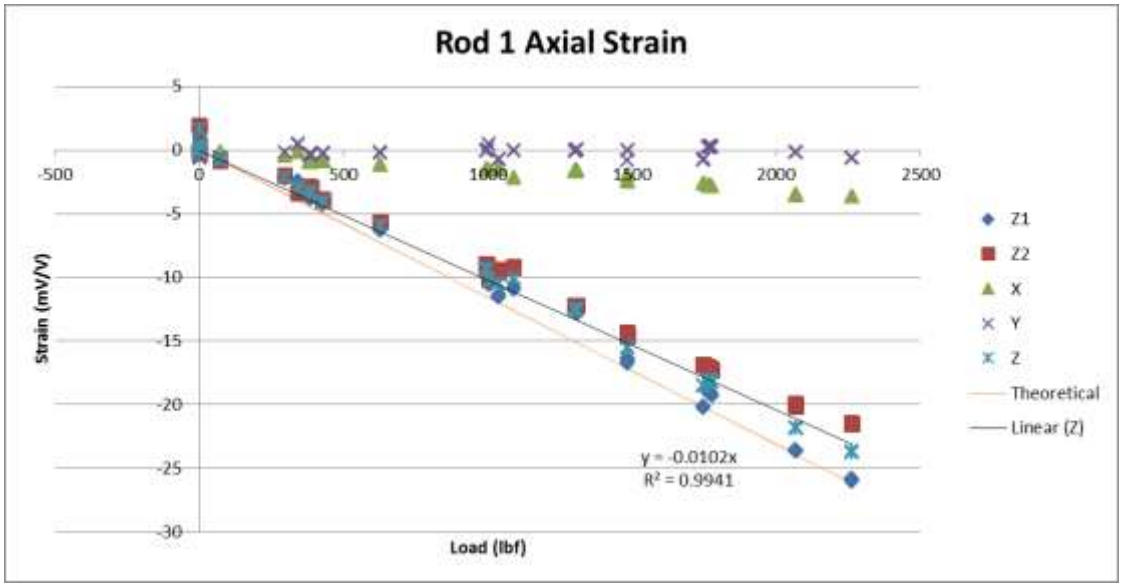

Figure 3.6: Axial load calibration data of Rod 1 showing the linear fit of the data

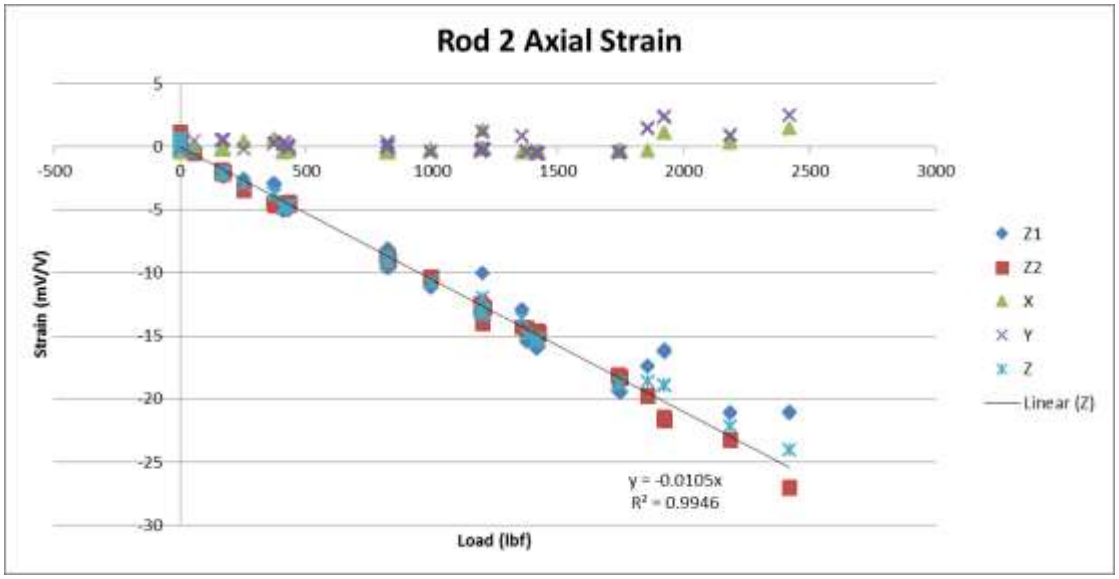

Figure 3.7: Axial load calibration data of Rod 2 showing the linear fit of the data

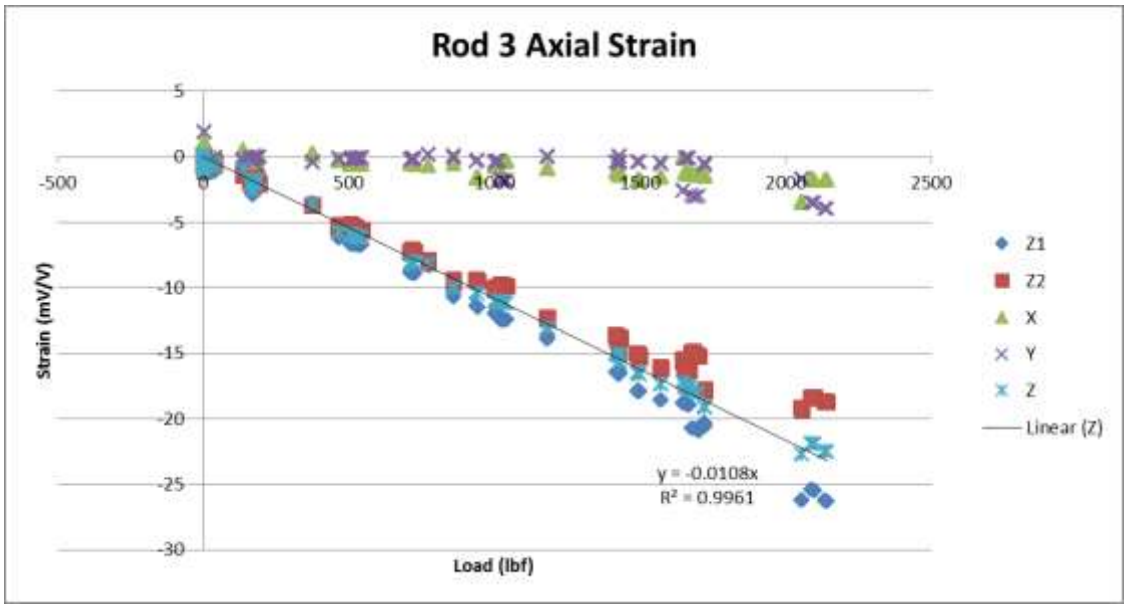

Figure 3.8: Axial load calibration data of Rod 3 showing the linear fit of the data

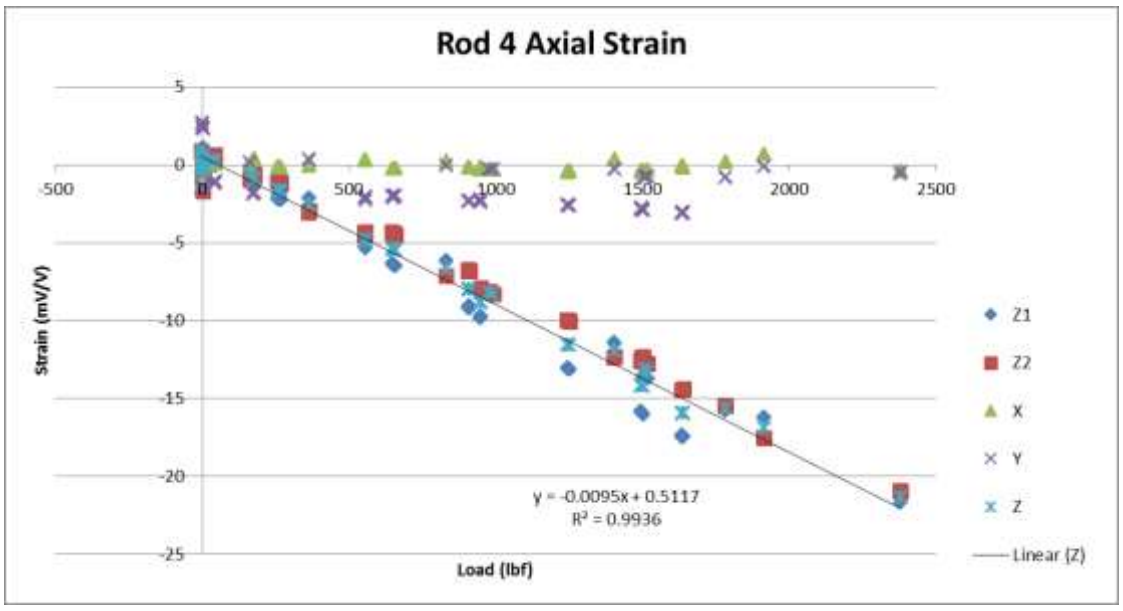

Figure 3.9: Axial load calibration data of Rod 4 showing the linear fit of the data

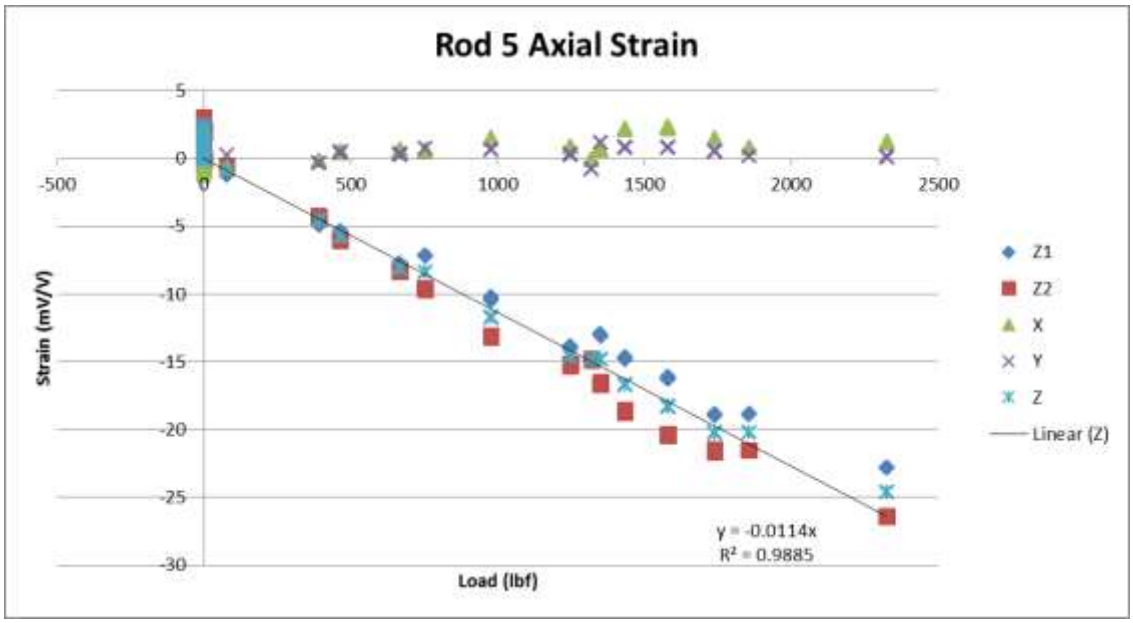

Figure 3.10: Axial load calibration data of Rod 5 showing the linear fit of the data

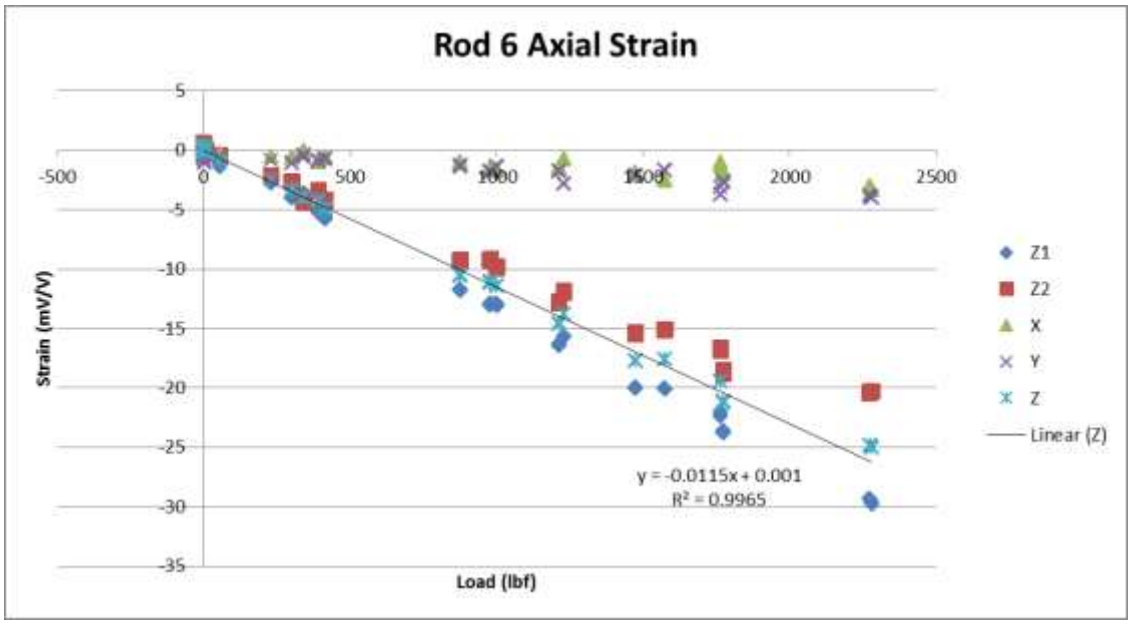

Figure 3.11: Axial load calibration data of Rod 6 showing the linear fit of the data

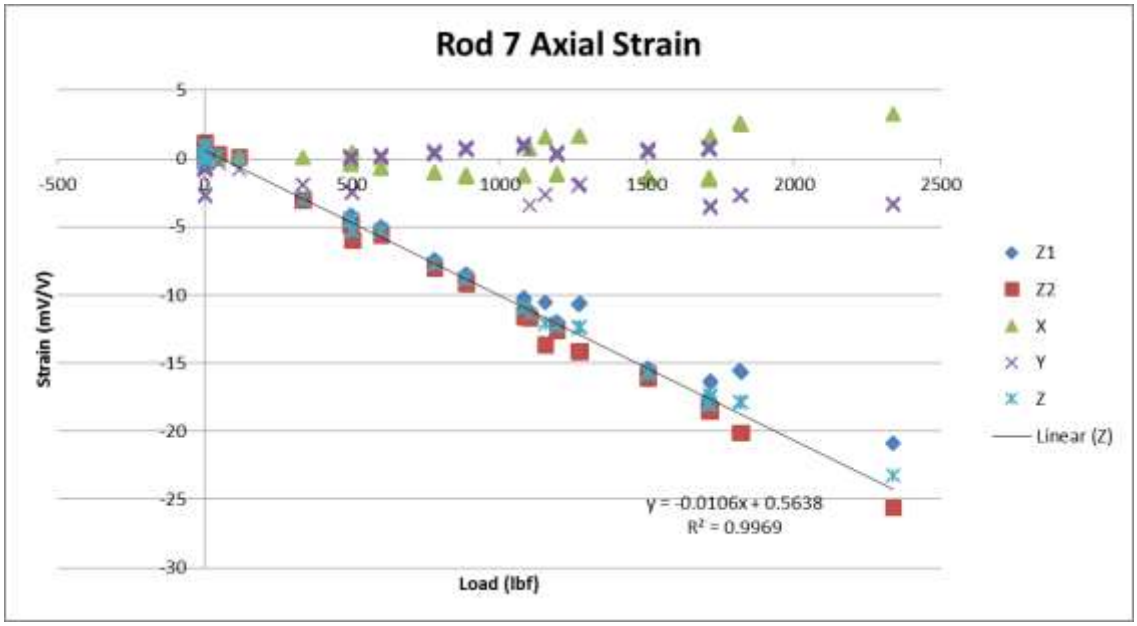

Figure 3.12: Axial load calibration data of Rod 7 showing the linear fit of the data

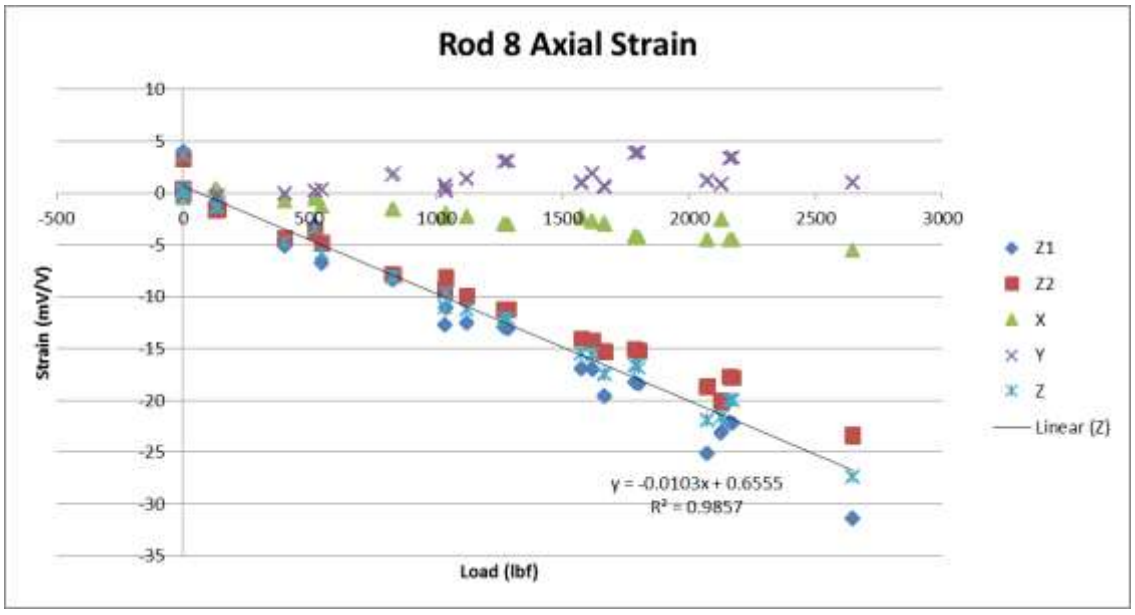

Figure 3.13: Axial load calibration data of Rod 8 showing the linear fit of the data

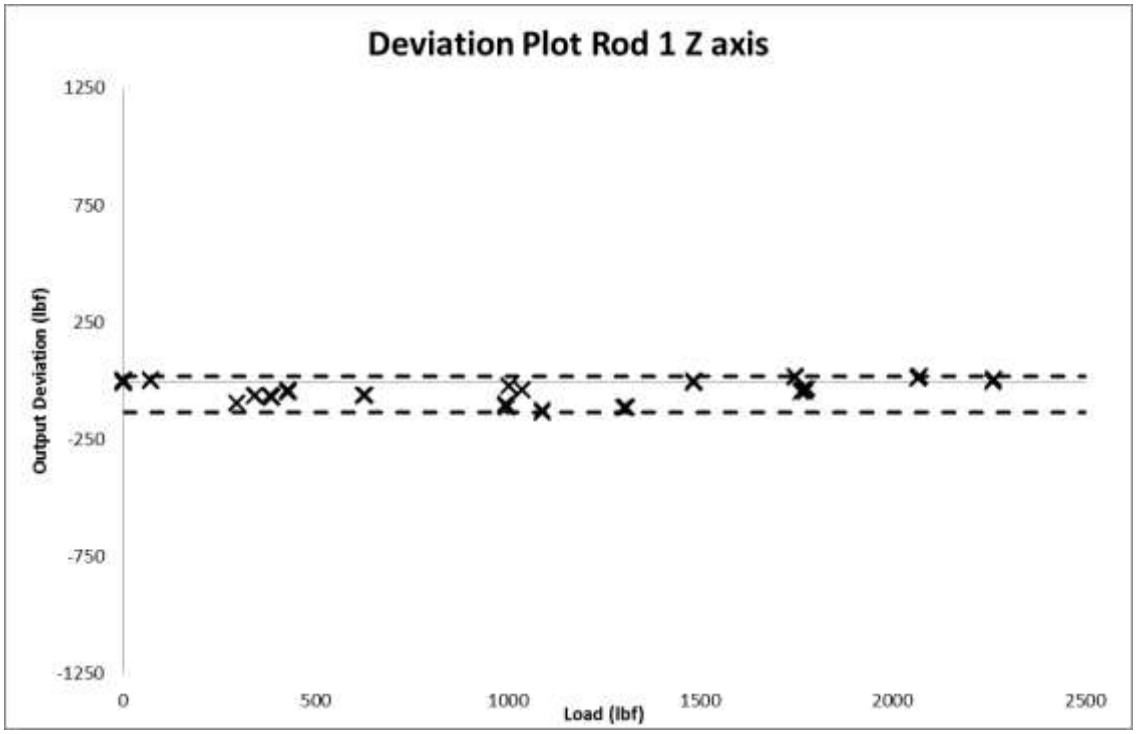

Figure 3.14: Deviation plot of the axial data of rod 1

To account for any frictional loads caused by the lateral force rods, the strain gauges along the local lateral axes were calibrated as well. The process for calibrating these rods was similar to the axial load rods. The rod was set up and loaded as a cantilever beam. This was done twice for each test, one where the load was oriented along the local X axis and the other oriented along the local Y axis in order to calibrate each bridge. The calibration data for these gauges are found in Figure 3.15 through Figure 3.22. The side load gauges were found to be more accurate than the axial gauges. This makes sense due to the larger stress due to bending than a pure axial load. The full scale side load for this system is assumed to be a maximum of 500 lbf. With this, all of the bending tests resulted in an accuracy of about 3% FS. This correlates to a value of 15 lbf deviation. An

example of one of the deviation plots for the bending tests is shown in Figure 3.23. The calibration factors for all rods and how they compare with each other can be found in

Table 3.1.

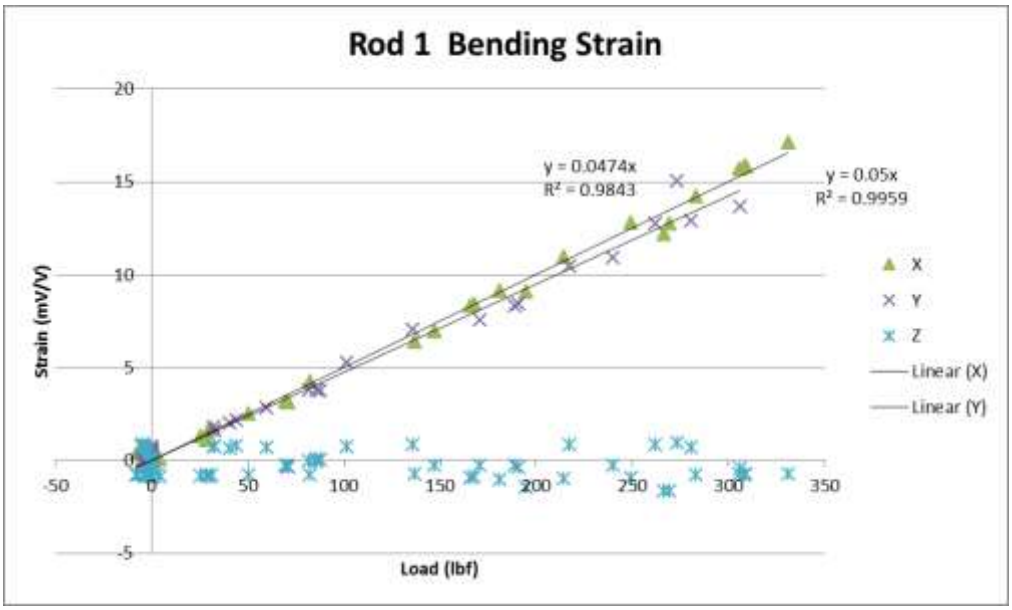

Figure 3.15: Lateral load calibration data of Rod 1 showing the linear fit of the data

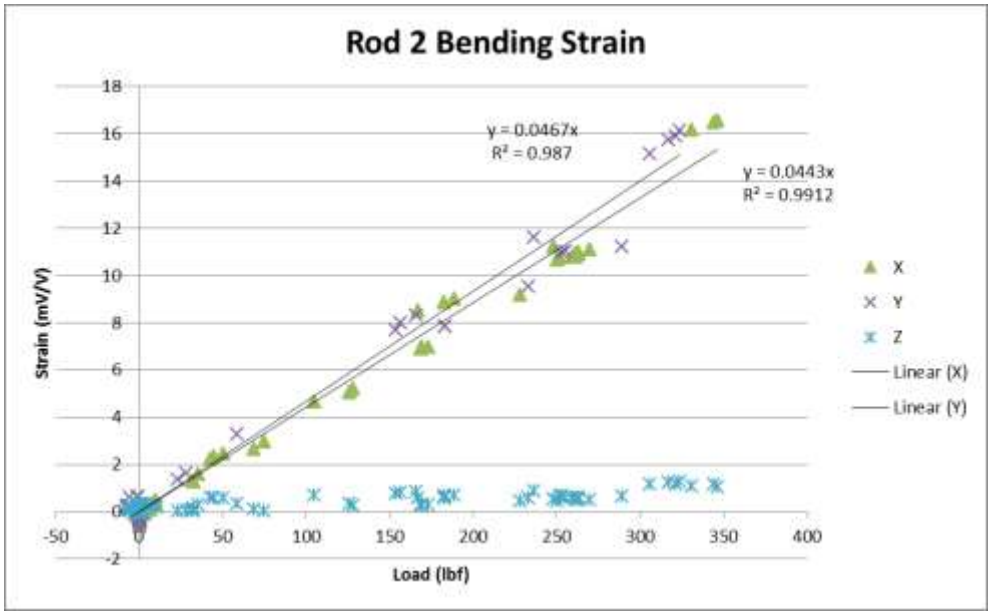

Figure 3.16: Lateral load calibration data of Rod 2 showing the linear fit of the data

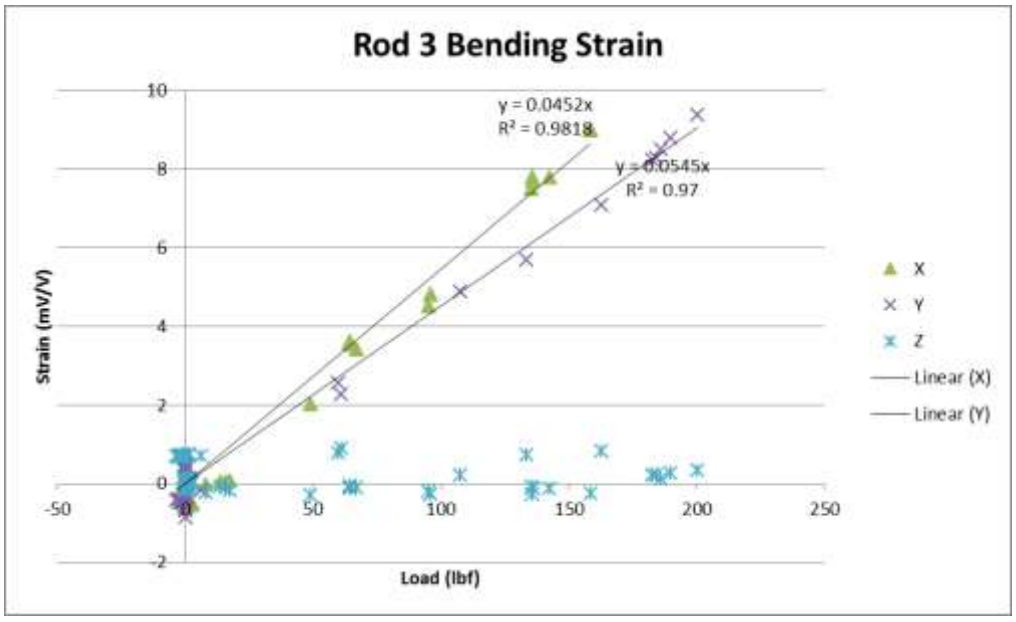

Figure 3.17: Lateral load calibration data of Rod 3 showing the linear fit of the data

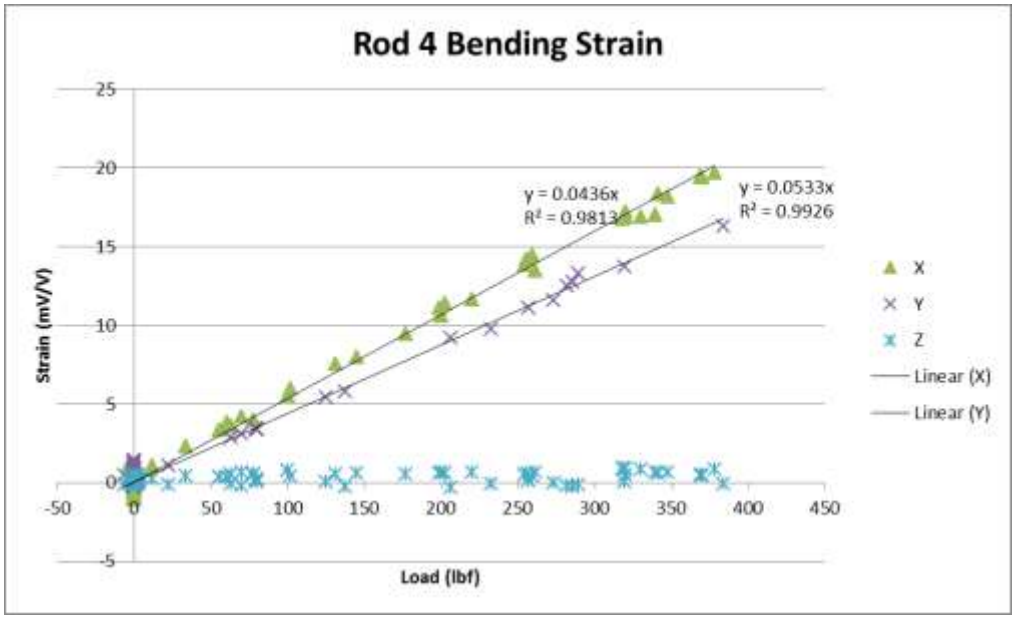

Figure 3.18: Lateral load calibration data of Rod 4 showing the linear fit of the data

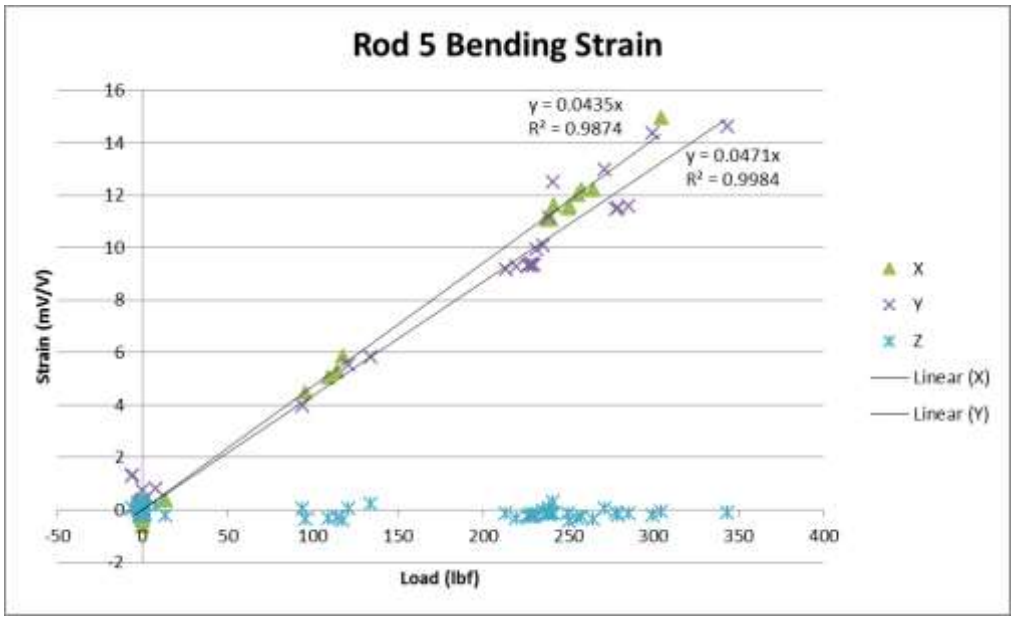

Figure 3.19: Lateral load calibration data of Rod 5 showing the linear fit of the data

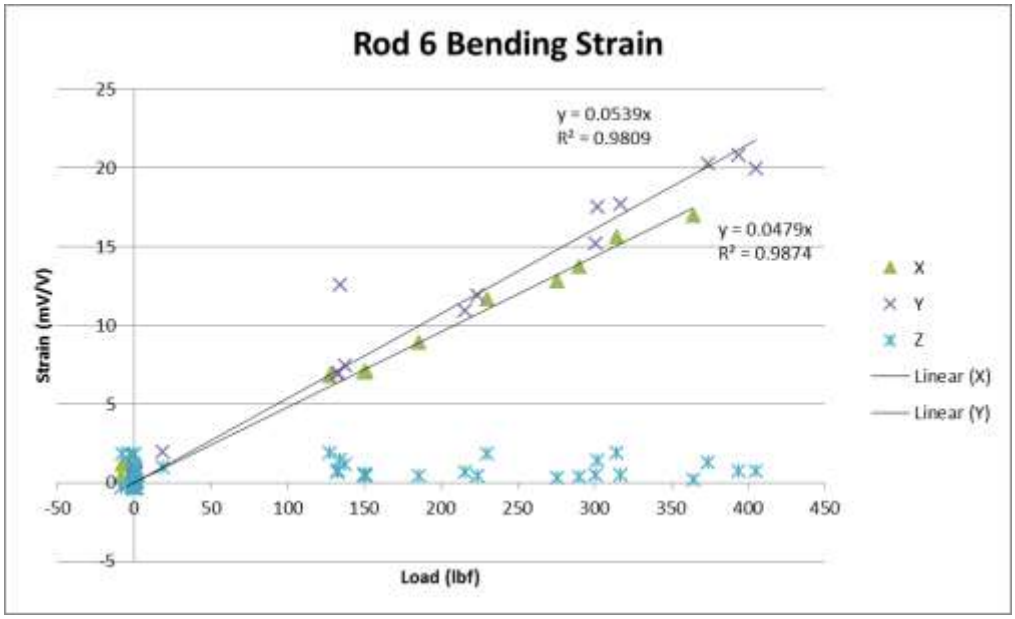

Figure 3.20: Lateral load calibration data of Rod 6 showing the linear fit of the data

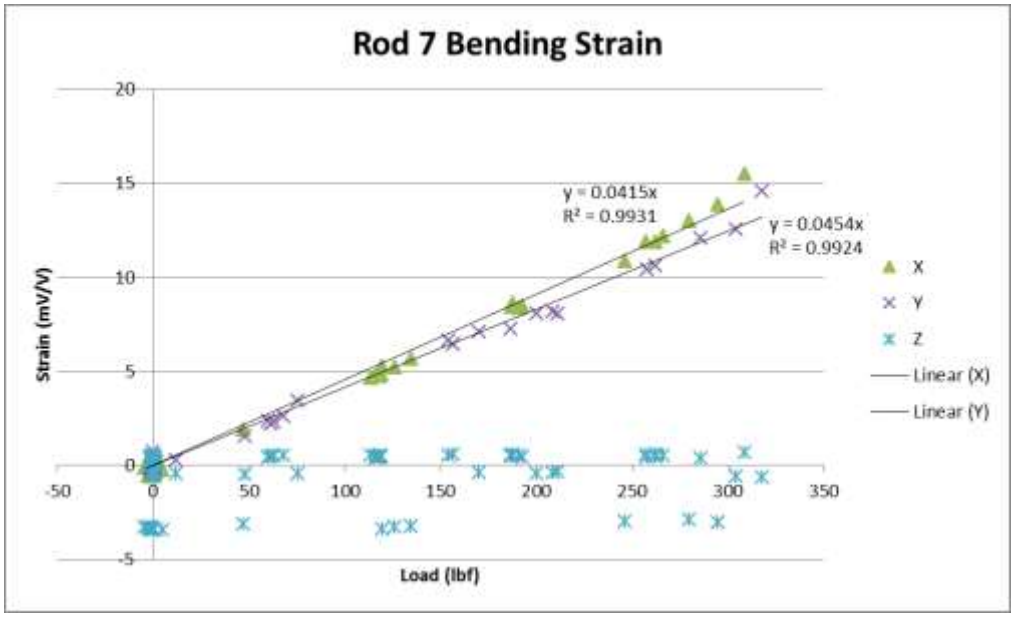

Figure 3.21: Lateral load calibration data of Rod 7 showing the linear fit of the data

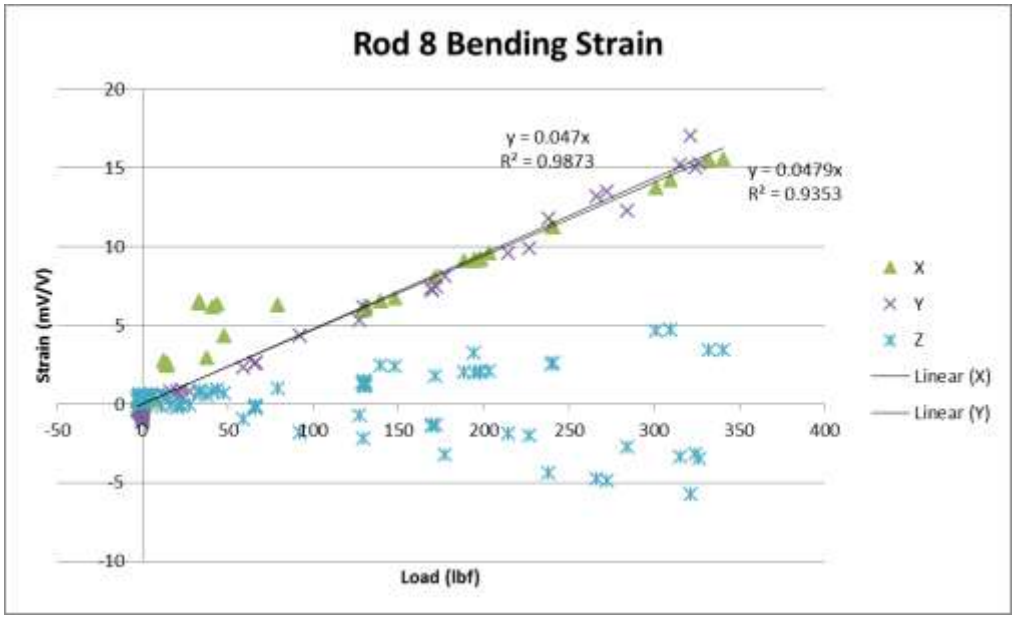

Figure 3.22: Lateral load calibration data of Rod 8 showing the linear fit of the data

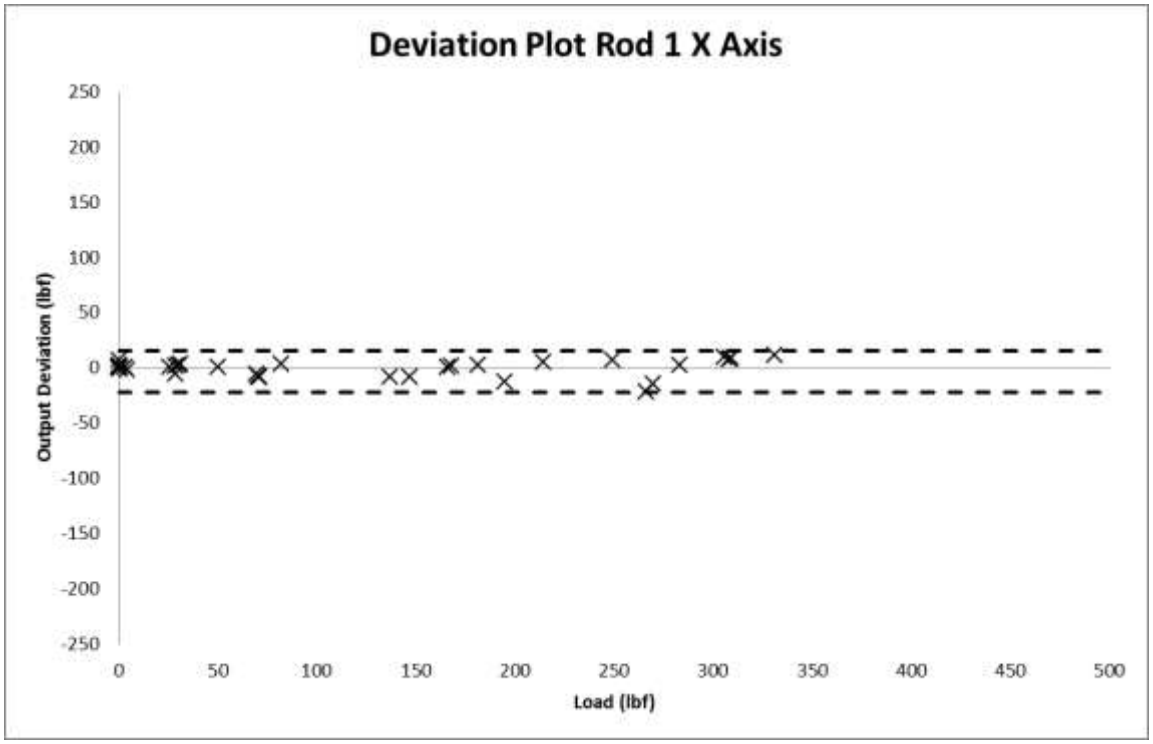

Figure 3.23: Deviation plot of the x axis data of rod 1

Table 3.1 also shows the summary of the rod output error. As seen from the table, the average error on the axial measurement of the rods was around 5% of the full scale output (FS), which is assumed to be 2000 lbf for the axial load. The worst error found for a specific rod was almost 8% FS. The error from the side load tests was generally lower with an average of about 3% FS. The highest error for the side load tests was 5.5% FS. The full scale side load is assumed to be 500 lbf.

Table 3.1: Force conversion factor, percent error from average and measurement error for each lateral load rod

	Calibration Factor (lbf/μStrain)	% error from average	Test Deviation (lbf)		Error range (lbf)	% FS Deviation
Rod 1			Max	Min		
z	97.96977376	1.9%	73.671	-111.18	184.851	4.6%
x	20.00840031	5.8%	15.59	-21.86	37.45	3.7%
y	21.0964418	0.6%	13.05	-17.23	30.28	3.0%
Rod 2						
z	95.21289772	1.0%	77.286	-136.33	213.616	5.3%
x	22.57928502	6.3%	35.26	-19.87	55.13	5.5%
y	21.3964281	0.8%	22.51	-29.09	51.6	5.2%
Rod 3						
z	92.4137856	3.9%	64.766	-73.86	138.626	3.5%
x	18.34815411	13.6%	7.21	-15.92	23.13	2.3%
y	22.11179672	4.1%	7.38	-10.5	17.88	1.8%
Rod 4						
z	110.1524034	14.5%	45.966	-108.63	154.596	3.9%
x	18.7680167	11.6%	12.77	-18.94	31.71	3.2%
y	22.9180804	7.9%	18.05	-10.27	28.32	2.8%
Rod 5						
z	88.02573593	8.5%	59.939	-161.44	221.379	5.5%
x	21.21578806	0.1%	13.13	-5.29	18.42	1.8%
y	22.99988455	8.3%	31.02	-18.35	49.37	4.9%
Rod 6						
z	86.90265889	9.6%	67.609	-116.1	183.709	4.6%
x	20.86827974	1.7%	15.83	-10.14	25.97	2.6%
y	18.57004744	12.5%	24.58	-18.04	42.62	4.3%
Rod 7						
z	98.10590635	2.0%	57.53	-77.447	134.977	3.4%
x	22.01215621	3.7%	10.62	-13.44	24.06	2.4%
y	24.10626219	13.5%	8.5	-16.25	24.75	2.5%
Rod 8						
z	100.5929386	4.6%	133.389	-184.43	317.819	7.9%
x	21.43422788	1.0%	5.21	-14.92	20.13	2.0%
y	21.27755224	0.2%	15.57	-22.63	38.2	3.8%

3.2.2. Lateral Force Load Rod Recommendations

Based on the calibration data, it was found that although the sensor error for the lateral load rods had a maximum value of 8% FS, this could cause some accuracy issues during tests. It is expected that a lot of the lateral loads experienced by the system will be at the same magnitude as the error bands and not necessarily near full scale load. This poses a problem for determining error from force data. This large error is in part due to the

design of the rods themselves. The rods are not sensitive enough to the expected loads, so to compensate for this lack of sensitivity a very large strain to force conversion factor to the raw data must be used. Not only does this large factor translate the small amounts of strain into the measured load so that the data makes sense, this very stiff system also takes small errors in the measurement system, whether it is from random error in the electronics, truncation error, sensor cross talk or thermal error and scales it to a large number as well. Strain gauges are better suited for thinner walled structures or, as seen in the calibration data, bending purposes which still improves with a lower moment of area. This is because of the higher strain associated with these applications. The axial loading of these thick walled cylinders does not produce a large enough strain to make the rods accurate.

The rated yield strength of the 304 stainless steel material that the rods are fabricated from is 75000 PSI. In order to fail this rod axially it would theoretically require a load of approximately 230000 lbf, in bending it would require a frictional load of approximately 26000 lbf. These values are far above any forces expected to be seen on the test rig. This gives a lot of room for area reduction to attempt to increase the sensitivity of the system. It is recommended that the rods are redesigned with a thinner wall to allow for more strain for a given load, thus lowering the error by lowering the strain to force conversion factors. If the inner wall under the strain gauges were to be bored out and reduced to a thickness of 0.1 in, this would produce a much more sensitive system while maintaining strength under the expected loads. Theoretically, this would reduce error and thermal effects by 70.5% for the axial loads and 64.7% for the side loads. Analytically, with this reduced wall thickness, the rods would still be capable of withstanding a local axial force of up to 68000 lbf and a 9200 lbf side load. These maximum loads were verified using finite element software. A finite element analysis was also done under full load conditions, as seen in Figure 3.24 and Figure 3.25.

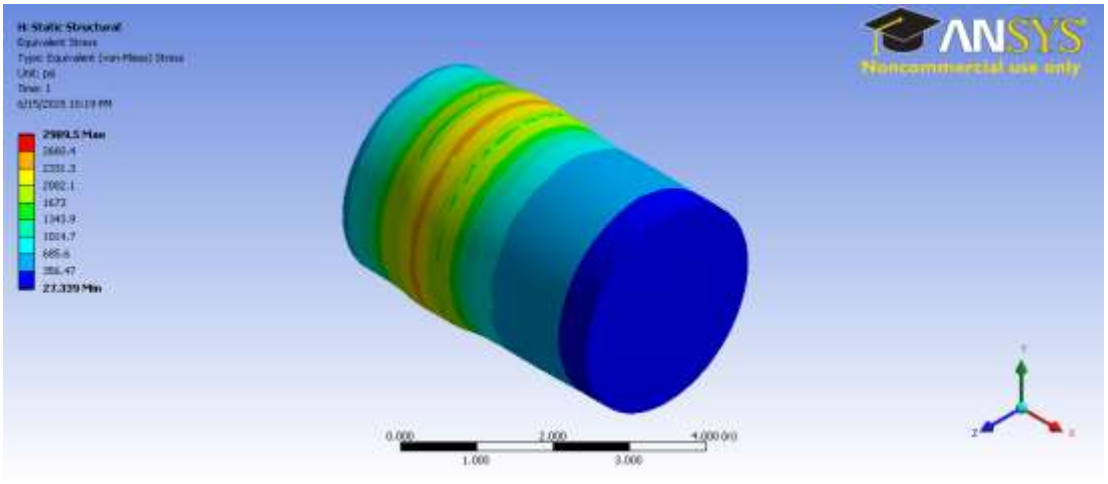

Figure 3.24: ANSYS® finite element analysis with 2000 lbf axial load on redesigned rod concept

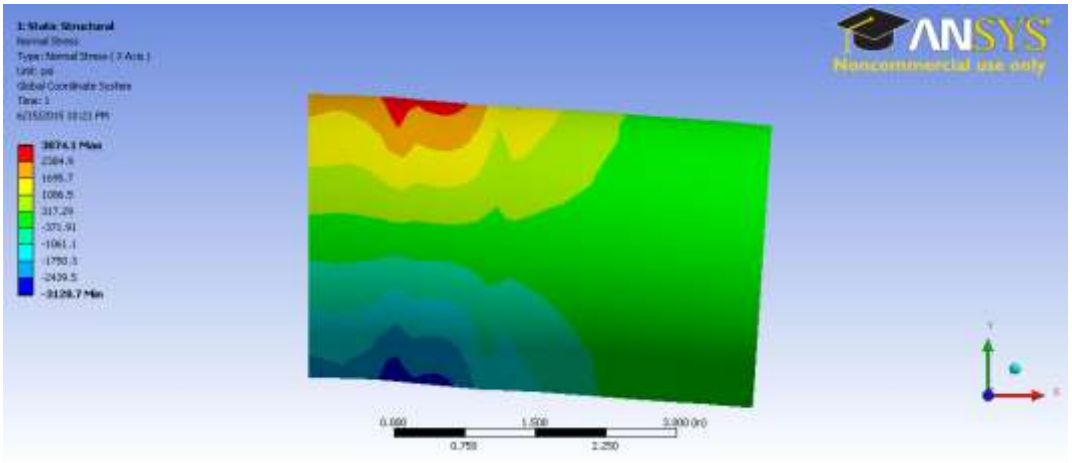

Figure 3.25: ANSYS® finite element analysis with 500 lbf lateral tip load on redesigned rod concept

Another important consideration would be if the rods failed due to buckling before exceeding the yield strength of the material. To check this, an analysis was done for both an axial buckling mode and a bending buckling mode. The results are shown in Figure 3.26 and Figure 3.27. These results showed that the critical buckling load for the axial

load would be 1.44×10^6 lbf and the critical transverse load would be 336500 lbf. These results are far above any forces that would be expected on the rig. Due to the analysis showing that the rods would perform better with a 0.1 inch wall thickness and that they would be capable of supporting the loads expected on the rig, it is recommended that a modification such as this be undertaken.

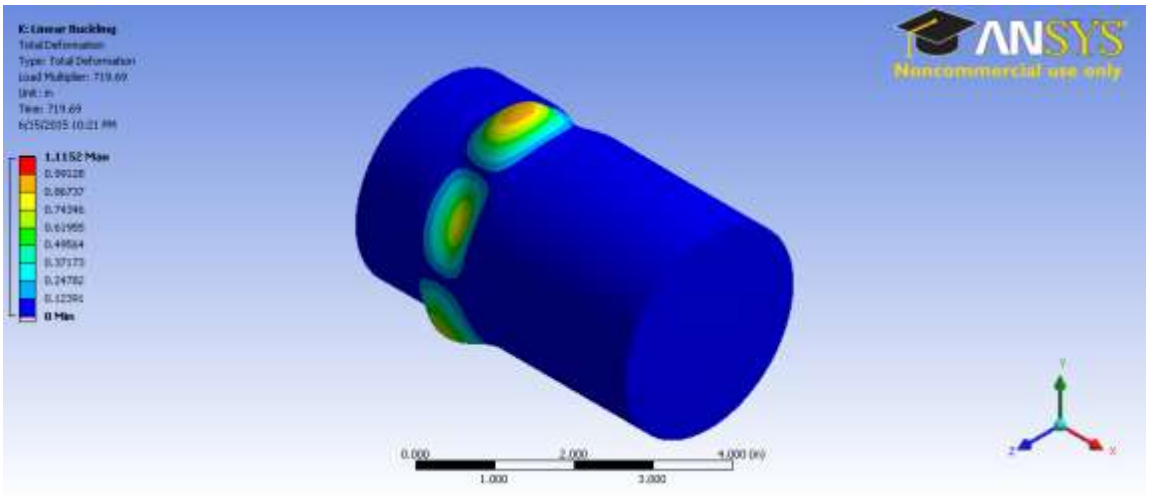

Figure 3.26: ANSYS® finite element analysis of buckling mode due to axial force

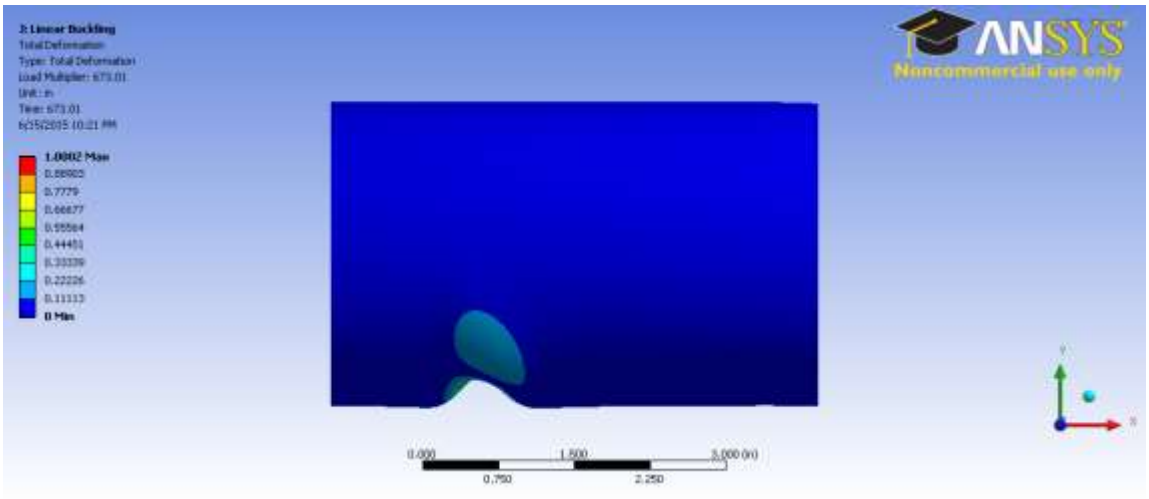

Figure 3.27: ANSYS® finite element analysis of buckling mode due to lateral tip load

As a recommendation as to how this modification could be made, it is suggested that the current load rods are cut about an inch below the strain gauges. The strain gauged end would be bored out to the desired wall thickness to a depth of about 1.5 inches. The other part of the rod, which is the mounting portion would have a thickness reduction from the outside at a depth of the wall thickness. This would create a rejoining spot for the two points which could be fixed with screws. This redesign would provide a simple method to make the desired modifications while keeping the thin walled section only under the strain gauges and not reducing the thickness over the entire rod. A computer model of the proposed change can be seen in Figure 3.28

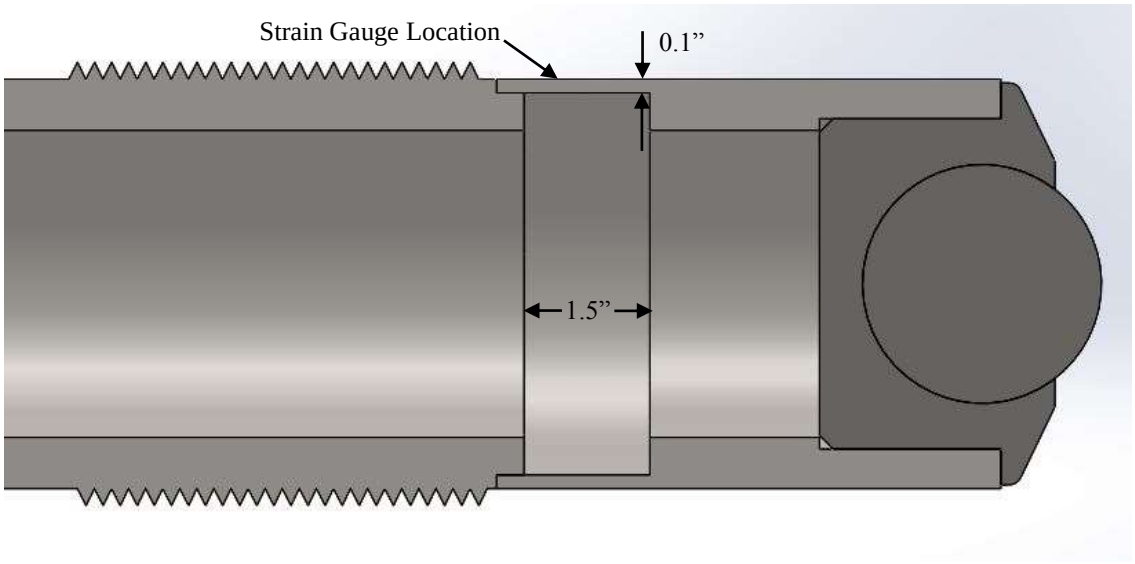

Figure 3.28: 3D CAD model of recommended lateral load rod redesign

3.3. Bit Force Data Acquisition Program Development

Due to its ease of use and highly customizable user interface options, National Instruments LabVIEW was used to develop the data acquisition code. The hardware used was a NI cDAQ-9178, 8 module chassis. Within the chassis, two 8-channel quarter-bridge strain modules, four 2-channel half/full bridge modules, and 1 4-channel voltage module were used to collect the data. In LabVIEW, there are two sections to any code, which is referred to as the VI. The first portion is the called the front panel, this is the user interface of the program. It contains all the buttons, controls and displays that make it possible to use the program as intended. The second part is the actual code of the program, it is known as the block diagram. The LabVIEW code is developed using an array of blocks and connectors to process and direct the data. For the drilling test rig, the LabVIEW VI was initially created by the Civil Engineering High Bay Lab at Texas A&M University. The front panel, or user interface of the LabVIEW VI can be seen in Figure 3.29. This program was very important in calibrating the rods because of its use in recording data and ease in shunt calibrating the strain gauge configurations.

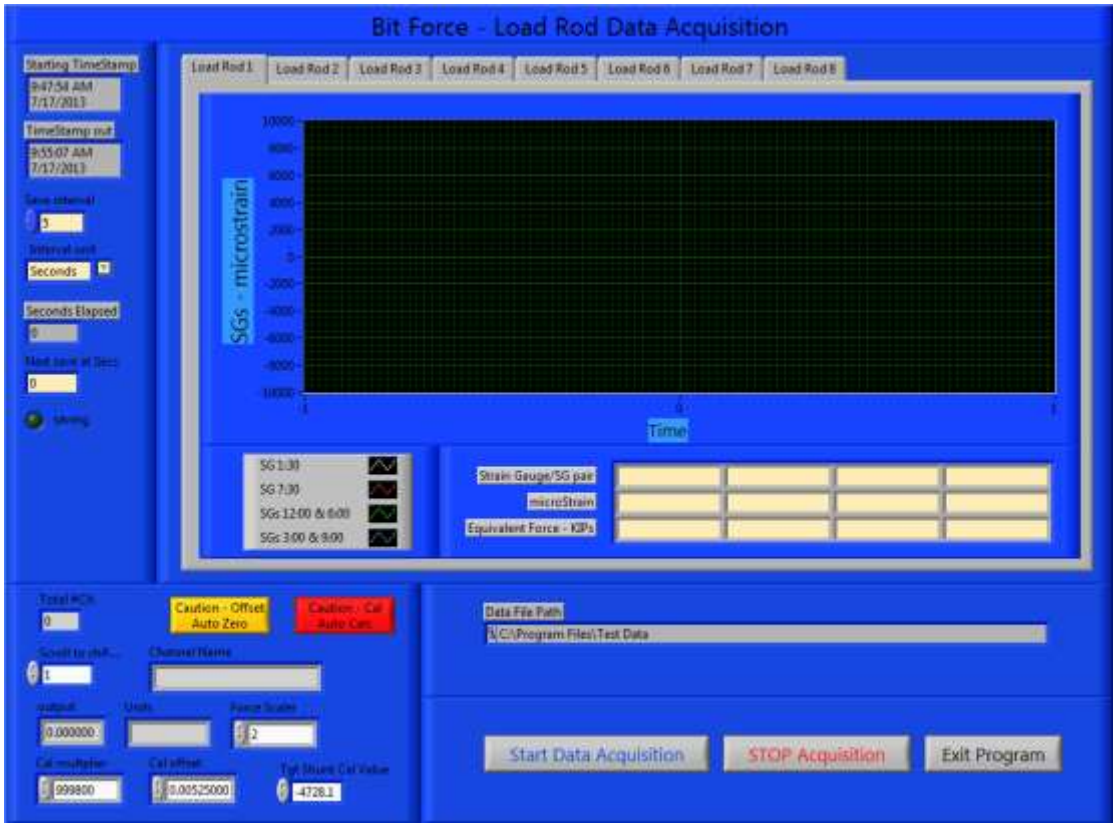

Figure 3.29: LabVIEW front panel of rod calibration program designed by TAMU CVEN

The main issue that was faced with the CVEN program is that only the front window was accessible to the users. Due to code copyrights, there was no access to the block diagram. This presented a problem because there were more sensors that needed to be added the program, and the interface was not ideal for seeing multiple inputs per channel. The data displayed for each rod was on a separate tab so only one measurement could be viewed at any given time.

These problems led to the development of the current program being used for the drilling rig. This program was created by VCEL and as such has the potential to be modified and

upgraded to meet the perceived needs of the test rig. It can also be used as a basis to develop new codes that focus on different parts of the rig. The front panel of the program allows the operator to see all forces on the same screen to be able to get a real time visualization of what data is being collected and to identify any abnormalities that may make the data collected invalid if not corrected.

This front panel is divided into two separate tabs. The first tab shows all data as numerical values. These values include all of the forces being measured, as well as the offset values, raw mV output of all channels and the position of the carriage as shown in Figure 3.30. The second tab displays a time graph of all load readings from the axial/torsional load cell and the lateral force measurement rods as shown in Figure 3.31.

The program is equipped with an auto zeroing function for all strain gauge rods due to the rods sensitivity to temperature. Since it is assumed that temperature would not be a constant from test to test, an auto zero function for all 32 strain gauge channels was deemed necessary to avoid long set up times associated with manual zeroing. However, the load cell channels are not included in the auto zero as they are somewhat less sensitive to temperature. However, a change in offset has been observed between tests so a manual zero feature was included for the WOB and TOB channels of the load cell. As for the string potentiometer, the offset is crucial to know the absolute position of the carriage and it is completely independent of temperature so it only has a manual offset value that depends on the length of the bit as stated in Equation 3.1.

Since most of the crucial information obtained from the tests will be determined from post processing, the program has a simple record data feature. When selected, the record button brings up a prompt screen to name the data file. During the course of the test, whenever the record button is activated, it will append the data to the file specified at the beginning of the test. This file is saved as an LVM file which can be opened and converted in Microsoft Excel. The data recorded by the program contains 28 columns,

these are: time, carriage position, WOB, TOB, the lateral load of each rod, and the frictional components of WOB and TOB measured by each rod.

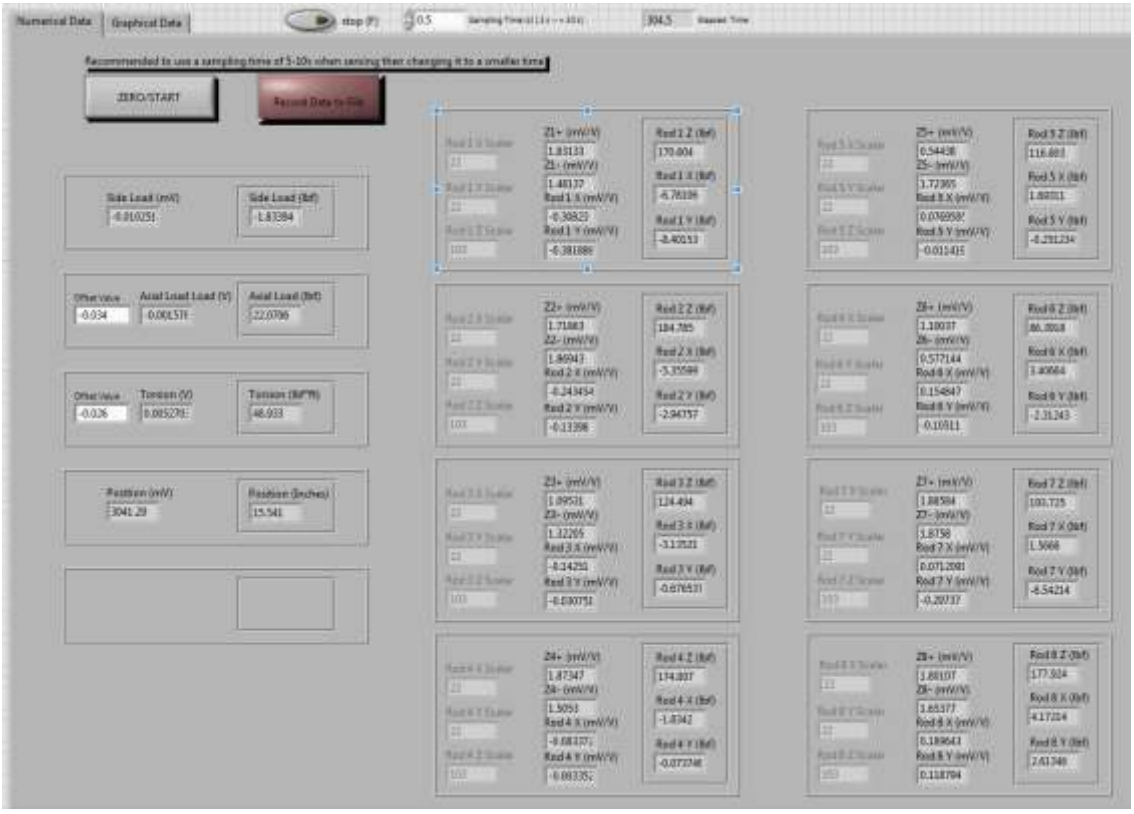

Figure 3.30: Numeric display of the current LabVIEW front panel used with the test rig

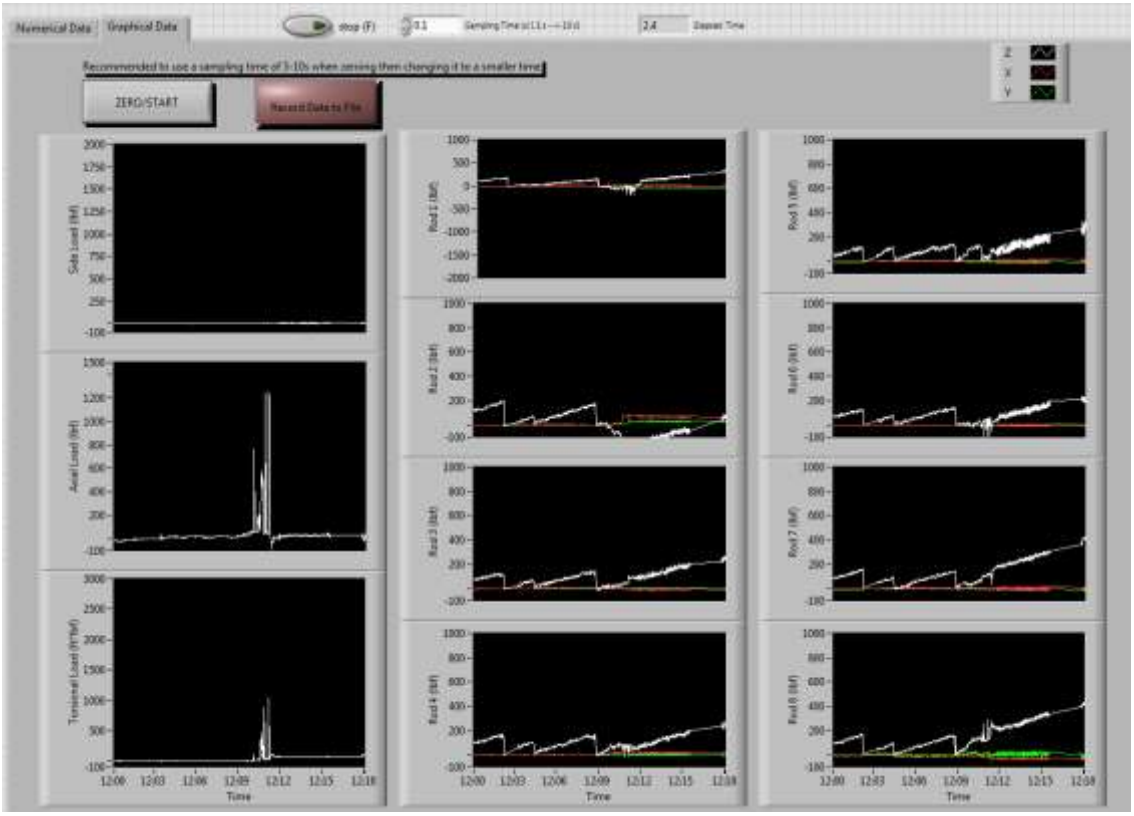

Figure 3.31: Graphical display of the current LabVIEW® front panel used with the test rig

The block diagram of the bit force measurement VI is set up into sections to divide the individual sensors as shown in Figure 3.32. Each sensor is essentially the same in that all raw data is collected and averaged according to how fast the user would like to collect data. After the averaging, the data is split into individual sensors and processed according to the sensor. The lateral load rod strain gauges go through a feedback loop to save the offset value that is automatically generated when the program starts. Once the data is processed and sent to the user front panel for live data, the data is then sent to the "write measurement to file" VI where it is recorded and saved for further analysis and post processing.

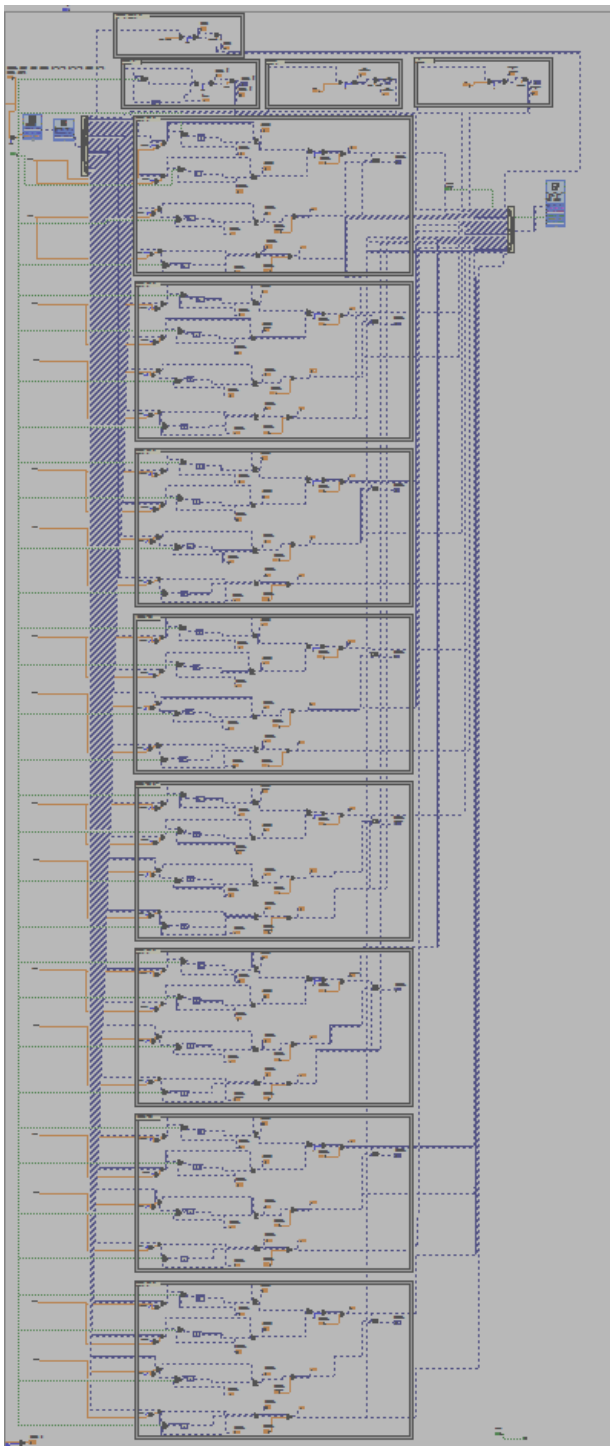

Figure 3.32: Full block diagram of bit force measurement LabVIEW® VI

4. RIG ANALYSIS

4.1. Structural Analysis

The shaft was one of the first components analyzed. As mentioned previously, one of the functions of the rig is to test the stiffness properties of the formation sample. This test would utilize a side load to measure the relative displacement between the shaft and the formation sample. For this reason, it was important to estimate the deflection in the drill shaft under a side load. Very low deflection is desired to keep the system in alignment, but that absolute maximum deflection allowable is 1.5 inches which would cause the side load jack to push the lateral load rod support cylinder out of place and cause it to fall. To predict the deflection, two cases were analyzed to estimate the deflection in the shaft. The model of the shaft used is found in Figure 4.1. The first case was assuming that the bearings were rigid supports. The bit was assumed to have a transverse load of 3000 lbf as due to the fact that the side loading jack on the drilling rig has a maximum capacity of 1.5 tons. This model estimated a maximum deflection of 0.13 inches. The second model assumed that some angular deflection was present and thus the bearings were modeled as pin connections. This analysis produced a max deflection of 0.24 inches at the bit for the same load as the first.

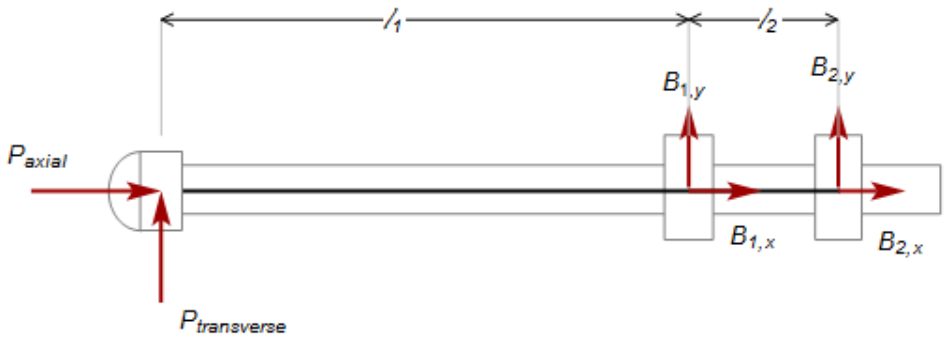

Figure 4.1: Load and support model for drill shaft

For additional analysis, a bearing stiffness calculation was done to see how much the bearings would contribute to the deflection of the shaft. This analysis was performed assuming a rigid shaft. These results were superimposed onto the flexible shaft results to predict the total deflection. The percent contribution from the deflection in the bearings to the total deflection seen was calculated and is shown in Figure 4.2. As seen in the figure, the bearings contribute to less than 1% of the deflection if stiffer than 100,000 lbf/in. After contacting SKF concerning the chosen bearings, it was revealed that the exact stiffness of the bearings is a nonlinear function dependent on the load applied to it. However, based on the few data points given, the stiffness of the bearings were predicted to always be stiffer than 500,000 lbf/in. Under this premise, the deflection due to the bearings was assumed to be negligible. Also, due to the high stiffness of the bearings, it was assumed that they would behave more like rigid supports than pins. It can then be concluded that the deflection in the shaft is acceptable and will not cause any issues in the reading of the proximity sensor or the alignment of the system. There should be care taken to separate the reaction from the bit and from the shaft seal as there will be lateral forces at both locations due to the deflection in the shaft and in the formation sample.

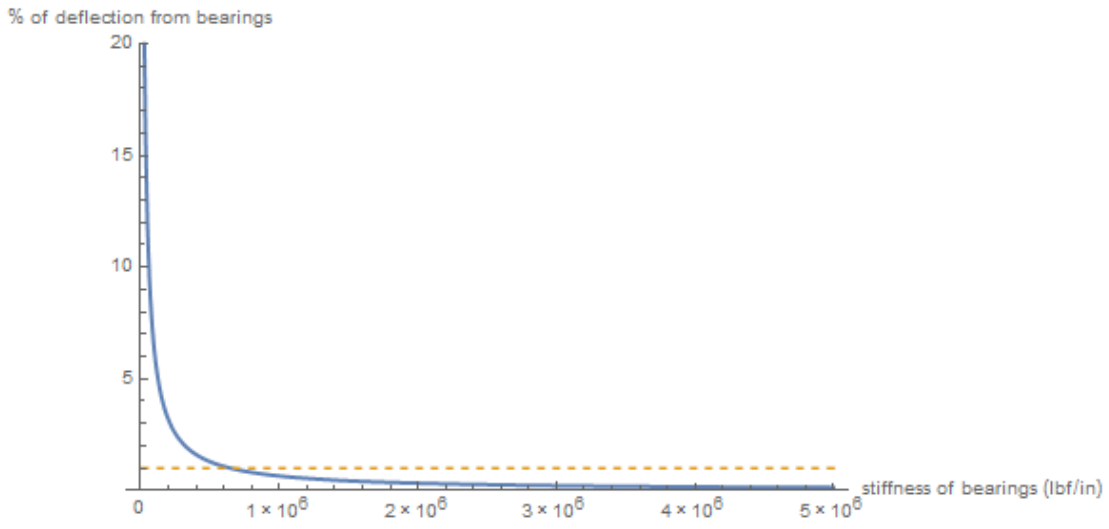

Figure 4.2: Percent of drill bit deflection due to bearing stiffness

Another concern for the design of the shaft was if there was a possibility of exciting a resonant frequency in the shaft. Finite element modeling was used to determine the resonant frequency of the drill shaft to ensure that it would be stable under the operating range. It should be noted that while the max operating speed of the shaft is quite slow, many observations have been made of 3x RPM excitations when using roller cone bits [15]. Using ANSYS® Workbench, the lowest natural frequency was found to be 23.4 Hz which had a mode shape that was comparable to a cantilever beam. The axial, or bit bounce, mode was not included in the results due to this mode shape having a much higher resonance than the maximum calculated mode at 552.9 Hz. With these results, it is shown that no resonant excitation should be expected in the shaft during operation.

The carriage was another point of concern for vibrational analysis since it is the main component of the drilling rig. It was important that the carriage was sufficiently strong and that no resonant frequencies are excited during operation. A full static analysis was done by Wilson during the design phase of the carriage [25]. However, it was deemed necessary that a modal analysis was performed to ensure stability. A finite element

modal analysis was performed and the results of the first five modes are found in Table 4.1. The mode shape result of the first mode can be seen in Figure 4.3. It can be seen from the results that the resonant frequencies are much higher than the operating frequencies.

Table 4.1: Results of modal analysis of measurement carriage assembly

Measurement Carriage Modal Analysis		
Mode	Frequency (Hz)	Frequency RPM
1	57.58	3454.8
2	60.183	3610.98
3	98.11	5886.6
4	105.47	6328.2
5	121.29	7277.4

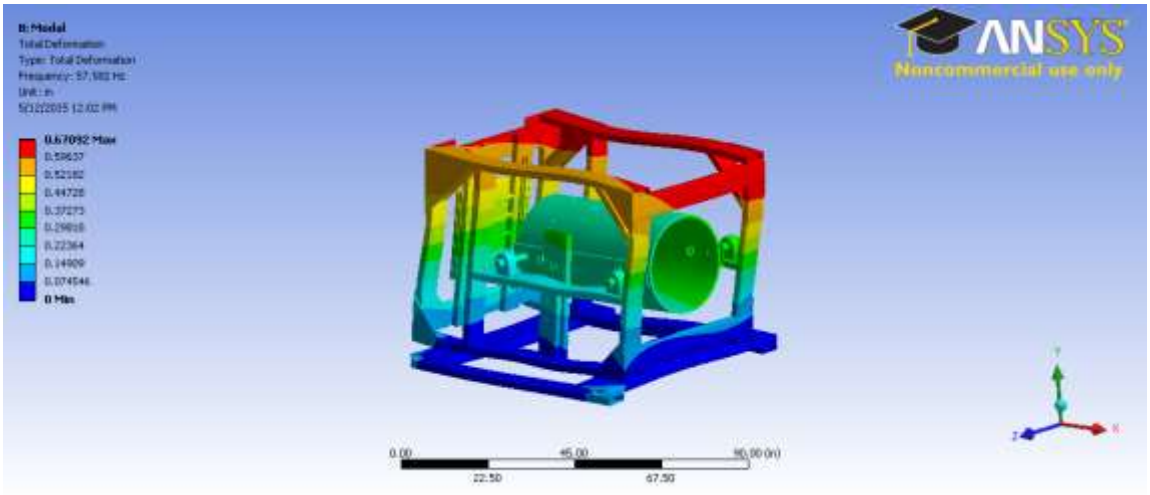

Figure 4.3: FEA modal result showing the mode shape of the first natural frequency

4.2. Cost Analysis

As part of the rig analysis, the budget was analyzed as the rig was being fabricated. Since much of the original budget allocation was based on estimations, many of the actual costs did not match the allocated cost. The forecasted rig budget estimated that the total fabrication costs would be about $15000. This cost included labor and materials. As the rig was being produced, this cost turned out to be $26016, putting the project about $10000 over budget. Also, the original estimated budget did not consider the electrical components needed to power the rig which added another $10000 to the cost. Due to this issue, along with other cost changes such as inflation and availability, much of the components were analyzed for redesign to reduce cost so that the rig could be built reasonably within the proposed budget, while some overflow of the money could be covered by a local account. To reduce cost, the amount of machining required and wasted material was considered as well as the possibility of standard parts. Where plausible, complicated machined parts were simplified into welded structures to reduce fabrication costs.

As part of the cost analysis, the vertical vibration measurement rig was also considered. Although, this component is not complete, it is a much simpler device than the horizontal rig and would only need a few weeks to manufacture and to purchase the parts. The fabrication of this rig was delayed due to insufficient resources and time. This funding issue came about due to the unforeseen costs and fabrication expenses that were needed to complete the horizontal rig. The proposed budget for the items needed to complete the rig can be found in Table 4.2. This estimated budget does not account for the cost of the sensors needed to measure the vibrations in the BHA.

Table 4.2: Projected Budget to build vertical test rig (does not include sensors)

Year 3 Part List	Cost	Source	Part #
Belltec NC250 Auger Drive	$ 1,548.00	http://www.equipmentland.com/produ	BEL-NC-200-113026
Precision Slide 4.5" stroke (x2)	$ 567.86	mcmaster	5236A16
Right angle gear drive (x2)	$ 325.46	mcmaster	6456K11
Drill Pipe (2 3/8 Mayhew Jr.)	$ 2,590.00	RockBuster Drilling Supply	
Swivel	$ 972.79	America West Drilling Supply	
Sub1	$ 607.47	America West Drilling Supply	
Sub2	$ 275.00	Venture Drilling Supply	
Raw Materials	$ 700.00	DiscountSteel	
Flanges and nipples	$ 562.12	Mcmaster	68095K177
Fabrication	$ 900.00	Verbal Quote	
TOTAL	$ 9,048.70		

5. CONSTRUCTION OF RIG

Careful consideration and engineering was used to develop a test rig that would best produce the measurements needed to create an accurate BFIL database. This design underwent various minor modifications to reduce build cost and/or to improve functionality. The fabrication process required a lot of help from outside fabricators and vendors. Working with these experts, further modifications were made to improve the rig. The horizontal rig was finally completed and made functional on May 4, 2015.

The bulk of the effort over the course of this project went into the construction of the rig. Over the duration of the project, various issues arose that caused major and minor delays along with additional design and analysis work. These issues ranged from logistics, to budget issues, to miscommunication, to design mistakes. This section will cover a summary of some of the major challenges faced and some of the major milestones in the construction of the rig.

At the time that the work presented in this thesis started, the sample carriage system was mostly complete as shown in Figure 5.1. There was some additional welding work that needed to be done on the sample carriage for its completion. At the beginning of this project, there was a need to ship the sample carriage assembly to a manufacturer to be completed. It was also foreseen that eventually, this and the full completed rig would also need to be transported to the testing location, which at this time had not been finalized. After researching options, it was found that since the components only needed to be shipped a maximum of about 45 miles, that a tow truck company provided the least expensive option and was generally available quickly if needed.

Figure 5.1: Progress of construction of drilling rig when work of this thesis was commenced.

The existing rig components and the additional frame technical drawings were sent to OTBOG Energy for fabrication. The major components were fabricated by them while some of the machine work and smaller items were done at Texas A&M University or outsourced to other nearby machine shops. These smaller items were then often sent over to OTBOG to be welded onto the rig structure. Once the major work on the rig was completed, the frame was shipped over to Texas A&M University Riverside Campus to be assembled as shown in Figure 5.2 on October 20, 2014.

Figure 5.2: Bit force measurement drilling rig after outsourced fabrication was completed

Once the frame was completed and fabricated, there was still a lot of work that was required to turn the frame into a working drilling rig. Among one of the first priorities was to protect the rig from wind and rain. This was very important to ensure that the motor and other electrical components were not damaged or destroyed by weather. Protection was also needed to prevent rapid oxidation on the exposed metal, this was especially important for the carriage guide rails. For this purpose, a 30 ft. tarp garage was purchased to cover the rig as shown in Figure 5.3. This cover provides protection from rain while still being light and portable to allow access to the rig if heavy components need to be relocated using a forklift.

Figure 5.3: Protective shelter put over rig to protect components from the elements

The next major step in assembly was the addition of the guide rails and the formation sample carriage base. Due to alignment purposes, the holes on the guide rail support tubes to mount the rails were not drilled. It was of crucial importance that the guide rails were perfectly parallel so that the carriage would not lock up at any location along the rails. In order to ensure that the rails were parallel, the linear bearings were attached to the base of the sample containment carriage. The rails were pushed to one side and a hole was drilled into the guide rail system frame for the ends of the rails so both rails were free to rotate about the end. One rail was then squared and measured and two more holes were drilled in order to fix the one rail in place. The second rail was then fixed at one end so it was still free to rotate. The carriage base was then slid across the rails to various locations to ensure that the rails were parallel while the holes were drilled. After the aligning procedure and installation of the rails, the guide carriage base was pushed up and down the track and no locking or seizing was observed, thus demonstrating that

the rails were parallel. A photograph taken during the rail installation process is shown in Figure 5.4.

Figure 5.4: Installation of guide rails and sample carriage base

The next major step in assembly was to place the sample containment carriage body onto the base that had been installed. Once in place, the lateral load rods were inserted into the support cylinder as shown in Figure 5.5. It was required for these rods to be inserted from the inside due to the strain gauges near the end. This makes it so the installation of the rods is required before the sample containment cylinder can be put into place. Once the rods were installed, the sample containment cylinder was lifted and slid into place as shown in Figure 5.6.

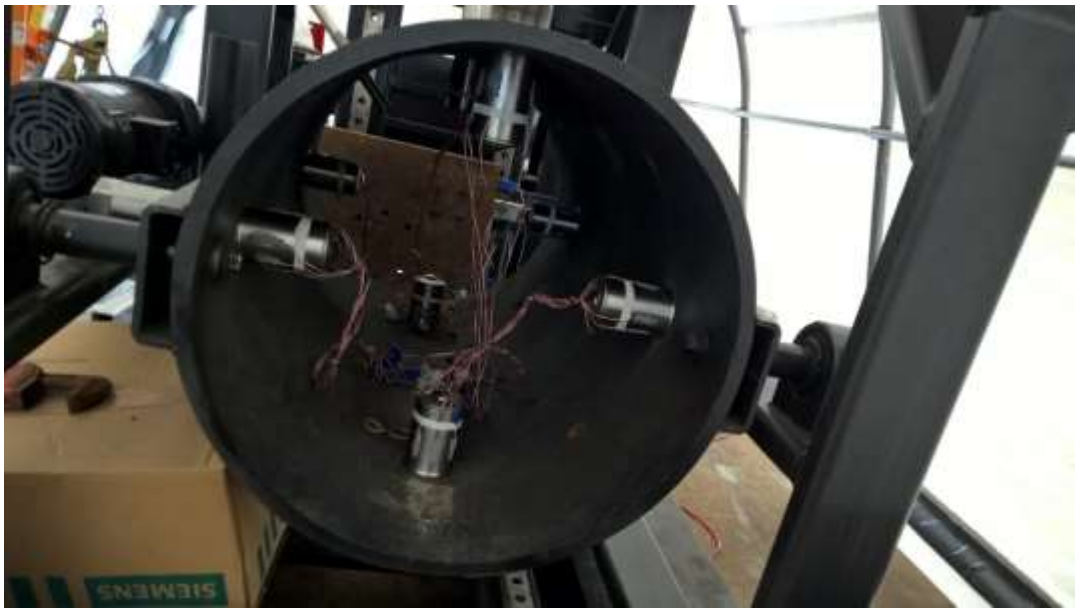

Figure 5.5: Installation of lateral load rods

Figure 5.6: Installation of sample containment cylinder

Once the sample containment cylinder was in place, the main load cell was bolted onto the back. This required a long extension due to the need for bolts to be inserted from the very back of the sample containment cylinder. This final step completed the sample containment carriage and allowed for the wiring of the sensors into the data acquisition system.

Another important step was to weld on support tabs for the hydraulic cylinder as shown in Figure 5.7. This welding work was done in parallel with other minor welding work that needed to be done. The welding that needed to be done by VCEL included the motor support beams, the gear reducer support beam, the bearing housing mounting blocks and all safety covers. With this welding work, the hydraulic pump was mounted and all hoses were attached to the cylinder as shown in Figure 5.8. In order to allow for the control of the ROP, a flow valve was installed onto the inlet of the hydraulic cylinder.

Figure 5.7: Hydraulic cylinder support tabs tacked into place

Figure 5.8: Hydraulic cylinder system fully installed with pump and regulator

Among the work that needed to be accomplished to make the rig functional was to align all drive components and install the couplings and mounting structures. Also, at this time, the shaft was still being machined by an outside vendor. The shaft took some time to be machined which caused major delays since it was needed to assemble the bearing system and to complete the alignment process.

Once the shaft was machined and completed, another issue surfaced concerning the bearing housing design. The shaft was designed to have a shrink fit for the bearings. Using a shrink fit would allow for an axial load to be supported by the bearings. The plan for the shrink fit was to dip the bearing end of the shaft into liquid nitrogen until it got cool enough for the bearings to slide on easily. On the first attempt, the first bearing would not slide on. On the second try, the first bearing slid freely down half way where it stopped and froze to the shaft. These difficulties were caused by the fact that the dewar did not have a large enough capacity to sufficiently lower the temperature of the entire

section of shaft. This setback required the shaft to be sent to a drive shaft company to be pressed on. After the first bearing was on, the shaft was dipped back into liquid nitrogen and the bearing was heated to 150° F to avoid another stuck bearing. This solution allowed for the easy assembly of the remaining spacers and bearing as shown in Figure 5.9. These issues caused delays and additional cost due to the multiple attempts and purchase of nitrogen, along with the time and money required to get the bearing professionally pressed on.

Figure 5.9: Drill shaft with bearings and spacers installed before insertion into the bearing housing.

With the completion of the bearing assembly, the alignment of the drive system was finally completed and all components were mounted into place as shown in Figure 5.10. The alignment started with the drill shaft so that it would be parallel with the motion of the sample containment carriage. This was done by measuring the concentricity of the

shaft and the tube with the carriage at the most retracted position and again at the fully extended position. The other components were then aligned from the shaft backwards.

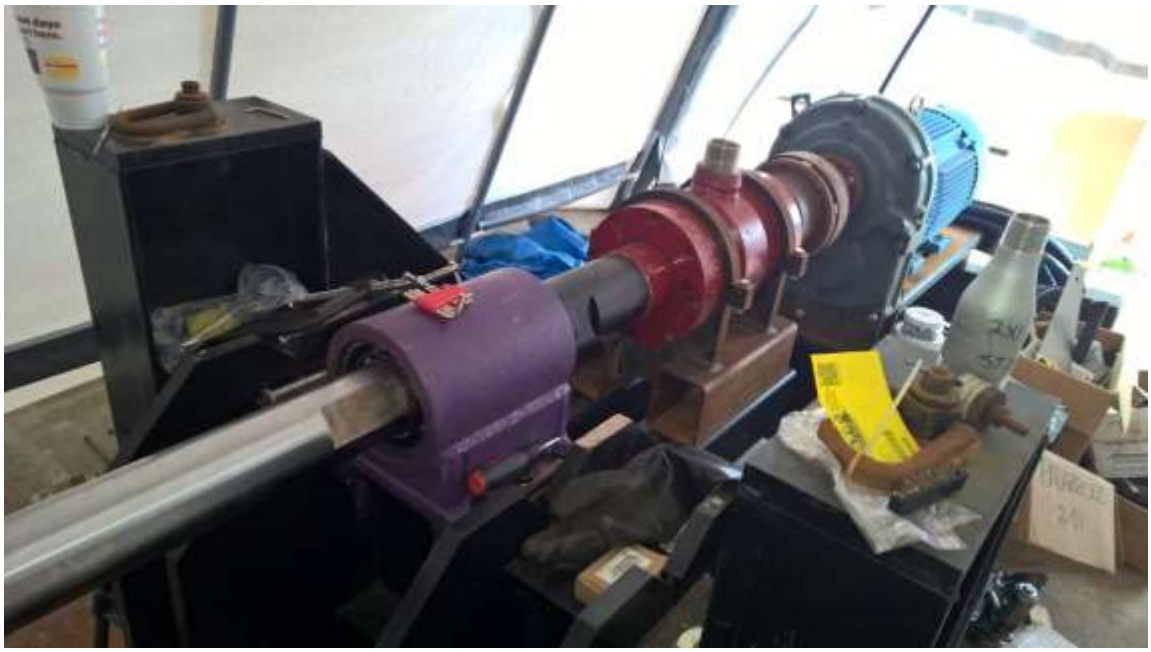

Figure 5.10: Drilling rig drive system aligned and mounted into place

With the completion of all components, the formation sample was inserted and secured into the sample containment carriage and the mud drain/shaft seal assembly was placed over the shaft and secured onto the sample containment cylinder as shown in Figure 5.11.

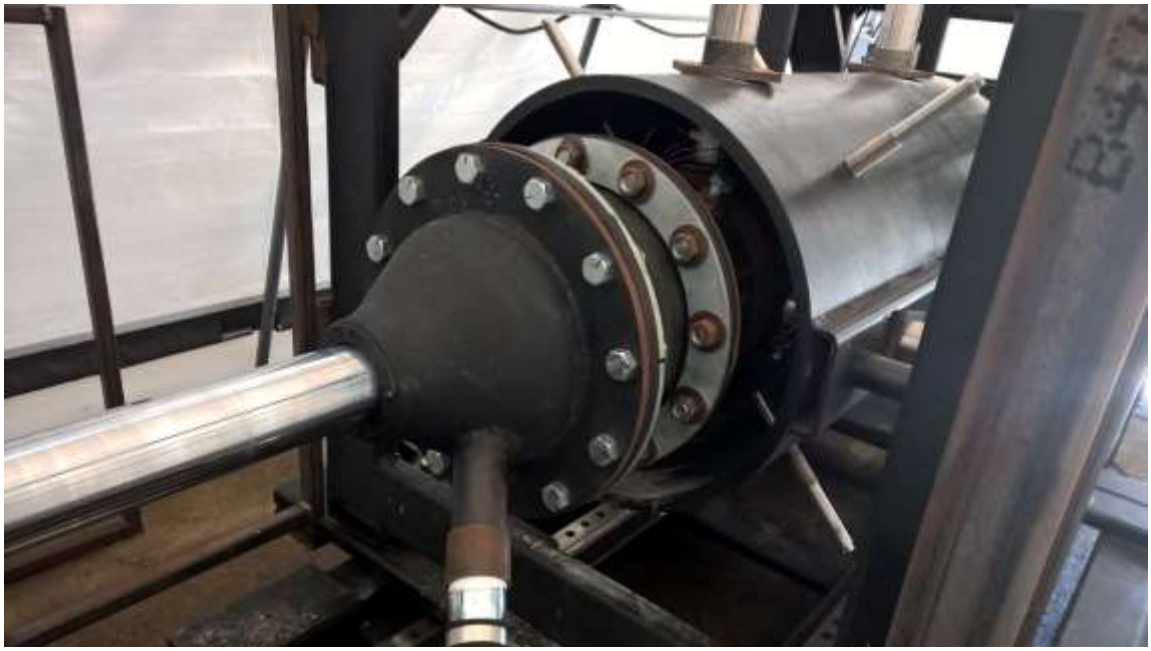

Figure 5.11: Mud drain system mounted onto sample containment cylinder

At this time, the rig is functional and the preliminary test results will be discussed in a proceeding section. Although the rig is functional, it still requires some minor work and modifications to include other tests that may be performed. The current functional test rig can be seen in Figure 5.12 and Figure 5.13. An overview of the rig and its operation can be found online at https://youtu.be/_AyXrKv-t74.

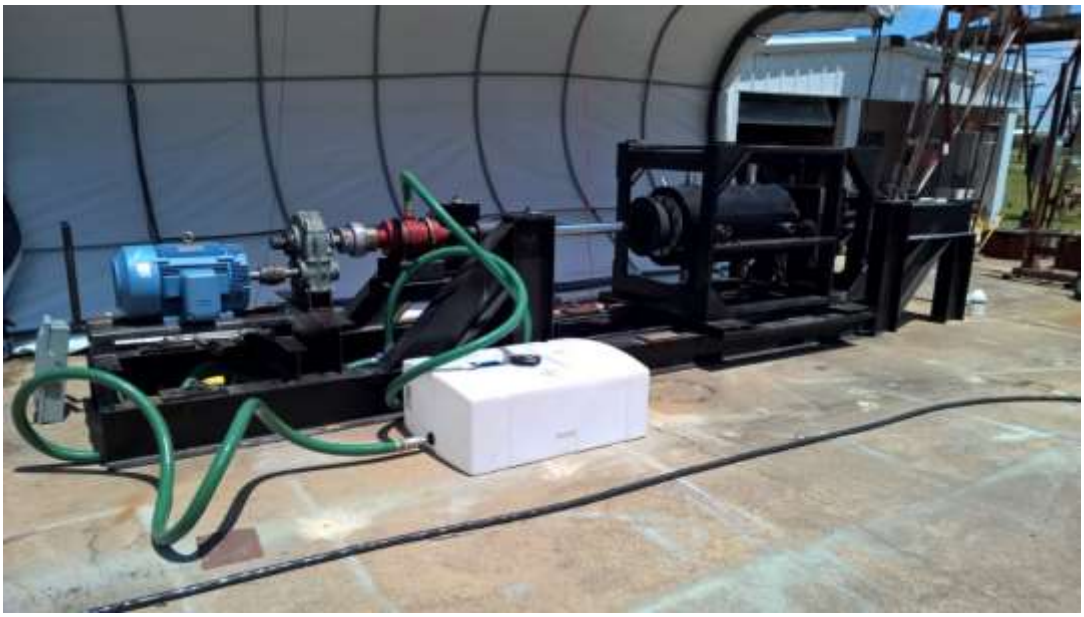

Figure 5.12: Completed Horizontal Drilling Rig Assembly

Figure 5.13: Completed Horizontal Drilling Test Rig detailing the drive assembly

6. TEST SET UP

6.1. Testing Procedure

There are multiple tests that are recommended to develop a full force law on the BHA. Due to the high complexity of the system, multiple tests are required to uncouple the effects of the fluid properties, flow rate, bit geometry, weight on bit, shaft speed, rate of penetration, formation stiffness, etc. Although only some tests will be recommended in this section, it is assumed that a variety of tests on drilling effects and formation properties could be derived from the test rig with or without additional modifications. For this study, the main loads of interest are shown in Figure 6.1

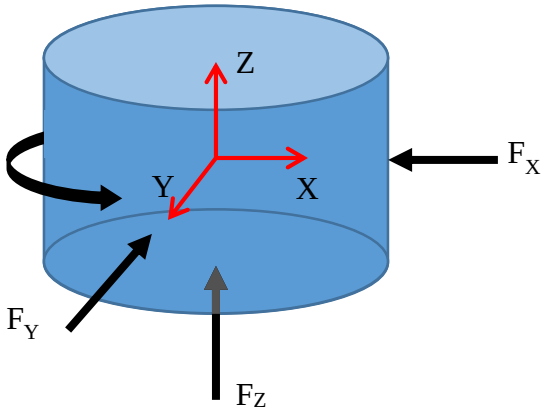

Figure 6.1: Generalized loads acting on the bit

Although this figure is a very simplified model of the bit, it should be noted that each component is made up of multiple forces. For example, the torque, T, includes the cutting torque of the bit, the frictional torque of the bit and the fluid damping torque. The lateral loads, F_X and F_Y, have a component that is related to the stiffness of the formation

and a component of the lateral damping of the drilling fluid. The axial force, F_Z, has a cutting and a frictional component as well as some fluid damping effects and formation stiffness effects. The purpose of this rig is to separate these variables so that the forces acting on the bit can be better understood and modeled.

6.1.1. Standard Drilling Operation

The first standard test is a simple drilling test. This test simply involves the penetration of the spinning bit into the formation sample without adding any side loads. This test should be done in stages to uncouple the forces on the bit. For example, it would be important to determine the amount of torque that is from the bit/formation interaction and the amount from the circulating fluid around the bit and the drill shaft. It may also be of interest to determine how much of the force is from the cutting component and how much is from the frictional component as discussed in the introduction.

There would be multiple methods for separating the fluid forces from the rock cutting forces. One method may be to drill a hole with no fluid circulating, followed by a drilled hole with fluid circulating. For additional data, after the hole has been drilled, one could spin the bit with no ROP and measure the fluid forces during the spin. Doing a test with no fluid, a test with no cutting and a normal full test may appear to be redundant; however, it is always a good idea to get more data. Also, it may be required to fully uncouple the forces as the fluid may affect the cutting efficiency along with the added damping forces which would only be observed from doing all three tests.

Another important requirement for the standard drilling operation is to determine the relationship for WOB and TOB with test factors such as ROP, bit characteristics and fluid properties. To develop a valid model for this, one would need to do many tests with changing ROP. To determine the factor of each, a testing matrix could be developed to determine the effect of only one component. For example Table 6.1 shows a test matrix

that assumes that there are only four test variables: ROP, RPM, formation characteristics and fluid characteristics. This matrix assumes that there are only two possible values for each variable. Utilizing a table such as this could ensure that all variables could be tested at all determined values while all others are considered constants. It should be taken into account that a test matrix for this rig would be much larger and more complex than this example. It would most likely include bit characteristics as well as others. Also, each characteristic group would have multiple variables of its own. It becomes apparent that the amount of tests to develop a detailed complete law would be much too large and require too many tests to be reasonable. This is where the user would have to take into account and do some preliminary calculations of what variables are most important and make the most impact. With carefully chosen variables and constants, a good function could be made for both WOB and TOB.

Table 6.1 : Example test matrix to separate different test variables

	ROP	RPM	Rock	Fluid
Test 1	1	1	1	1
Test 2	2	1	1	1
Test 3	1	2	1	1
Test 4	2	2	1	1
Test 5	1	1	2	1
Test 6	2	1	2	1
Test 7	1	2	2	1
Test 8	2	2	2	1
Test 9	1	1	1	2
Test 10	2	1	1	2
Test 11	1	2	1	2
Test 12	2	2	1	2
Test 13	1	1	2	2
Test 14	2	1	2	2
Test 15	1	2	2	2
Test 16	2	2	2	2

6.1.2. Formation Stiffness test

The formation stiffness test would be a smaller portion of the testing. This test would require a pre-existing drilled hole. The bit would be inserted into the hole until it is completely encased by the formation sample. The side measurement proximity probe would then be moved into position to get data for the lateral displacement of the rod. The side load jack would then be engaged to press against the side of the bit. The lateral load rod measurements could then be transformed into the side load on the bit. This side load along with the relative displacement of the formation wall could be used to determine the stiffness of the formation.

Another side load test that could be done is to do the same test but with the bit rotating. This data could give some valuable information on the frictional component of the drilling operation. This may also help develop some directional drilling data to determine the side cutting characteristics of the bit.

6.1.3. Lateral Fluid Damping Shake Test

Just as with the side load tests, the lateral damping test would require that a previous standard drilling test was performed on the sample. For this test, to ensure clearance for the shaft to move, the bit would need to be removed from the shaft. The shaft would then be inserted into the drilled hole, and the formation sample would be actuated at different frequencies. The acceleration of the sample and the measured forces would then be used to determine that lateral damping of the fluid. It should be noted, that at the present time, the test rig is not equipped to measure the sample acceleration. It is recommended that an accelerometer is added to the data acquisition system and secured onto the lateral load rod support cylinder

6.1.4. Deriving Bit Forces from Measurements

Determining the forces acting on the bit from the measured lateral, axial and torsional loads from the sensors is a very complex transfer function that depends on the stiffness of the formation, bit, structure and the sensors. This transformation of measured loads to actual load would be frequency dependent as is the case in any dynamic system as shown in Figure 6.2. This figure shows the magnitude plot of the transmissibility of a standard system. The transmissibility is the amplitude ratio of the forces transmitted to the system support to the excitation force [29].

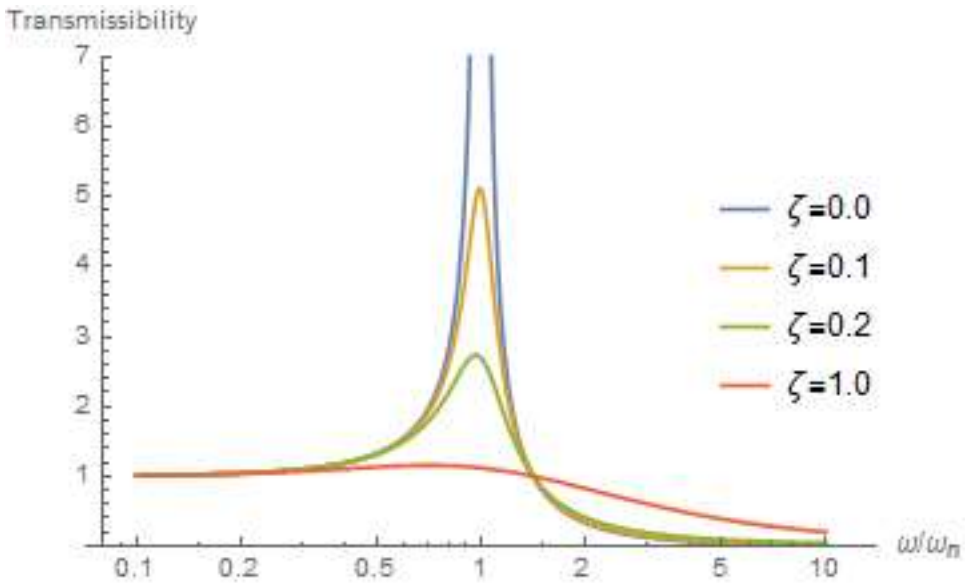

Figure 6.2: Transmissibility plot for a dynamic system

In this case, the excitation forces are those being produced by the bit, and the forces in the supports are the forces measured by the sensors. The figure represents a simplified 1 DOF system, however, the principal remains the same that at low frequencies much less than the resonant frequency of the system, this ratio can be assumed to be equal to 1. As

noted in the analysis, the natural frequencies of the system are much greater than the operating frequencies. In this system, the frequency ratio at the lowest natural frequency is expected to be around .03. With this in mind, the assumption can be made that the output, or measured forces, are equal to the input, or drill bit forces. Under these assumptions, the transformation was made assuming a static rig as shown in Figure 6.3. This figure shows all measured forces in blue, drill bit forces in red and the dynamic shaft seal forces in green. This model was made under the assumption that the frictional components from the lateral load rods and from the dynamic shaft seal have known relationships to the other measurements and are included in other values or neglected. In the diagram, d is the depth of penetration into the formation.

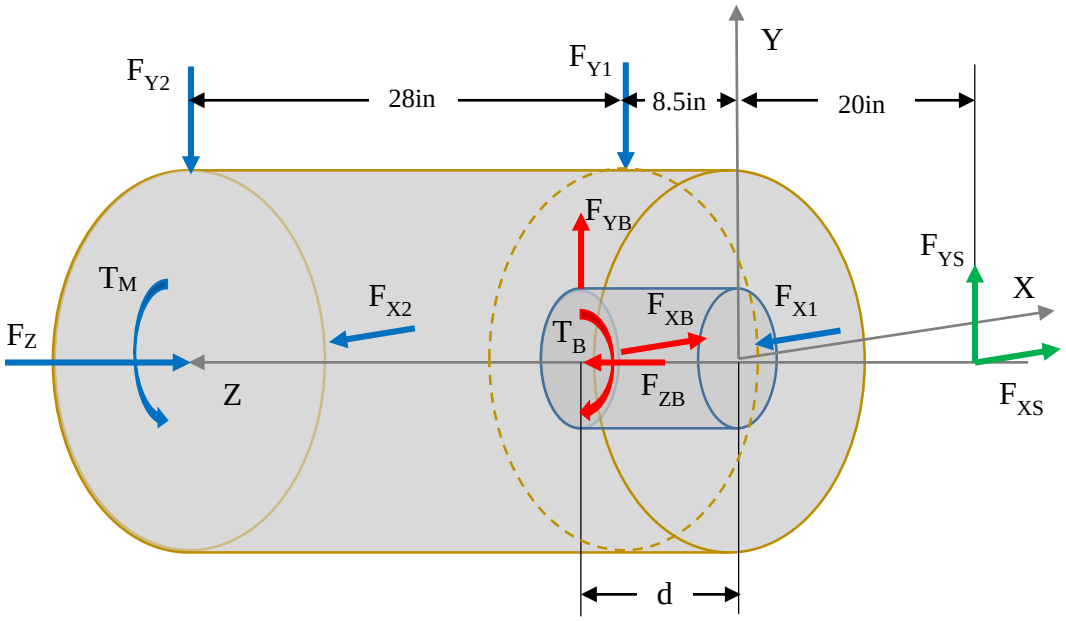

Figure 6.3: Free body diagram showing forces acting sample containment cylinder

Applying Newton's laws to the formation, the unknown forces can be inferred from the measured forces as

$$WOB = F_Z \tag{6.1}$$

$$TOB = T_M \tag{6.2}$$

$$F_{XB} = \frac{28.5F_{X1} + 56.001F_{X2}}{d + 20} \tag{6.3}$$

$$F_{YB} = \frac{28.5F_{Y1} + 56.5001F_{Y2}}{d + 20} \tag{6.4}$$

$$F_{XS} = \frac{F_{X1} + F_{X2} - 8.5F_{X1} - 36.5F_{X2}}{d + 20} \tag{6.5}$$

$$F_{YS} = \frac{F_{Y1} + F_{Y2} - 8.5F_{Y1} - 36.5F_{Y2}}{d + 20} \tag{6.6}$$

6.2. Initial Test Parameters

Once the bit formation measurement drilling rig was complete, some initial testing was done in order to provide some data on how the rig works and to find any issues that could be included in any recommendations for further work and modifications of the test rig. For these preliminary test runs, some initial parameters were chosen and utilized that can be compared to future data.

One of the key components of the drilling rig is the formation sample. For the initial tests, a formation sample was made on site following the design presented in Section 2.2.

As an easy test to ensure functionality, an attempt to make a very soft formation was undertaken. The general recommended mixture for a good strong concrete is 1 part cement, 2 parts sand, and 3 parts gravel. In an attempt to soften the material and to create a more uniform strength throughout, it was decided to leave out the gravel and add more sand. The concrete mixed for the sample had a 6:1 sand to cement ratio. Finding a good relationship between the concrete lithology and strength was difficult to find, however Figure 6.4 shows an estimated relationship between the cement to sand ratio and compressive strength. According the graph, assuming that we have somewhat good sand at ratio of 1:6, it was estimated that the original formation sample had a compressive strength of about 10 MPa.

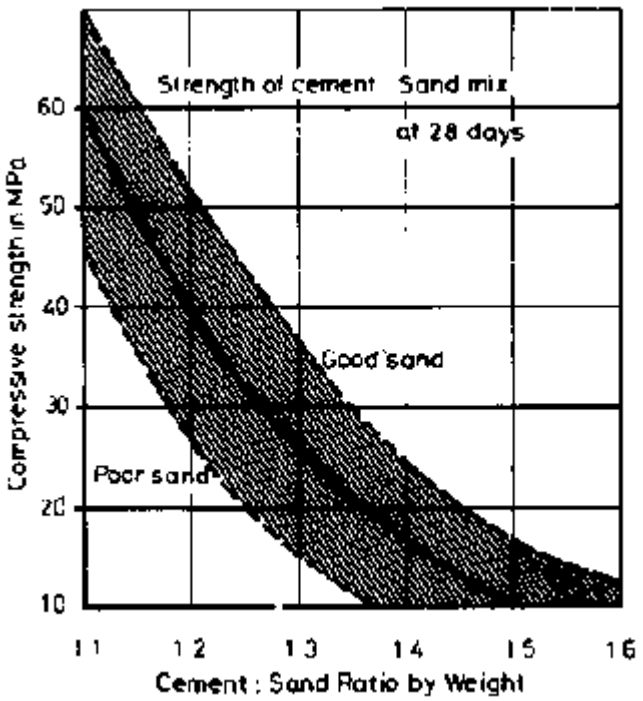

Figure 6.4: Effect on the cement to sand ratio on the compressive strength of concrete [30]

The bit used for initial testing was chosen to be a simple step drag bit as shown in Figure 6.5. This bit was chosen due to low cost and simple construction. The bit has a 4” diameter giving the annulus around the shaft a thickness of 0.5 inches. The bit has 3 blades and a single 1 inch diameter flow nozzle.

Figure 6.5: The 4" drag bit used for initial testing of the drill rig

The lateral load rods were inserted into place and rotated until they came in contact with the formation containment cylinder. From this point, they were rotated further until the next local X_R or Y_R axis was in line with the global Z axis. Knowing this orientation of all the rods is very important for post processing and understanding the frictional loads seen by the rods. It is also important to know that location of each rod in the assembly. The placement of each rod along with the global and local coordinates of the rods and system are shown in Figure 6.6. This figure shows the local coordinate system of rod 2

as compared with the global. Table 6.2 shows the local axis of each rod that is aligned with the global Z and T coordinates. This means, for example, on rod 1, a load in the positive Z direction globally will be read as a positive value in the data acquisition system in the X_R coordinate, while rod 4 would show a negative X_R value for the same load.

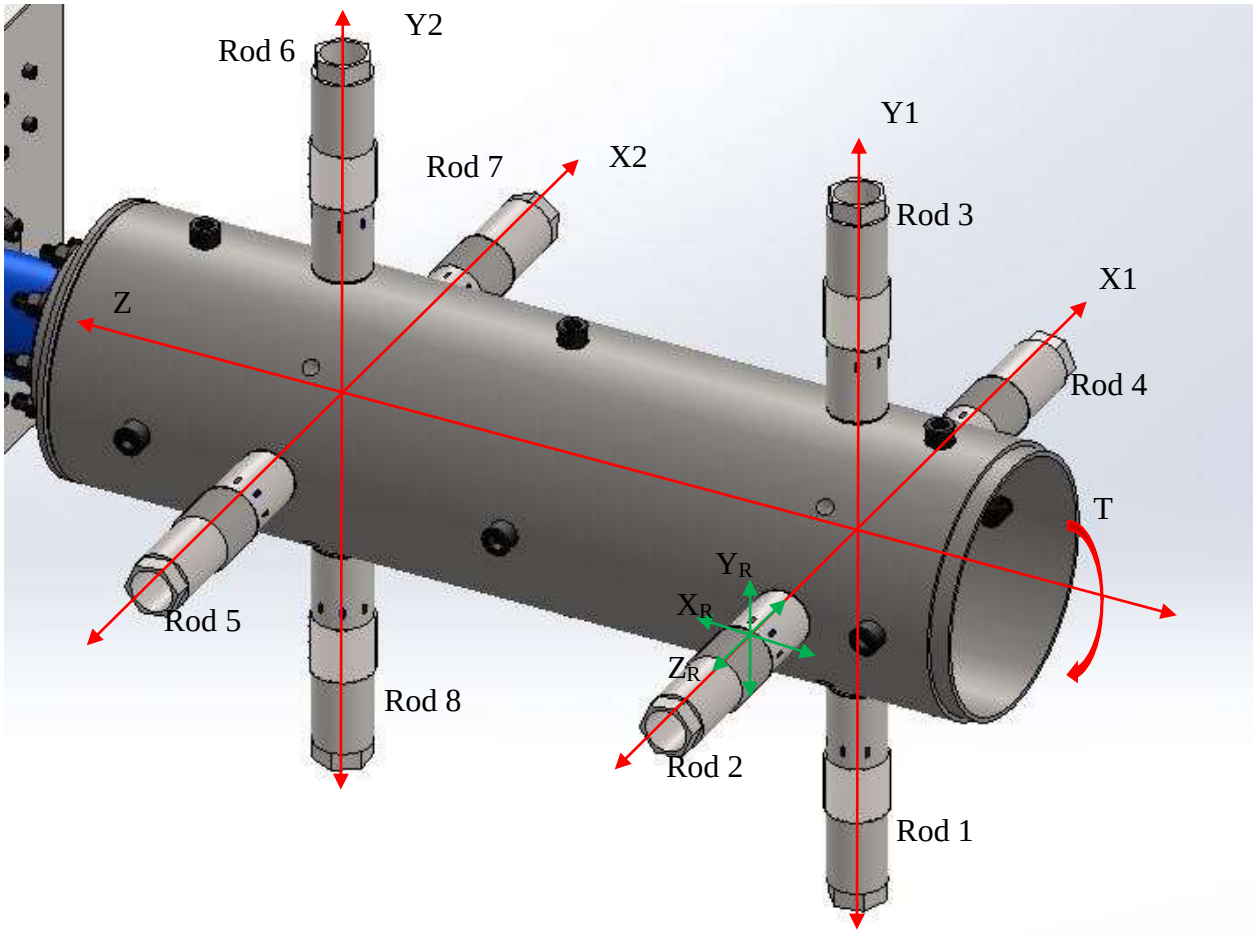

Figure 6.6: Test rig rod location and reiteration of global and local coordinate systems

Table 6.2: Orientation of lateral load rods for friction measurements

Rod #	Local Axis in Z	Local Axis in T
1	X_R+	Y_R+
2	X_R+	Y_R+
3	X_R+	Y_R+
4	X_R-	Y_R-
5	X_R-	Y_R-
6	X_R+	Y_R+
7	X_R+	Y_R+
8	Y_R-	X_R+

The last fixed initial parameter considered was the mud. Due to resources, time and ease of handling and clean up, water was used as the initial drilling fluid. Using water to start was also advantageous in that it allowed for easy viewing of the cuttings and to check for serious leaks.

7. EXPERIMENTAL RESULTS

7.1. Initial Test Data

Upon completion of the rig, preliminary testing was done as a verification that all sensors were working properly and to see any initial correlations in the data. The initial test was done at 30 RPM as a dry run without any fluid flowing. The results of the first test can be seen in Figure 7.1, which shows the axial, torsional and lateral forces acting on the formation over the time period that the test was run. As it can be seen the test was run for 1 minute and 10 seconds. This illustrates the short time period needed to run a test. It should also be noted that this initial test only penetrated into the sample about 3 inches. This short period may result in difficult to interpret data due to the changing geometry of the cutting surface of the bit is it penetrates deeper. It can be assumed that as the bit penetrates deeper into the formation, there should be a higher friction load due to the bit being more fully surrounded by material. Since the output of the data acquisition system only measures the position of the carriage, a 5 point numerical differentiation method was done on the raw data to produce the rate of penetration (ROP) [31]. As it can be seen from the data, the first test was done cautiously and was periodically started and stopped. This was done to ensure that everything was working properly and to experiment with how the system reacts to drilling and if there were any unforeseen issues. The second test run was done at a speed of 50 RPM with water flowing through the annulus as the drilling fluid. This test was run more continuously at a constant feed rate than the first. The second test was done faster than the first only lasting about 30 seconds and penetrating 8 inches into the formation. It should be noted that on the first test, there appears to be correlation between ROP and some lateral reactions, where the second test does not show much lateral loading.

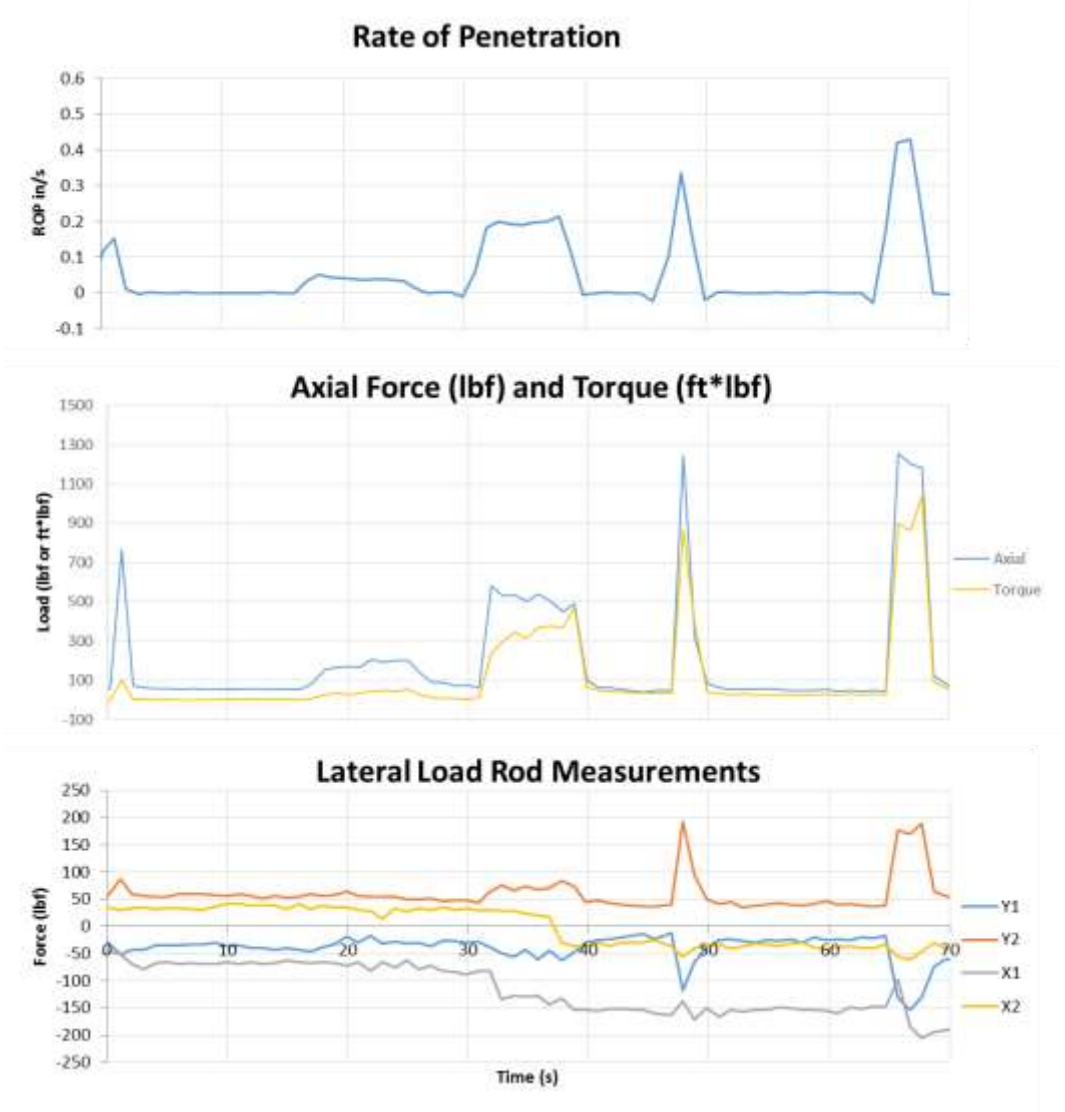

Figure 7.1: The rate of penetration (ROP), axial force, torque and lateral forces of the first dry run of the horizontal rig

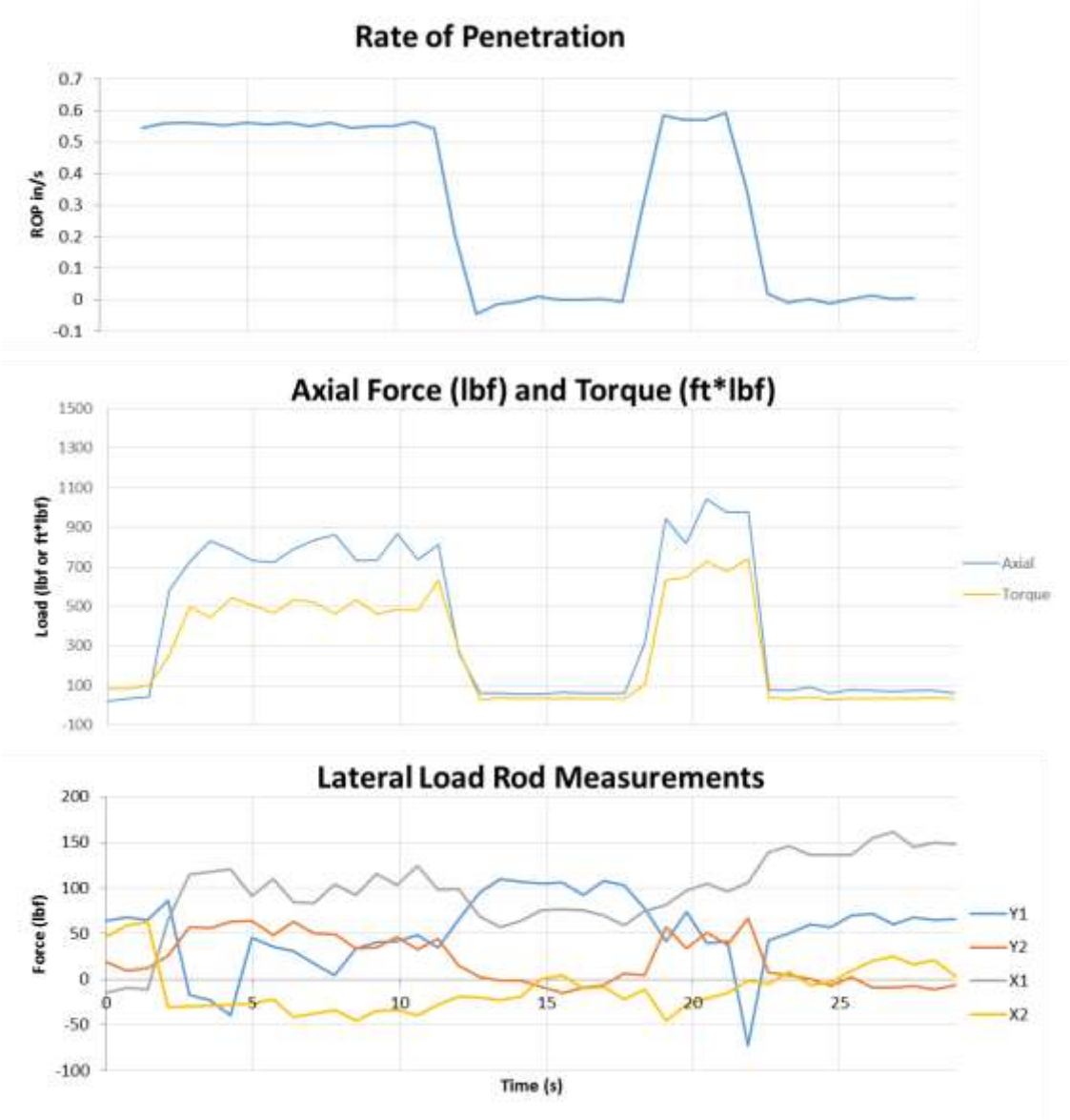

Figure 7.2: The rate of penetration (ROP), axial force, torque and lateral forces of the first wet run of the horizontal rig

Both tests proved that the test rig runs well. There was no excess of noise and no visible vibration response to the drilling. The results from the initial tests show a definite correlation in the ROP and the axial and torsional loads. As mentioned earlier, there was also a noticeable lateral load during the first run. More testing would need to be done to

determine if a lateral load does exist on the bit while drilling. This lateral response could be due to a walking tendency of the bit or it could be from a slight misalignment in the system. It should also be noted that at the beginning of the data in the first run, there is a higher spike in the axial force which could indicate the initial impact of the bit and the formation. This data would produce an outlier for standard drilling, but further investigation into the initial impact forces could be done on the rig to determine the magnitude and severity of these forces while starting.

The results of the tests were tabulated to compare the different operating conditions to the weight on bit and torque on bit as seen in Table 7.1. This data does not represent a full set of experimental data needed to develop an interface law. Further testing is required to get more data points for each of the changing parameters. This data shows the need for further testing, including varying ROP and RPM.

Table 7.1: Summarized test results with varying operating conditions

Test	ROP (in/s)	RPM	Fluid	WOB (lbf)	TOB (ft*lbf)
Test 1	0.05	30	None	150	50
Test 1	0.2	30	None	500	350
Test 1	0.4	30	None	1200	900
Test 2	0.6	50	Water	800	500

Another important piece of data needed from some of the initial test was the frictional force from the lateral measurement rods. As discussed in a previous section, these rods were fixed with stain gauges to measure bending strain due to any frictional force on the rod. This data was recorded and can be seen in Figure 7.3. It appears that there is some frictional force acting on the rods. This frictional force appears to be about 20 lbf on each rod. This would account for approximately 160 lbf of friction that is not being measured by the load cell. In this test, this is about 13% of the axial load. However,

comparing the data to the axial load measured by the load cell, there was very little correlation. Further testing would need to done to determine the effect of varying loads on the frictional support.

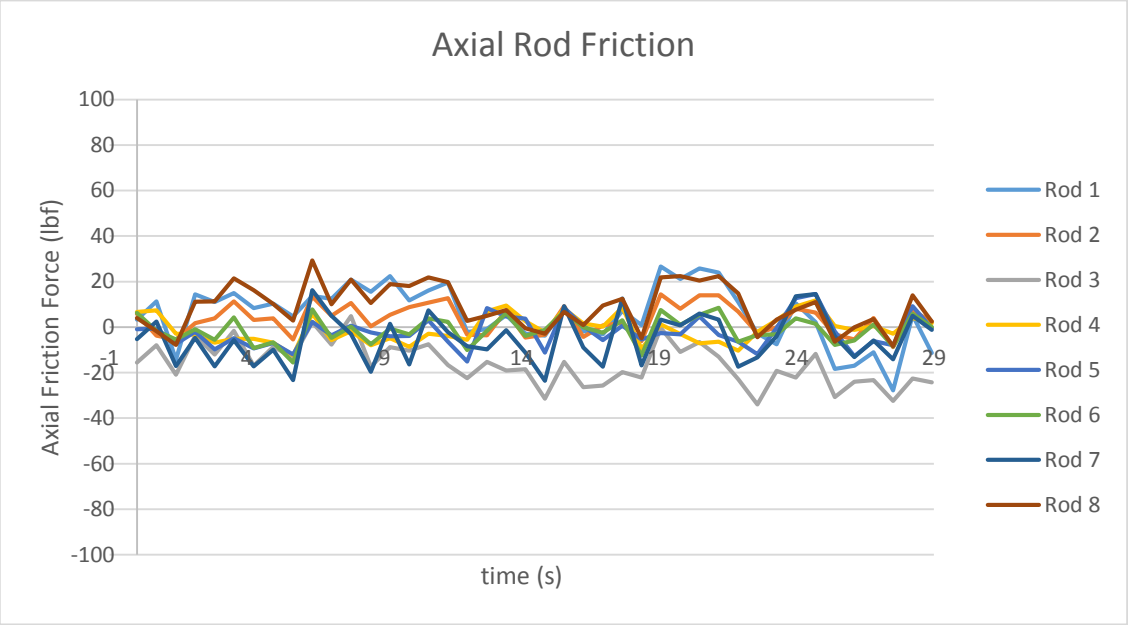

Figure 7.3: Frictional force measured by lateral force rods

Figure 7.4 shows that correlation between the sum of the frictional forces measured in the axial direction of all rods. A linear trend line would suggest that there is a correlation between the axial load and the amount of friction measured by the rods, however, the correlation is not close enough to make any definitive statements about the correlation. It should also be noted that the trend line has a negative offset. Basic physics would indicate that there is not an opposing load measured by the rods, but that there is an offset error in the data collected.

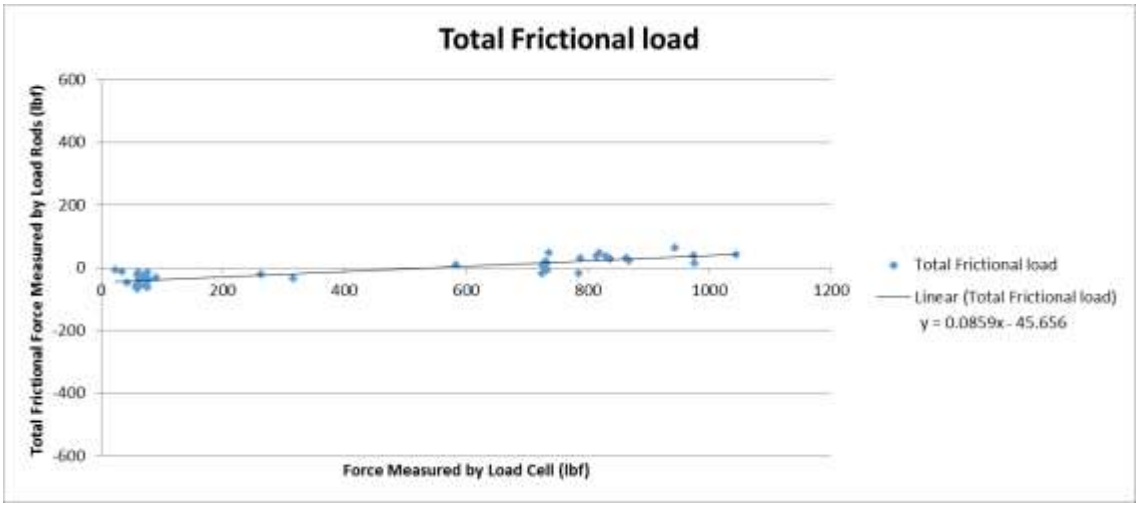

Figure 7.4: Correlation between measured axial load and frictional load

Apart from the force data, it was also important to look at how the machine itself was working. After the initial tests, the drain cap was removed to inspect the drilling quality and to see if the drill was breaking the formation or if it was cutting it. Once inspected, it was clear that the bit was in fact cutting the concrete sample. Pictures of the drilled hole can be seen in Figure 7.5 and Figure 7.6. It was also noticed that the cuttings were of the consistency of course sand as seen in Figure 7.7. This post drilling inspection also showed that the sediment filter designed for the mud tank was collecting sediment on the bottom, and that it was working correctly. It should be noted that at one point during the test, the filter mesh got overloaded with sediment and the filter began to overflow. This was due to improper depth of the inlet hose and it was directing the fluid and the sediment directly onto the mesh.

Figure 7.5: Inspection of the of the drilling quality produced by the initial tests

Figure 7.6: Bottom of the drilled hole of the initial test

Figure 7.7: Consistency of cuttings from initial test sample

7.1. Analytical Results

As an initial validation of how the experimental results from the first two tests compared to the analytical bit to formation interface laws found in literature, some calculation were done to estimate the expected weight on bit and torque on bit measurements. In order to estimate the WOB and TOB measured by the system based on the current bit and general set up, the PDC drag bit equation presented by Detournay et al. was used [11]. This equation states that both of these forces are a sum of a frictional component and a cutting component.

$$T = T_c + T_f \tag{7.1}$$

$$W = W_c + W_f \tag{7.2}$$

where W represents weight on bit and T represents torque on bit. The subscripts c and f represent the cutting component and the friction component respectively. These components can further be broken down and estimated.

To start, the cutting component of the weight on bit is defined by

$$W_c = \frac{2\pi\zeta\varepsilon\, r\, R_b}{\Omega} \tag{7.3}$$

where ζ is a drilling strength to rock strength ratio, ε is the intrinsic specific energy, r is the rate of penetration, R_b is the bit radius, N is the number of blades and Ω is the rotational velocity of the shaft [11]. For this case, the frictional component of the weight on bit is ignored due to the complexity of finding the factors and bit characteristics needed. This assumption would produce results slightly lower than realistic for both the weight on bit component and the torque on bit component. However, the frictional component of the torque on bit was not neglected as it can be found from a known frictional component of weight on bit. Another important relationship is the definition of the depth of cut per revolution which can be found with

$$\delta = \frac{2\pi r}{\Omega} \tag{7.4}$$

With this in mind, the relationship defined in Equation 1.1 between the torque, weight on bit and depth of cut is reduced to

$$T = \frac{\left(1-\mu\gamma\zeta\right)\pi\varepsilon r R_b^{\,2}}{\Omega} + \frac{\mu\gamma R_b}{2} W_c \tag{7.5}$$

where γ is defined as a bit constant. Literature states that a good estimate for a bladed bit, meaning that it does not have multiple cutters per row, this bit constant is defined as

$$\gamma = \frac{l}{2R_b} \tag{7.6}$$

where l is the wear flat or frictional contact surface of the bit. Detournay and Defourny present an example case for finding the needed factors from a tested Berea sandstone sample. Since the material properties of the formation sample used are not entirely known, the factors presented for this sandstone sample were used to estimate the forces on the bit. This set of data was chosen because it presented a somewhat soft formation. While the bit characteristic values were measured or estimated. The values used for the calculations can be found in Table 7.2.

Table 7.2: Values used in bit force calculations

Variable	Meaning	Value	units	Source
R_b	Bit Radius	2	Inch	Measured
l	wear flat length	0.1	Inch	Estimated
μ	friction coefficient	0.82	n/a	Berea Sandstone
ε	intrinsic specific energy	4641	PSI	Berea Sandstone
ζ	strength ratio	0.8	n/a	Berea Sandstone

Using these values, all operational parameters used in the initial test runs were calculated with the presented bit and formation constants. The results can be found in Table 7.3. As can be seen from the results. The model presented by Detournay and Defourny far over predicts the weight on bit force. This value ranged from about 400% to 570% percent higher than those forces actually measured. This could be explained by the difference in bit geometry assumed for the model and that used for the tests. Standard PDC bits used in petroleum drilling have a blunt nose shape while the step drag bit used had a pointed tip which theoretically would have a lower weight on bit to get the same depth of cut. This may indicate a need to include a bit tip constant in the bit to formation interface model to account for these differences. The torque on bit component was actually a

fairly close prediction, where the analytical prediction of the lowest measurement was 53% higher, which translates to predicting only 26.7 ft*lbf higher torque. Some of the higher measurements were closer to 10%.

Table 7.3: Comparison of experimental and analytical results

Parameters		Experimental Values		Analytical Values		Error	
ROP (in/s)	Shaft Speed (rpm)	WOB (lbf)	TOB(ft*lbf)	WOB (lbf)	TOB (ft*lbf)	WOB (%)	TOB (%)
0.05	30	150	50	742.56	76.72	395.0	53.4
0.2	30	500	350	2970.24	306.86	494.0	12.3
0.4	30	1200	900	5940.48	613.73	395.0	31.8
0.6	50	800	500	5346.4	552.35	568.3	10.5

8. CONCLUSIONS

Due to the gap in research as pertaining to the BFIL, a bit force measurement drilling rig was designed and fabricated. The configuration of the rig includes a horizontal rotating drill shaft that drills into the moving sample. The sample is supported by load measurement devices that can read the axial, torsional and lateral forces acting on the bit during various processes. The rig will be used to develop a bit formation interface law for various drill bits and rock types. This rig is also set up to measure the rock formation stiffness properties and the fluid forces.

The completed horizontal drilling rig was tested on a soft concrete cylinder to represent a soft rock sample. While the exact properties of the initial sample are not exactly known, the block was made to be soft to ensure that any issues with the rig would not be catastrophic. The test results produced a correlation between the rate of penetration and the Torque and WOB. These results showed a good response to drilling, however, more data and tests are needed to develop a more accurate correlation.

This data developed from the horizontal drilling rig will be used in conjunction with the vertical drilling rig that will be built and used in an existing well located at Riverside Campus. This rig will measure the vibrations in the BHA both from downhole sensors and from surface sensors.

It is recommended that additional testing be done on the horizontal drilling rig to develop a full understanding of the bit/formation interface law. There is a lot that can be gained from the rig including the effects of various rock hardness and other formation properties, the effect of different types of bits, and the effect of varying rates of penetration and varying RPM. It is recommended that the rig could also be used to measure bit wear during drilling operations under different loading conditions.

Future work is recommended to develop the proposed bit to formation interface law. The majority of the recommended future work is to use the drilling test rig to find the values and parameters for various bit sizes, bit types, formation properties, fluid properties and flow rates. This work will require a lot of work and time but would be valuable to research and industry in developing vibration control methods and devices.

It is also recommended to improve the data acquisition program so that it is capable of a faster sampling rate. The current sampling rate maxes out at approximately 2.5 Hz. This may be due to the large amount of data being collected, the LabVIEW program itself, the capability of the computer or a combination of multiple factors.

Another important adjustment that may vastly improve the lateral load rod performance is to apply some kind of temperature compensation strain gauge. Additional work can be done with the wiring or the data conditioning to improve the accuracy of the rods.

REFERENCES

[1] "Refined Petroleum Products - Consumption," *The World Factbook*, 2013. [Online]. Available: https://www.cia.gov/library/publications/the-world-factbook/fields/2246.html#193. [Accessed: 01-Jan-2015].

[2] F. E. Dupriest, W. C. Elks Jr., S. Ottesen, P. E. Pastusek, and J. R. Zook, "Borehole Quality Design and Practices to Maximize Drill Rate Performance," *Proc. SPE ATCE*, 2010.

[3] P. E. Pastusek, D. Ertas, L. Wang, and J. R. Bailey, "Drillstring Mechanics Model for Surveillance, Root Cause Analysis, and Mitigation of Torsional and Axial Vibrations," *Proc. 2013 SPE / IADC Drill. Conf. Exhib.*, 2013.

[4] J. R. Bailey, E. D. Company, C. C. Elsborg, and E. Exxonmobil, "Design Evolution of Drilling Tools to Mitigate Vibrations," 2013.

[5] Y. a. Khulief, F. a. Al-Sulaiman, and S. Bashmal, "Vibration analysis of drillstrings with self-excited stick-slip oscillations," *J. Sound Vib.*, vol. 299, no. 3, pp. 540–558, 2007.

[6] G. W. Halsey, A. Kyllingstad, T. V Aarrestad, and D. Lysne, "Drillstring Vibrations: Comparison Between Theory and Experiments on a Full-Scale Research Drilling Rig," *IADC/SPE Drill. Conf.*, no. SPE 15564, 1986.

[7] W. R. Tucker and C. Wang, "On the Effective Control of Torsional Vibrations in Drilling Systems," *J. Sound Vib.*, vol. 224, no. 1, pp. 101–122, 1999.

[8] W. R. Tucker and C. Wang, "An Integrated Model for Drill-String Dynamics," *J. Sound Vib.*, vol. 224, no. 1, pp. 123–165, 1999.

[9] T. Richard, C. Germay, and E. Detournay, "A simplified model to explore the root cause of stick-slip vibrations in drilling systems with drag bits," *J. Sound Vib.*, vol. 305, no. 3, pp. 432–456, 2007.

[10] T. Richard and E. Detournay, "Stick-slip vibrations of PDC bits," *Pacific rocks 2000; "rock around rim"; Proc. fourth North Am. Rock Mech. Symp. NARMS 2000, Seattle, Washington, USA*, pp. 33–40, 2000.

[11] P. Detournay, E. Defourny, “A Phenomenological Model for the Drilling Action of Drag Bits,” *int. J. Rock Mech. Min. Sci. Geomech.*, vol. 29, no. I, pp. 13–23, 1992.

[12] E. Detournay, T. Richard, and M. Shepherd, “Drilling response of drag bits: Theory and experiment,” *Int. J. Rock Mech. Min. Sci.*, vol. 45, no. 8, pp. 1347–1360, 2008.

[13] B. Besselink, N. van de Wouw, and H. Nijmeijer, “A Semi-Analytical Study of Stick-Slip Oscillations in Drilling Systems,” *J. Comput. Nonlinear Dyn.*, vol. 6, no. 2, p. 021006, 2011.

[14] D. Dareing, J. Tlusty, and C. Zamudio, “Self-Excited Vibrations Induced by Drag Bits,” *J. Energy Resour. Technol.*, vol. 112, no. 1, p. 54, 1990.

[15] C. a Zamudio, J. L. Tlusty, and D. W. Dareing, “Self-Excited Vibrations in Drillstrings,” *SPE Annu. Tech. Conf. Exhib.*, no. SPE 16661, pp. 1–8, 1987.

[16] L. F. P. Franca, “Drilling Action of Roller-Cone Bits: Modeling and Experimental Validation,” *J. Energy Resour. Technol.*, vol. 132, no. 4, p. 043101, 2010.

[17] H. Huang, B. Damjanac, and E. Detournay, “Normal Wedge Indentation in Rocks with Lateral Confinement,” vol. 31, pp. 81–94, 1998.

[18] H. Alehossein, E. Detournay, and H. Huang, “An Analytical Model for the Indentation of Rocks by Blunt Tools,” *Rock Mech. Rock Eng.*, vol. 33, no. 4, pp. 267–284, 2000.

[19] L. F. P. Franca, “A bit-rock interaction model for rotary-percussive drilling,” *Int. J. Rock Mech. Min. Sci.*, vol. 48, no. 5, pp. 827–835, 2011.

[20] D. Miller and a Ball, “Rock Drilling with Impregnated Diamond Microbits - an Experimental-Study,” *Int. J. Rock Mech. Min. Sci. Geomech. Abstr.*, vol. 27, no. 5, pp. 363–371, 1990.

[21] C.-M. Liao, B. Balachandran, M. Karkoub, and Y. L. Abdel-Magid, “Drill-String Dynamics: Reduced-Order Models and Experimental Studies,” *J. Vib. Acoust.*, vol. 133, no. 4, p. 041008, 2011.

[22] N. Mihajlović, a. a. van Veggel, N. van de Wouw, and H. Nijmeijer, “Analysis of Friction-Induced Limit Cycling in an Experimental Drill-String System,” *J. Dyn. Syst. Meas. Control*, vol. 126, no. 4, p. 709, 2004.

[23] L. Gerbaud, S. Menand, H. Sellami, and M. De Paris, “PDC Bits : All Comes From the Cutter / Rock Interaction,” 2006.

[24] Y. Amghar, H. Denoix, B. Cuiller, and H. Sinardet, “PDC Bit Steerability Modeling and Testing for Push-the-bit and Point-the-bit RSS,” pp. 1–12, 2012.

[25] J. K. Wilson, “Design and Analysis of a Test Rig for Modeling the Bit/Formation Interface in Petroleum Drilling Applications,” Texas A&M University, 2013.

[26] A. J. Wheeler and A. R. Ganji, *Introduction to Engineering Experimentation*, Third. Prentice Hall, 2010.

[27] C. C. Perry and H. R. Lissner, *The Strain Gauge Primer*, Second Edi. New York, NY: McGraw-Hill Book Company, 1962.

[28] IHS, “AC Motors Information,” 2015. [Online]. Available: http://www.globalspec.com/learnmore/motion_controls/motors/ac_motors.

[29] K. Ogata, *System Dynamics*, Fourth Edi. Upper Saddle River, NJ: Pearson Prentice Hall, 2004.

[30] B. Der-Petrossian, “Roofing, Technolofy Profile No.1 - Fibre-concrete,” *J. Netw. African Ctries. Local Build. Mater. Technol.*, vol. 3, no. Number 2, 1994.

[31] S. C. Chapra and R. P. Canale, *Numerical Methods for Engineers*, 6th Editio. New York, NY: McGraw-Hill Book Company, 2010.